UNIVERSITY OF CALIFORNIA, SAN DIEGO

Plasmonic Nanoarrays for Enhanced Photoemission, Rectification, and Photodetection

A dissertation submitted in partial satisfaction of the requirements for the degree

Doctor of Philosophy

in

Electrical Engineering (Electronic Circuits and Systems)

by

Shiva Piltan

Committee in charge:

Professor Daniel F. Sievenpiper, Chair
Professor Gert Cauwenberghs
Professor Eric Fullerton
Professor Boubacar Kante
Professor Brian Keating

2017

The Dissertation of Shiva Piltan is approved, and it is acceptable in quality and form for publication on microfilm and electronically:

_____

_____

_____

_____

_____

Chair

University of California, San Diego

2017

DEDICATION

To my beloved parents and sister.

TABLE OF CONTENTS

Signature Page iii

Dedication iv

Table of Contents v

List of Figures viii

Acknowledgments xii

Vita xiv

Abstract of the Dissertation xv

Chapter 1 Introduction 1

1.1. Vacuum and Semiconductors 1

1.2. Electron Emission Mechanisms 3

1.2.1. Thermionic Emission 5

1.2.2. Field Emission 6

1.2.3. Photo-assisted Field Emission and Photoemission . 8

1.2.4. Optical Field Emission 9

1.2.5. Transition Between Emission Mechanisms 10

1.3. Plasmon-induced Field Enhancement 11

Chapter 2 Field Enhancement in an Array of Gold Nanostructures 13

2.1. Design and Optimization 13

2.1.1. Design Background 13

2.1.2. Modeling and Simulations 14

2.2. Fabrication 19

2.3. Characterization and Measurement 21
2.4. Modeling and Discussion 24
2.4.1. Discussion of Measured Characteristics 24
2.4.2. Modeling the Device 25
2.4.3. Comparison Between Analytical Solution and Measurements 27
2.5. Summary 30
Chapter 3 Variations of the Resonant Surface and Their Properties 31
3.1. Geometrical Control over Field Enhancement 31
3.2. Design and Optimization 33
3.3. Fabrication 38
3.4. Characterization and Measurement 39
3.5. Scaling Property of Photocurrent with Surface Area 41
3.6. Analytical Field Enhancement Factor Extraction 43
3.7. Summary 47
Chapter 4 Optical Rectification Using Geometrical Field Enhancement in Gold Nano-arrays 48
4.1. Introduction 48
4.2. Rectenna Challenges 50
4.3. Design and Optimization 55
4.4. Fabrication 58
4.5. Characterization and Measurement 60

4.6. Modeling and Discussion 65
4.7. Summary 71
Chapter 5 Plasmonic Nano-arrays for Infrared Photodetection 73
5.1. Introduction 73
5.2. Design and Optimization 76
5.3. Fabrication 79
5.4. Characterization and Measurement 80
5.5. Modeling and Discussion 81
5.6. Summary 87
Chapter 6 Summary and Conclusion 88
Bibliography 91

LIST OF FIGURES

Figure 1.2.1. Thermionic emission in a metal with work function φ and Fermi level EF..... 5
Figure 1.2.2. Field emission. Work function is effectively reduced due to image charge effects..... 7
Figure 1.2.3. Photo-assisted field emission by absorption of (a) one or (b) two photons..... 8
Figure 1.2.4. (a) Photoemission and (b) above-threshold photoemission processes..... 9
Figure 1.2.5. Optical field emission..... 9

Figure 2.1.1. Surface Enhanced Raman Scattering through nano-cavities on a rough surface upon excitation with optical radiation..... 14
Figure 2.1.2. Plasmon-induced photoemission vacuum-channel device. Resonant array emits electrons under a CW laser illumination and a DC bias..... 15
Figure 2.1.3. Plasmon-induced photoemission vacuum-channel device. Resonant array emits electrons under a CW laser illumination and a DC bias..... 15
Figure 2.1.4. Schematic of the resonant vacuum-channel device. (a) DC biased array under laser illumination. (b) Top- view of multiple cells, W= 450 nm, L= 120 nm, T= 770 nm, S= 400 nm, H= 140 nm, and G= 100 nm..... 16
Figure 2.1.5. Real and imaginary parts of the complex refractive index of gold as a function of wavelength..... 17
Figure 2.1.6. Simulation unit-cell, 140 nm of e-beam evaporated gold on top of 200 nm isolating SiO2 on Si wafer..... 17
Figure 2.1.7. Electric field enhancement in the gap as a function of incident wavelength..... 18
Figure 2.1.7. Simulated field profile in half unit-cell at 785 nm..... 19
Figure 2.2.1. Scanning Electron Microscope images of samples after fabrication..... 20
Figure 2.3.1. Measured current as a function of DC voltage, for fixed laser power intensities (0, 60, 95, and 120 $\frac{W}{cm^2}$ shown)..... 21
Figure 2.3.2. $\log\left(\frac{I}{V^2}\right) - \frac{1}{V}$ Fowler-Nordheim curves for optical intensity of 60, 95, and 120 $\frac{W}{cm^2}$, inset for DC voltage above 8 volts..... 22
Figure 2.3.3. Current versus optical power density for fixed DC electric field (0.11 v/nm)..... 23
Figure 2.3.4. Current versus optical power density for fixed DC electric field (0.11 v/nm) in log scale and their linear regression, the slope is an indication of the number of photons absorbed..... 23
Figure 2.4.1. Comparison between analytical model and measurement results.

I-V curves at radiation intensity= 115 $\frac{W}{cm^2}$, analytical solution (solid, red), measured data (blue)..... 28
Figure 2.4.2. Comparison between analytical model and measurement results. I-P curves at DC field= 0.11 V/nm, analytical solution (solid, red), measured data (blue)..... 28
Figure 2.4.3. Total time averaged current as a function of DC field and Enhanced laser power density based on analytical solution..... 29

Figure 3.1.1. Modified flat structure for enhanced field intensity..... 32
Figure 3.2.1. Simulation unit-cell. Symmetry of the design and periodicity of the boundary conditions allow simulation of only quarter of unit-cell... 33
Figure 3.2.2. Multiple unit-cells of the triangular array and the simulated geometric parameters..... 34
Figure 3.2.3. Simulated field enhancement as a function of frequency for final optimized dimensions, solid (blue) at the edge of the triangular tip on the substrate, dashed (red) at the edge of the triangular tip 65 nm above substrate..... 35
Figure 3.2.4. Simulated field enhancement profile on the side interface of triangular half unit- cell upon incident of plane wave at 785 nm polarized along the tip axis..... 36
Figure 3.2.5. Simulated field enhancement profile on the top interface of triangular half unit- cell upon incident of plane wave at 785 nm polarized along the tip axis..... 36
Figure 3.2.6. Simulated field enhancement in the vacuum gap as a function of distance from gap edge for three different vertical distances from substrate, 130 nm (top), 65 nm (middle), and on substrate, upon incident of plane wave at 785 nm polarized along the tip axis..... 37
Figure 3.3.1. Scanning electron microscope images of periodic surface after fabrication..... 39
Figure 3.4.1. Measured current-voltage characteristics for the triangular sharp tip array for fixed radiation intensities centered at 785 nm (0, 65, 102, 141, 176, and 200 $\frac{W}{cm^2}$ shown)..... 40
Figure 3.4.2. Measured current-optical power characteristics for the triangular sharp tip array for fixed DC bias voltages (3, 6, 8, and 11 volts shown)..... 41
Figure 3.5.1. Scanning electron microscope images of the 80x80 element array.. 42
Figure 3.5.2. Measured current-optical power characteristics for fixed DC bias voltages (5.5, 6, and 6.5 volts shown) for 40x40 and 80x80 element surface..... 42
Figure 3.6.1. Measured $\log\left(\frac{I}{V^2}\right) - \frac{1}{V}$ characteristics for the triangular sharp tip array for fixed radiation intensities centered at 785 nm (0, 65, 102, 141, 176, and 200 $\frac{W}{cm^2}$ shown)..... 43

Figure 3.6.2. Measured $\log\left(\frac{I}{V^2}\right) - \frac{1}{V}$ characteristics for the triangular sharp tip array for fixed radiation intensities centered at 785 nm (0, 65, 102, 141, 176, and 200 $\frac{W}{cm^2}$ shown)..... 44
Figure 3.6.3. Measured $\log\left(\frac{I}{V^2}\right) - \frac{1}{V}$ characteristics for the triangular sharp tip array for fixed radiation intensities centered at 785 nm (0, 65, 102, 141, 176, and 200 $\frac{W}{cm^2}$ shown), and their linear regression..... 45
Figure 3.6.4. Field enhancement factor as a function of optical power density extracted using the slope of measured Fowler-Nordheim type cuves for 50 nm gap size and 5.1 eV gold work function..... 46

Figure 4.1.1. Block diagram of rectenna device attached to a load..... 49
Figure 4.3.1. Schematic of designed resonant optical rectifier. Rectifying unit-cell of geometrically asymmetrical electrodes with 50 nm air gap in between, optimized for maximum field enhancement at the sharp tip..... 56
Figure 4.3.2. Schematic of designed resonant optical rectifier. Resonant array consisting of 3 terminals, the flat electrode terminal and two sharp tip terminals. One of the sharp tip terminals is grounded in our measurements..... 57
Figure 4.3.3. Simulation results. Electric field enhancement 25 nm above the substrate on the sharp electrode (green) and flat electrode (cyan), and 50 nm above the substrate on the sharp electrode (blue) and flat electrode (red), as a function of frequency..... 58
Figure 4.3.4. Simulation results at 382 THz. Side view of asymmetrical field profile in the air gap between the electrodes showing different field ratios on each side..... 58
Figure 4.4.1. Scanning electron microscope images of fabricated samples..... 59
Figure 4.5.1. Measurement setup for rectifying structure. Two source- meters simultaneously measure the currents through the flat terminal and the sharp terminal..... 61
Figure 4.5.2. Measured I-V characteristics for various laser power densities, current on sharp terminal as a function of voltage over it..... 62
Figure 4.5.3. Measured I-P characteristics at various DC bias voltages on sharp terminal..... 62
Figure 4.5.4. Measured I-V characteristics for various laser power densities, current on flat terminal as a function of voltage over sharp terminal..... 63
Figure 4.5.5. Measured I-V characteristics for various laser power densities, current on flat terminal as a function of voltage over it..... 64
Figure 4.5.6. Measured I-V characteristics for various laser power densities, current on sharp terminal as a function of voltage over flat terminal..... 65

Figure 4.6.1. Diode figures of merit calculated from measured I-V characteristic using a model based on Taylor expansion of current in oscillating potential, Responsivity based on classical definition limited to 1.2663 at λ= 785 nm..... 67
Figure 4.6.2. Diode figures of merit calculated from measured I-V characteristic using a model based on Taylor expansion of current in oscillating potential, resistance for various optical powers..... 68
Figure 4.6.3. Diode figures of merit calculated from measured I-V characteristic using a model based on Taylor expansion of current in oscillating potential, asymmetry defined as the ratio of forward to reverse current as a function of applied voltage based on measured values. 69
Figure 4.6.4. Diode figures of merit calculated from measured I-V characteristic using a model based on Taylor expansion of current in oscillating potential, nonlinearity, a measure of deviation from a linear resistor as a function of voltage..... 69
Figure 4.6.5. Power conversion efficiency in 382 THz based on measurement results..... 71

Figure 5.2.1. Resonant surface for maximized field enhancement at 25 THz..... 76
Figure 5.2.2. Simulated optimized dimensions for maximized field enhancement at 25 THz..... 77
Figure 5.2.3. Simulated field enhancement as a function of frequency for final optimized dimensions, solid (red) at the edge of the triangular tip, dashed (blue) in the middle of the gap, both vertically 37.5 nm above substrate..... 78
Figure 5.2.4. Side view of field profile in the air gap between the electrodes at 23 THz..... 78
Figure 5.3.1. Scanning electron microscope images of fabricated resonant array. 79
Figure 5.4.1. Measured current-voltage characteristic of array for infrared detection..... 80
Figure 5.5.1. Spectral radiance as a function of wavelength for a variety of temperatures..... 81
Figure 5.5.2. Responsivity as a function of applied voltage based on current-voltage characteristic curves..... 85
Figure 5.5.3. Specific detectivity as a function of applied voltage based on current-voltage characteristic curves..... 85
Figure 5.5.4. Efficiency as a function of applied voltage based on current-voltage characteristic curves..... 86

ACKNOWLEDGMENTS

First and foremost, I would like to express my sincere appreciation for my advisor, Prof. Daniel Sievenpiper, for his continuous guidance, patience, and encouragement throughout the entirety of my graduate program. He was the perfect role model for approaching research problems with his great vision and will always be an example I will refer to in true support and mentorship. I am privileged to experience working in his group and learning from his insight and ability to stay future-oriented in a broad range of topics while keeping the depth of research and knowledge. I will always be candidly grateful for all his advices and support.

I would like to thank my committee members, Prof. Gert Cauwenberghs, Prof. Eric Fullerton, Prof. Boubacar Kante, and Prof. Brian Keating, for taking the time to be part of my committee and for their valuable comments and suggestions.

The experience of PhD was made a lot more delightful because of the fantastic people I was lucky enough to work with in Applied Electromagnetics group. I am very thankful for all the consultations and instructions and for the cheerful times and laughs we had together. I would also like to thank all my friends from UCSD and outside UCSD who supported me throughout my time as a graduate student by teaching me resistance in tough times and helping me keep a balanced life. I would like to specially thank Dmitry, who was there for me through the most challenging times, who inspired me to try to be a little better every day, and whose belief in me encouraged me to move forward and to smile no matter what.

Words fall short to express my sincere gratitude to my family. To my sister, Mina, who never failed to show me how deeply she cares about me and how genuinely she is willing to be there for me as soon as I need comfort in any situation. To my father, for having so much faith in me even when I do not, for inspiring me to dream big and to work hard to follow them, and for showing me constant support even when physically far apart. To my mother, for countless sacrifices she made for me to come this far, for her exemplar courage, for being my best friend and teacher, and for showing me nothing but unlimited selfless love regardless of what I do.

The material in this dissertation is based on the following papers which are either published, under review or in preparation for submission.

Chapter 1 and 2, in part, have been submitted for publication of the material as it may appear in: S. Piltan, D. Sievenpiper, "Field Enhancement in Plasmonic Nanostructures". The dissertation author was the primary author of this material.

Chapter 3 and 5, in part, are currently being prepared for submission for publication of the material as it may appear in: S. Piltan, D. Sievenpiper, "Plasmonic Nano-arrays for Enhanced Photoemission and Photodetection". The dissertation author was the primary author of this material.

Chapter 4, in part, has been submitted for publication of the material as it may appear in: S. Piltan, D. Sievenpiper, "Optical Rectification Using Geometrical Field Enhancement in Gold Nano-arrays". The dissertation author was the primary author of this material.

VITA

2012	Bachelor of Science in Electrical Engineering, Sharif University of Technology, Tehran, Iran
2013-2017	Research Assistant, University of California, San Diego
2017	Doctor of Philosophy in Electrical Engineering (Electronic Circuits and Systems), University of California, San Diego

PUBLICATIONS

S. Piltan, D. Sievenpiper, "Field Enhancement in Plasmonic Nanostructures", submitted to Physical Review A.

S. Piltan, D. Sievenpiper, "Optical Rectification Using Geometrical Field Enhancement in Gold Nano-arrays", submitted to Journal of Applied Physics.

S. Piltan, D. Sievenpiper, "Plasmonic Nano-arrays for Enhanced Photoemission and Photodetection", in preparation.

E. Forati, **S. Piltan**, A. Li, D. Sievenpiper, "Experimental study of the interaction between DC discharge microplasmas and CW lasers", *Optics Express*, vol. 24, no. 2, p. 1495-1506, 2016.

E. Forati, **S. Piltan**, D. Sievenpiper, "On the difference between breakdown and quench voltages of argon plasma and its relation to 4 p–4 s atomic state transitions", *Applied Physics Letters*, vol. 106, no. 5, p. 054101, 2015.

E. Forati, **S. Piltan**, D. Sievenpiper, "Stadium mushroom metasurface for electro-optical ignition of gas plasma", *CLEO: Science and Innovations*, p. JTu5A-99, 2015.

E. Forati, **S. Piltan**, D. Sievenpiper, "Microplasma generation: Using metasurfaces to combine DC discharge and laser induced breakdown", *Radio Science Meeting (Joint with AP-S Symposium), 2015 USNC-URSI*, p. 138, 2015.

ABSTRACT OF THE DISSERTATION

Plasmonic Nanoarrays for Enhanced Photoemission, Rectification, and Photodetection

by

Shiva Piltan

Doctor of Philosophy in Electrical Engineering (Electronic Circuits and Systems)

University of California San Diego, 2017

Professor Daniel F. Sievenpiper, Chair

Conversion of photons to electrical energy has a wide variety of applications including imaging, solar energy harvesting, and infrared detection. The coupling of electromagnetic radiation to free electron oscillations at a metal interface results in interesting properties including enhanced electric fields tightly confined to the surface. Taking advantage of this nonlinear light-matter interaction, this work presents a variety of resonant surfaces optimized for combining electrical and photonic

excitations in order to liberate electrons in a vacuum-channel device for applications ranging from enhanced photoemission, optical rectification, and infrared photodetection.

Chapter 1

Introduction

The coupling of electromagnetic radiation to free electron oscillations at a metal interface and its consequent properties including enhanced optical near-field have drawn significant interest to the field of plasmonics and its applications. Some of the most widespread demonstrated applications of this nano-scale light-matter interaction include surface-enhanced Raman spectroscopy (SERS) [1,2], plasmonic color pixels for CMOS compatible imaging and bio-sensing [3,4,5], hot electron photo-electrochemical and photovoltaic devices and photodetectors [6,7,8,9], optical antennas [10,11], plasmonic integrated circuits [12,13], and metamaterials [14,15]. By taking advantage of the plasmonic surface field enhancement in simple periodic structures, we have significantly moderated conditions required for electron liberation in vacuum channel devices using a combination of DC and optical excitations. We exploited this idea in a variety of applications requiring efficient generation of charge carriers including optical rectification and IR photodetection by modifying the geometry of the scalable periodic surface.

1.1. Vacuum and Semiconductors

The discovery of the first solid-state diode goes back to 1874 by Ferdinand Braun where he demonstrated the unidirectional flow of charge at the contact point

between a metal and galena crystal [16]. The phenomenon behind thermionic emission was later discovered independently by Frederick Guthrie and Thomas Edison [17] and the first practical vacuum tube device, the thermionic diode, was patented by John Ambrose Fleming in 1904 [18]. The idea of solid-state rectifiers made a comeback due to a number of reasons [19]. First, vacuum tubes did not satisfy the desired frequency requirements. Furthermore, the theory of quantum mechanics was significantly advanced in 1920s, leading to an insightful understanding of solids, band structures, and Schottky barriers. Also, solid-state devices provided superior lifetime, higher efficiency, lower cost, smaller size, and were easily integrated.

Vacuum tubes and MOSFETs resemble each other in some respects and differ in other. They are both essentially 3 terminal devices. The current flow from cathode to anode is controlled by the voltage on the grid in the former and gate voltage modulates the drain to source current in the latter. The current in semiconductor transistors comes from the drift and diffusion of electrons whereas in vacuum tubes it is due to thermionic emission. The most important difference between vacuum and solid-state devices is the charge transport in the medium. Carriers are transported in a ballistic flow in vacuum rather than collisional in semiconductors. This theoretically enables electron speeds up to 3 orders of magnitude higher in vacuum than e.g. GaAs and provides a solution to address the Terahertz gap [20]. Vacuum devices are also intrinsically less susceptible to over-radiation and heating damage.

Today, semiconductor fabrication techniques have advanced considerably and they can now be used to produce vacuum devices with reduced gap size of a fraction

of mean free path length of electrons. The smaller gap moderates the need for high vacuum since there is smaller chance of collision with gas molecules. This also relieves cathode degradation caused by bombardment of positive ions. In addition, reduced gap size corresponds to shorter carrier travel distances and consequently higher switching speeds. The short distance between anode and cathode electrodes also provides higher electric fields for the same applied voltage and enhances efficiency of the device. However, liberating electrons from the metal surface efficiently remains a challenging task.

1.2. Electron Emission Mechanisms

In order to liberate the cold, bound electrons from a metal surface into vacuum it is required to overcome the work function of the metal. Work function is a surface property of the material and it is defined as the minimum energy needed to remove an electron from the solid to a state at rest in the nearby vacuum. Applying thermal or electrical energy can enable electron emission by modifying the electron distribution inside the metal and the probability of transmission for electrons with the same initial energy level.

The procedure to calculate the emitted current density from metals is similar regardless of the emission mechanism. Current density is given as a function of applied electric field, temperature of electron gas in the bulk material, and Fermi level. Fermi function is the probability that a given electron energy state is occupied at a certain temperature. In other words, the energy distribution of occupied states in metal is given by the Fermi-Dirac function:

$$f_{FD}(E) = \frac{1}{1+e^{(E-E_F)/K_B T}}$$ **Equation 1.2.1**

Where K_B is the Boltzmann constant, T is the temperature, and E_F is the Fermi energy. The Fermi energy is the level of the lowest available electron state at absolute zero temperature and no electron will have sufficient energy to go above this level. It can be considered as a hypothetical energy level of an electron, such that at thermodynamic equilibrium this energy level would have a 50% probability of being occupied at any given time.

The first step for calculating the electron flow is to evaluate the supply function. The supply function is defined as the number of electrons per second per unit area with total energy within w and w+dw whose normal energy on barrier lies within ε and ε+dε. Next, the transmission probability or the probability of an electron with normal energy ε to escape the barrier needs to be found. Total emitted current density is obtained by integrating the product of the supply function, N, and the transmission probability, D, over all energy states and it is given by:

$$J(E, E_F, T) = q \iint D(E, \varepsilon) N(T, E_F, \varepsilon, w) d\varepsilon dw$$ **Equation 1.2.2**

Here, E, E_F, T, q, w, and ε are the electric field at the surface, Fermi level, temperature, charge of electron, total energy of incident electron, and the energy of charge carrier in the normal direction to the metal-vacuum interface, respectively. Depending on the dominant emission mechanism, increase in the supply function, transmission probability, or both contribute to the current density.

1.2.1. Thermionic Emission

If kinetic energy of charge carriers is increased by heating such that it becomes sufficient to overcome the work function of the barrier, the dominant emission mechanism is called thermionic emission. The form of the Fermi-Dirac distribution function imposes that at ordinary temperatures, most of the filled states lie below the Fermi level and relatively fewer electrons have energies above it. Increasing the temperature extends the high-energy tail of the energy distribution as shown in Figure 1.2.1 and the part of it falling beyond $E_F + \phi$ promotes electron liberation, where ϕ is the work function of metals.

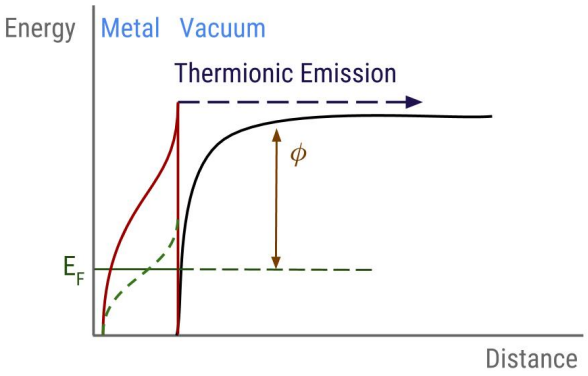

Figure 1.2.1. Thermionic emission in a metal with work function ϕ and Fermi level E_F.

Assuming the potential barrier is not deformed the transmission probability of electrons has the form:

$$D(E,\varepsilon) = 0 \quad \text{for} \quad \frac{mv_x^2}{2} < q\phi$$

$$D(E,\varepsilon) = 1 \quad \text{for} \quad \frac{mv_x^2}{2} > q\phi$$

Equation 1.2.3

Here, v_x is the velocity of electrons in direction normal to the barrier interface. The supply function in this case can be obtained using the Fermi-Dirac distribution

function. For energy levels in the high-energy tail of the Fermi-Dirac density of states, the distribution is identical to the classical Maxwell-Boltzman distribution allowing its replacement. Substituting these values in equation 1.2.2 and integrating over all energy states gives the Richardson-Dushman equation for current density in thermionic emission [21]:

$$J_{thermionic} = AT^2 e^{-\phi/K_B T}$$

$$A = \frac{4\pi q m K_B^2}{h^3} = 1.2\times10^6\ [Am^{-2}K^{-2}]$$

Equation 1.2.4

Where m is the electron rest mass and h is Planck's constant.

1.2.2. Field Emission

The barrier at electric field strengths above 1 $\frac{V}{nm}$ becomes thin enough for the electrons to tunnel through from states close to Fermi level. This process, shown in Figure 1.2.2, is referred to as field emission and was analytically characterized by Fowler and Nordheim [22] by solving the 1D time-independent Schrödinger equation for a rounded triangular barrier. The barrier is rounded due to the image charge effect and has a lower effective work function. The electric potential energy as a function of distance from metal-vacuum interface is given by:

$$q\Phi(x) = q(E_F + \phi) - \frac{q^2}{16\pi\varepsilon_0 x} - qE_0 x$$ **Equation 1.2.5**

Where ϕ is the work function, E_0 is applied electric field, ε_0 is vacuum permittivity, and x is distance from surface. The potential at the surface is then a sum of the work function reduced by the image charge potential and the applied field.

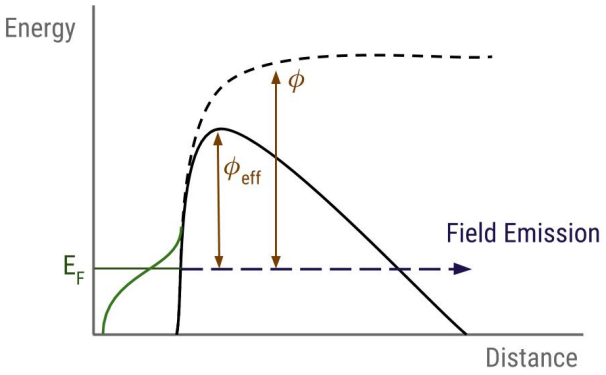

Figure 1.2.2. Field emission. Work function is effectively reduced due to image charge effects.

Fowler and Nordheim showed that the current density based on supply function given by the Sommerfeld electron distribution has a form of:

$$J_{FN} = \frac{A}{\phi} F^2 e^{-B\phi^{3/2}/F}$$

$$A = \frac{q^3}{8\pi h} = 1.543\times10^{-6}\ [A\ eV\ V^{-2}]$$

$$B = \frac{8\pi\sqrt{2m}}{3hq} = 6.83\ [eV^{-3/2}\ V\ nm^{-1}]$$

Equation 1.2.6

A and B are referred to as the first and second Fowler-Nordheim constants, respectively, F is the total field at the surface, and work function ϕ is in eV. It can therefore be concluded that for the strong-field tunneling mechanism, $\ln(\frac{I}{F^2})$ versus $\frac{1}{F}$ curves should be linear with a negative slope depending on the work function and the surface field enhancement. These curves are referred to as the Fowler-Nordheim type curves. The slope of the curve is equal to $\frac{B\phi^{3/2}}{\beta}$ where β is field enhancement factor at

the surface. Knowing the slope of Fowler-Nordheim curves, it is possible to extract the work function and field enhancement.

1.2.3. Photo-assisted Field Emission and Photoemission

The addition of optical excitation can interact with the system by both modulating the barrier and increasing the initial energy of electrons due to photon absorption [23,24,25]. The dominant mechanism for weak optical fields is either photo-assisted field emission [Figure 1.2.3] or photoemission [Figure 1.2.4]. In the photo-assisted field emission process, electron energy is enhanced to a non-equilibrium distribution by absorption of one/two photons of frequency w and tunnels through thereafter.

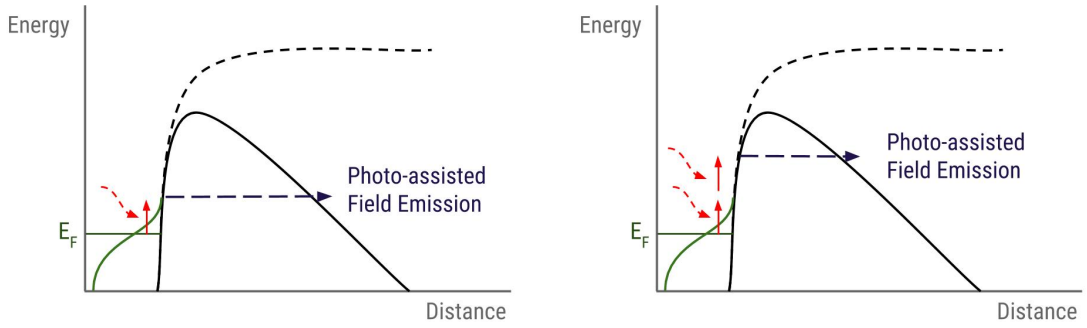

(a) (b)

Figure 1.2.3. Photo-assisted field emission by absorption of (a) one or (b) two photons.

In the photoemission process, the electron absorbs a sufficient number of photons to travel above the barrier as shown in Figure 1.2.4. If the multiphoton emission process happens by absorption of a greater number of photons than required ($n > \phi/\hbar w$) the process is called above-threshold photoemission [26]. It has been shown than in the multiphoton regime photo-emitted current is proportional to the nth

power of laser intensity, where n is the total number of photons absorbed, that is $I \propto |F|^{2n}$, where F is the incident peak field. [26,27].

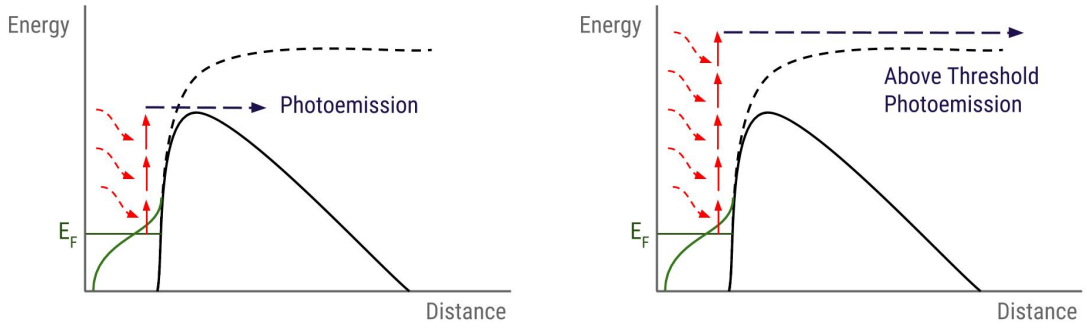

(a) (b)

Figure 1.2.4. (a) Photoemission and (b) above-threshold photoemission processes.

1.2.4. Optical Field Emission

If the laser intensity is sufficiently large, the potential barrier becomes narrow enough during part of the optical cycle for the electrons to tunnel through directly from the Fermi level.

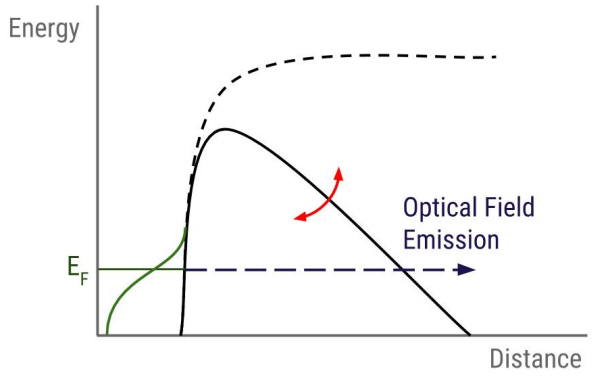

Figure 1.2.5. Optical field emission.

This process is called optical field emission and it is shown in Figure 1.2.5. The average kinetic energy of the electron in the optical field exceeds the ionization energy of metal in optical field emission process. Fowler-Nordheim type equations

can be used in this strong-field regime by substituting the total field with the sum of DC and AC fields.

1.2.5. Transition Between Emission Mechanisms

The transition between the photon-driven and field-driven regimes is characterized by Keldysh parameter which is defined as the ratio of the incident optical frequency to the characteristic tunneling frequency of metal [28]. The Keldysh parameter can be written as:

$$\gamma = \sqrt{\frac{I_P}{2U_p}} = \frac{w}{w_t} \qquad \textbf{Equation 1.2.7}$$

Where I_P is the ionization energy of the metal, $U_p = \frac{q^2E^2}{4mw^2}$ is the average ponderomotive energy in the oscillating laser field E with frequency w, and $w_t = \frac{qE}{\sqrt{2m\phi}}$ is the characteristic tunneling frequency [29]. For relatively weak fields where $\gamma > 1$, the maximum oscillation amplitude of electrons in the applied field, referred to as the quiver amplitude, is smaller than the decay length of the near field; therefore, electrons are back accelerated before they are liberated and the dominant process is multiphoton induced emission [23,30]. For stronger fields where $\gamma < 1$ the average kinetic energy of electrons in the oscillating fields is larger than the ionization energy of metal. The local slope of the photocurrent as a function of laser intensity drops as the dominant mechanism changes from multi-photon induced emission to optical field emission and therefore it is an appropriate characterizing property [26,30].

1.3. Plasmon-induced Field Enhancement

We can consider the DC and laser induced electron emission essentially as a two-step process. First, electrons are photoemitted due to either of the mechanisms. Next they are accelerated by combination of the external and plasmon-induced fields. Any charged particle, regardless of polarity, is subject to a nonlinear net force called the ponderomotive force towards the weak field region when located in a non-homogeneous field. The larger the field gradient, the stronger the ponderomotive force and therefore acceleration. Ponderomotive force can be written as:

$$F_P = -\frac{q^2}{4mw^2}\nabla(E^2)\ [N] \qquad \textbf{Equation 1.3.1}$$

The acceleration is due to the fact that the charged particle travels a longer distance in the strong field region than it does when it is back-accelerated in the weak-field region. Nanostructures supporting surface plasmon resonances provide both electric field enhancement and spatial sub-wavelength confinement. The induced local field enhancement can be used to facilitate the electron emission by providing access to high-field intensity regions and introducing a large field gradient causing enhanced ponderomotive acceleration. It also enables operation in intensities below the damage threshold of the metal [26,27,30,31,32,33,34,35].

Due to the finite effective mass of electrons, the phase lag between oscillating electrons and the incident electromagnetic field increases with frequency. The coulomb interaction with metal ions acts as the restoring force. The amplitude of the charge oscillation is maximized when the phase lag is increased to 90 degrees [36].

The degree of field enhancement correlates directly to the plasmon oscillation amplitude. Therefore, this frequency corresponds to the localized surface plasmon resonance frequency in metals and results in enhanced electric field near the surface. The resonant field enhancement is due to the collective oscillation of conduction band electrons in a confined region and it depends on the geometrical shape; therefore, it provides an additional control parameter to liberate electrons [33,37,38].

We have taken advantage of the plasmonic field enhancement in resonant metallic arrays of unit-cells in order to address the electron emission challenge in a variety of vacuum microelectronic devices for applications including enhanced photoemission, optical rectification, and photodetection. The geometrical dependence of the resonant frequency and its consequent localized field enhancement offers an important degree of freedom for optimizing the device for a spectrum of frequencies and a variety of applications. In addition, it enables the unit-cells to emit electrons at DC and optical power levels significantly below expected.

Chapter 1, in part, has been submitted for publication of the material as it may appear in: S. Piltan, D. Sievenpiper, “Field Enhancement in Plasmonic Nanostructures”. The dissertation author was the primary author of this material.

Chapter 2

Field Enhancement in an Array of Gold Nanostructures

As discussed in Chapter 1, in order to generate electron emission from metals, it is needed to either provide sufficient energy to electrons to promote to high energy level states and overcome the potential barrier, or to modify the barrier using DC or AC external fields. The input power levels required to create desired combination of carrier state and barrier shape can be significantly moderated using the nonlinear light-matter interaction between metals and an incoming optical radiation in plasmonic frequencies. This field-controlled interaction can demonstrate applicability in fields such as attosecond science, nano-scale antennas, medical imaging, chemical sensors, and photovoltaics. Here, we discuss design, fabrication, and characterization of a geometrically tailored gold nano-array demonstrating enhanced photoemission in exceptionally low DC and AC powers.

2.1. Design and Optimization

2.1.1. Design Background

The idea behind the design was initially inspired by Surface Enhanced Raman Scattering (SERS). This phenomenon is used for high-sensitivity detection of bio-molecular interactions such as single-molecule absorption on a rough metallic surface

and it is shown in Figure 2.1.1. Excitation of the substrate at the particular plasmon resonance frequency increases the intensity of the Raman signal detected for adsorbates on various substrates and the surface field enhancement pronounces this effect significantly. It is common to use visible and near-infrared radiation to excite Raman signals. The plasmon resonance frequencies of some metals such as gold and silver lie within these spectral ranges; therefore, they are typically used for intensifying the Raman modes. The mechanism behind this effect works based on the high quality factor optical cavities on the rough surface. We exploited an identical idea optimizing certain periodic structures for high quality factor resonance and enhanced photon absorption.

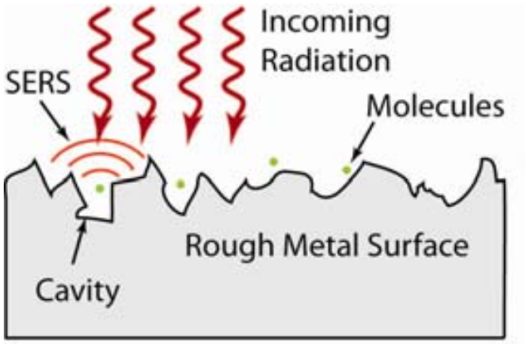

Figure 2.1.1. Surface Enhanced Raman Scattering through nano-cavities on a rough surface upon excitation with optical radiation.

2.1.2. Modeling and Simulations

Figure 2.1.2 shows the schematic of the periodic surface supporting local surface plasmon resonances in near-infrared range. It consists of multiple rows of unit-cells. There are two terminals serving as the feed for the DC excitation and every other

row of the array is connected to one terminal. Therefore, a vacuum channel is formed between the plates of each unit-cell on two adjacent rows.

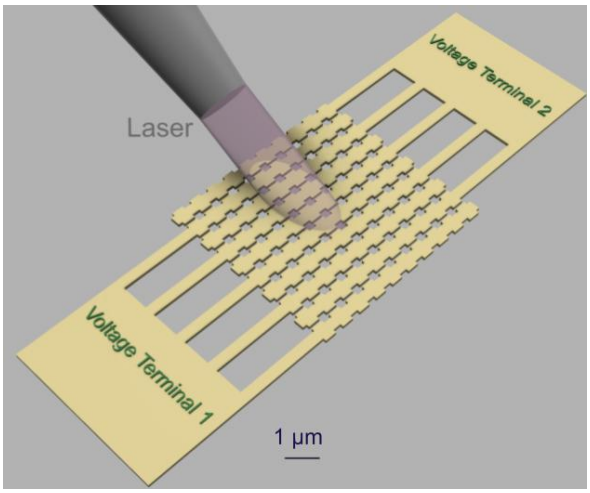

Figure 2.1.2. Plasmon-induced photoemission vacuum-channel device. Resonant array emits electrons under a CW laser illumination and a DC bias.

The geometry is tailored such that high electric field spots are achieved in the 100 nm gap between the resonant unit-cells as shown in Figure 2.1.3; consequently, the electron emission mainly occurs there. There are two parameters used to manipulate the electric field intensity in the channel, the static bias voltage providing the electrical control and the laser radiation providing the optical control.

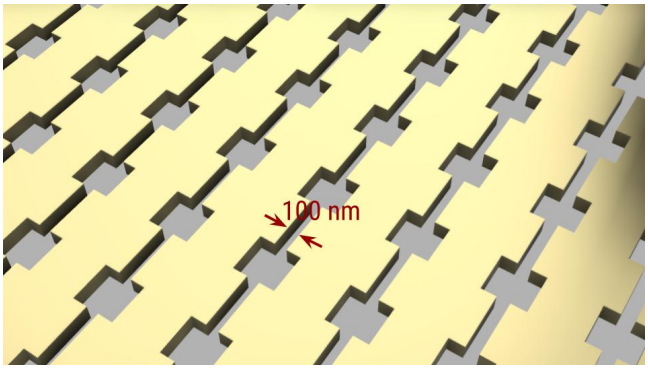

Figure 2.1.3. Plasmon-induced photoemission vacuum-channel device. Resonant array emits electrons under a CW laser illumination and a DC bias.

The dimensions of the geometry, including the gap between the plates G, the period of unit-cells T, the width and length of the fingers W and L, and the thickness of gold layer H have been optimized to provide the maximum electric field enhancement at the center point between the plates of unit-cells on two adjacent rows upon excitation with a plane wave at 785 nm, polarized in the direction normal to the plates (y direction as shown in Figure 2.1.4). Schematic of the DC biased array under laser illumination and the top view of multiple cells are shown in Figure 2.1.3 (a) and (b), respectively.

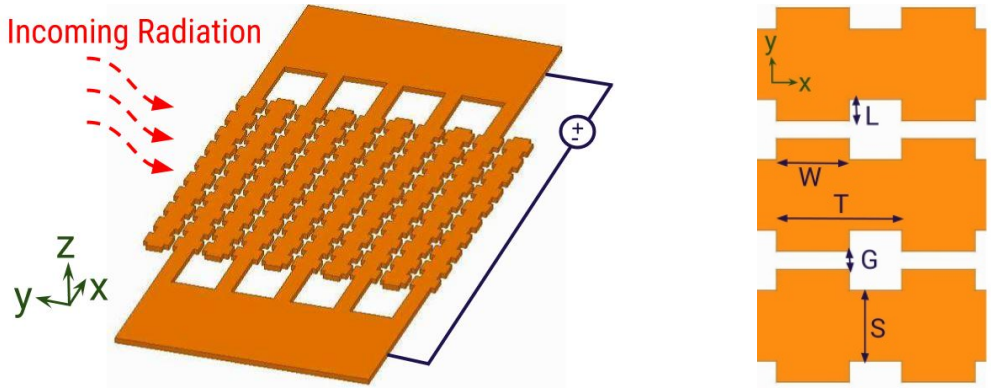

(a) (b)

Figure 2.1.4. Schematic of the resonant vacuum-channel device. (a) DC biased array under laser illumination. (b) Top- view of multiple cells, W= 450 nm, L= 120 nm, T= 770 nm, S= 400 nm, H= 140 nm, and G= 100 nm.

The design simulations were done using HFSS electromagnetics tool based on the finite-element method. We used the values from Johnson-Christy model for the complex dielectric constant properties of gold [39]. The real and imaginary parts of the wavelength-dependent complex refractive index of gold based on this model are shown in Figure 2.1.5.

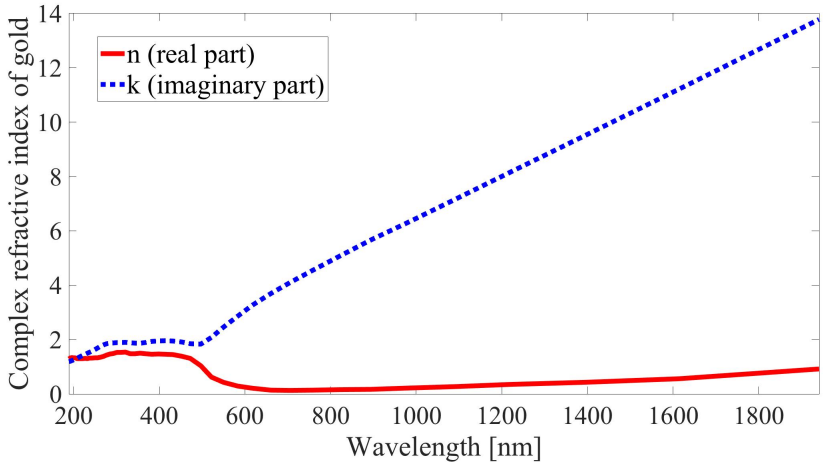

Figure 2.1.5. Real and imaginary parts of the complex refractive index of gold as a function of wavelength.

Simulations were done on a single unit-cell as shown in Figure 2.1.6. The gold unit-cell was designed on a 200 nm layer of silicon dioxide on silicon substrate. The isolation SiO_2 layer prevents leakage current through the substrate. The vertical boundaries of the simulation volume are either perfect electric or perfect magnetic conductors. This combination of boundary conditions presents a "hall of mirrors" effect and allows for simulations in an effectively infinite lattice of identical unit-cells. Radiation boundary condition was used for horizontal boundaries.

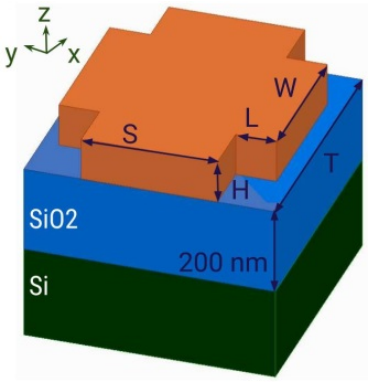

Figure 2.1.6. Simulation unit-cell, 140 nm of e-beam evaporated gold on top of 200 nm isolating SiO2 on Si wafer.

Field enhancement was defined as the ratio of the electric field in the middle point in the gap between adjacent unit-cells to the incident field. The incident field was a plane wave at 785 nm with magnitude of 1 v/m and polarization along the gap axis (y direction). The vacuum gap width between adjacent cells G, is inversely related to the intensity of field enhancement. Also, shorter gaps provide faster switching speeds by decreasing electron transit time. Therefore, we kept the gap parameter G= 100 nm which is a value enabling both easy fabrication and sufficiently high field enhancement. The final values of geometrical parameters optimized for maximum gap field enhancement are T= 770 nm, W= 450 nm, L= 120 nm, H= 140 nm, and S= 400 nm.

Figure 2.1.7 demonstrates the simulated field enhancement as a function of wavelength. It is shown that the electric field in the gap is enhanced approximately by a factor of 10 at the resonant mode in 785nm.

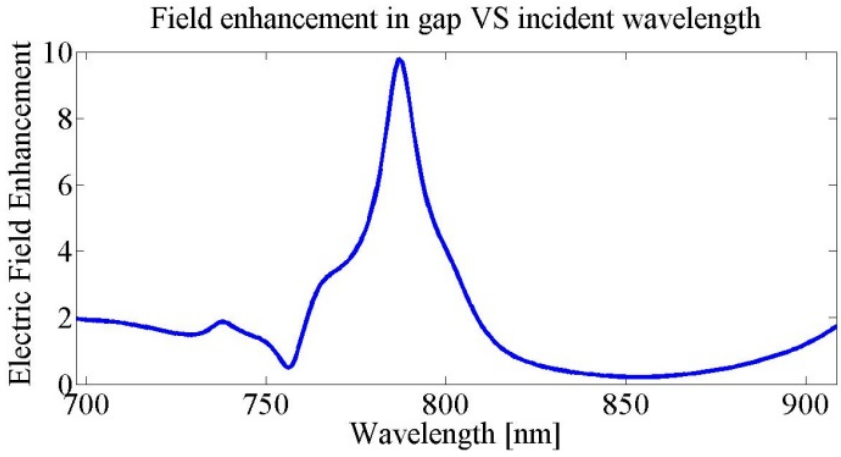

Figure 2.1.7. Electric field enhancement in the gap as a function of incident wavelength.

Field profile in the gap shows maximum enhancement at the top and bottom edges of the gold unit-cell. This means the majority of electrons are emitted from the

area around the edges. Figure 2.1.8 shows simulated field profile in half unit-cell at 785 nm, with maximum field confined in the air gap.

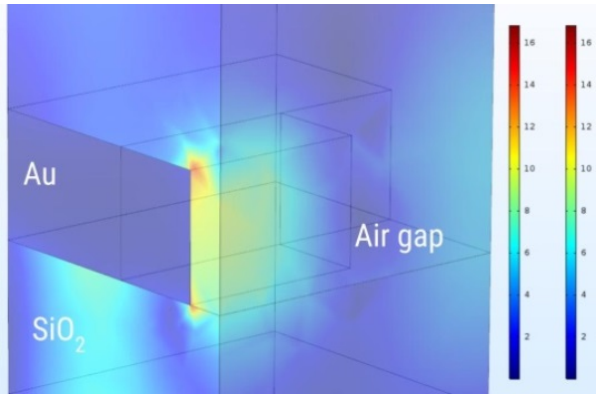

Figure 2.1.7. Simulated field profile in half unit-cell at 785 nm.

2.2. Fabrication

The designed 40x30 element array was fabricated on silicon wafers with a 200 nm thermally oxide SiO_2 layer for isolation. The 200nm SiO_2 layer provides sufficient isolation so that silicon absorption would not have a significant effect as it is theoretically and experimentally demonstrated [40]. After cleaning the wafer, 300 nm of polymethyl methacrylate (MicroChem 950PMMA A4) was spin coated for 45 seconds with 2000 rpm. The wafer was then baked on a 180 °C hot plate for 60 seconds. The 40x30 element layout was later exposed using electron beam lithography technique and Vistec EBPG5200 50/100 KV high performance nanolithography system. Next, the exposed samples were developed and etched using O_2 plasma for 5 seconds to insure clean layout. A 10nm chromium adhesion layer and 130nm of gold were electron beam evaporated subsequently using Temescal's BJD 1800 e-beam evaporator. Finally, lift-off was done using Remover PG over-night

and subsequently using acetone in an ultrasonic bath. The fabricated samples were later diced and imaged using FEI XL30-SFEG high-resolution scanning electron microscope (SEM). Figure 2.2.1 shows SEM images of final samples.

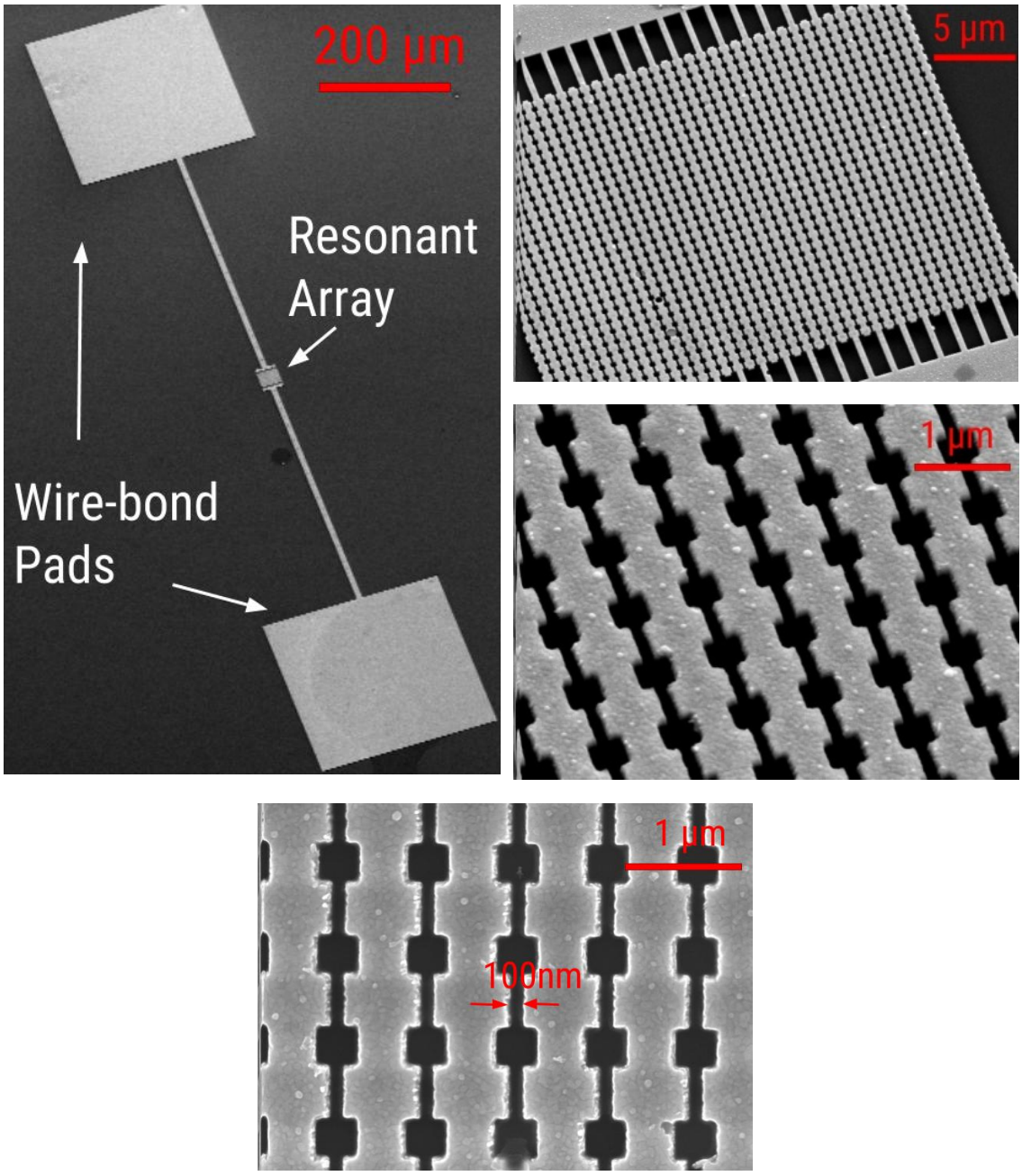

Figure 2.2.1. Scanning Electron Microscope images of samples after fabrication.

Fabricated samples were then wire-bonded in standard dual in-line packages and were ready for measurements.

2.3. Characterization and Measurement

The average field enhancement factor in fabricated samples was first confirmed using Raman spectroscopy to be approximately 10. The current-voltage characteristics were evaluated using Keithley 2410 source-meter. The measurement setup consists of a tunable Ti:Sapphire continuous-wave laser pumped with a 10 watt green semiconductor laser. The laser beam beam is first sampled for power and wavelength measurements to be done using a silicon photo-detector and spectrometer. The beam is then focused on the sample inside a vacuum chamber pumped down to 0.1 mTorr. The measured I-V characteristics curves are shown in Figure 2.3.1.

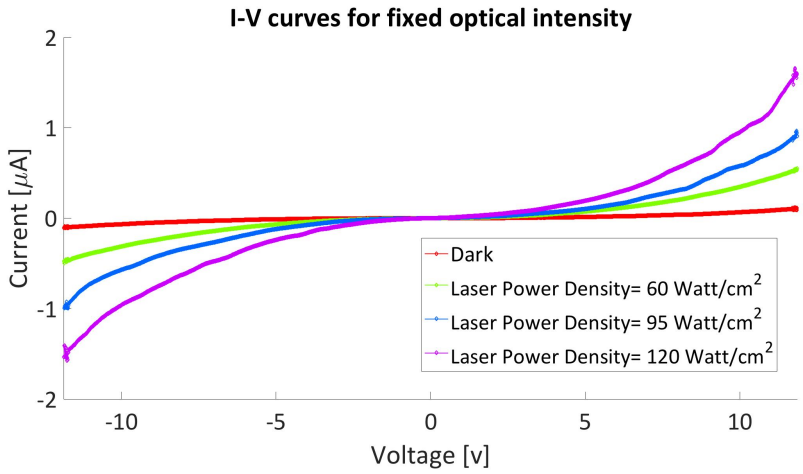

Figure 2.3.1. Measured current as a function of DC voltage, for fixed laser power intensities (0, 60, 95, and 120 $\frac{W}{cm^2}$ shown).

The laser intensity was changed from 0 to 140 $\frac{W}{cm^2}$ keeping the wavelength at 785 nm. For each fixed laser power the DC voltage was swept from -12 to 12 v

resulting in an electric field in the gap ranging from 0 to 0.12 $\frac{\mathrm{v}}{\mathrm{nm}}$. For low laser power the DC electric field is not sufficient for the electrons to overcome the potential barrier as expected; however, it is shown that the emitted current increases significantly as the optical illumination intensifies to levels as low as 10s of $\frac{\mathrm{W}}{\mathrm{cm}^2}$. This is due to the highly nonlinear light-matter interaction at the surface allowing for a combination of DC and AC field excitations.

Figure 2.3.2 shows the experimental current-voltage characteristics in the Fowler-Nordheim coordinates as discussed in Equation 1.2.6. As the DC voltage increases, slope of the curves corresponding to $\log(\frac{\mathrm{I}}{\mathrm{V}^2})$ as a function of $\frac{1}{\mathrm{V}}$ changes sign and becomes approximately linear. The inset of Figure 2.3.2 shows the linear part for voltages above 8 volts. This behavior is observed to a greater degree as the optical radiation intensifies and it confirms the fact that emitted electrons are mainly traveling through the free space.

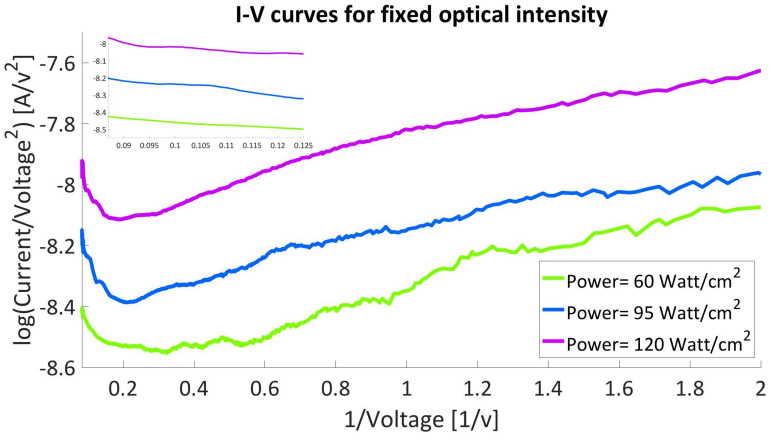

Figure 2.3.2. $\log\left(\frac{\mathrm{I}}{\mathrm{V}^2}\right) - \frac{1}{\mathrm{V}}$ Fowler-Nordheim curves for optical intensity of 60, 95, and 120 $\frac{\mathrm{W}}{\mathrm{cm}^2}$, inset for DC voltage above 8 volts.

The slope of the photocurrent curve as a function of optical intensity is an indication whether the dominant emission mechanism is multi-photon induced or optical field emission, as discussed earlier. If the electrons are mainly liberated due to n-photon absorption mechanism, $I \propto P^n$ where I is the photocurrent and P is laser power; therefore, I-P curves in logarithmic scale are linear with a slope showing the number of photons being absorbed. We have shown the I-P curves in linear (Figure 2.3.3) and logarithmic (Figure 2.3.4) scales for different measurements. The slope of I-P curves in log scale is between 1 and 2 in our measurements, indicating the dominance of one/two photon absorption mechanism.

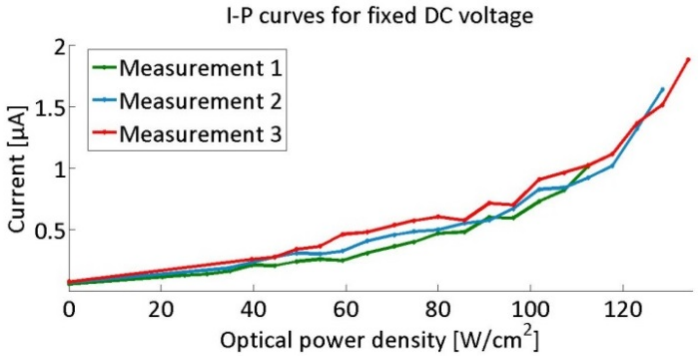

Figure 2.3.3. Current versus optical power density for fixed DC electric field ($0.11 \frac{v}{nm}$).

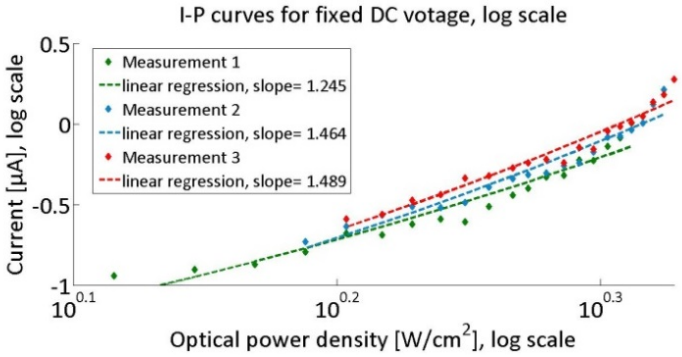

Figure 2.3.4. Current versus optical power density for fixed DC electric field ($0.11 \frac{v}{nm}$) in log scale and their linear regression, the slope is an indication of the number of photons absorbed.

2.4. Modeling and Discussion

2.4.1. Discussion of Measured Characteristics

As discussed in the first chapter, optical illumination can interact with the electron emission process by both modulating the potential barrier and increasing initial energy of electrons due to photon absorption. The confined electric field enhancement induced by resonant plasmons facilitates liberation of electrons in two ways, it provides access to high-field regions and the intense field gradient due to the nanoscale confinement enhances the ponderomotive acceleration. The plasmon-induced enhancement in this nonlinear optical process has been shown experimentally and analytically of substantial significance. Kim et al. showed that the intensity at the tip of the apex of a resonant gold bow-tie element can be enhanced up to 4 orders of magnitude by numerically solving the Maxwell's equations using FDTD calculations [35]. Ward et al. demonstrated field enhancements exceeding 1000 in nanogaps between plasmonically active gold nanostructures [41]. They extracted the enhanced electric field and tunneling conduction of nanogaps ranging from 0.03 to 0.23 nm using a continuous-wave laser at 785 nm and peak intensity of 22.6 $\frac{\mathrm{kW}}{\mathrm{cm}^2}$. Dombi et al. demonstrated the role of plasmonic field enhancement in electron emission from resonant metallic nanoparticles and showed maximized photoemission and kinetic energies at the resonance frequency [33]. It has also been shown that the work function of a resonant nanostructures supporting plasmon coupling is effectively decreased upon interaction with incoming photons by a value corresponding to the energy of the photon at the laser wavelength [26,29,32,42,43]. Thermally enhanced

field emission process is not of significant contribution for static fields below on the order of 1 $\frac{\mathrm{GV}}{\mathrm{m}}$ as discussed by Kealhofer et al. for hafnium carbide tips [24]. The maximum static field in our measurements is an order of magnitude lower than that limit and the optical field does not exceed 22.4 $\frac{\mathrm{kV}}{\mathrm{m}}$. In other words, despite the fact that the optical electric field is too small to modulate the static electric field, the nonlinearity of plasmon resonance effectively enhances the emission current.

2.4.2. Modeling the Device

There are three most widely used approaches to theoretically understand the phenomena concerned with nonlinear interaction of laser and matter, the strong-field approximation [44], the semi-classical approach [45], and the direct solution to the time-dependent Schrödinger equation. The semi-classical approach includes the two-step models dividing the process into distinct electron liberation and propagation steps. In order to model the device we have utilized the exact solution of the time-dependent Schrödinger equation at a modulated triangular potential barrier discussed by Zhang and Lau [46]. The model solves the Schrödinger equation for the complex electron wave function assuming zero potential inside the metal. Each particle can be represented by a wave function $\Psi(\mathrm{x},\mathrm{t})$ such that $\Psi\Psi^*$ gives the probability of finding the particle at that position at that time. The potential outside metal is taken as a constant DC-field induced triangular barrier modulated by a continuous AC laser field. The time-dependent Schrödinger equation is given by:

$$\mathrm{i}\hbar\frac{\partial\Psi(\mathrm{x},\mathrm{t})}{\partial\mathrm{t}} = -\frac{\hbar^2}{2\mathrm{m}}\frac{\partial^2\Psi(\mathrm{x},\mathrm{t})}{\partial\mathrm{x}^2} + \Phi(\mathrm{x},\mathrm{t})\Psi(\mathrm{x},\mathrm{t}) \qquad \textbf{Equation 2.4.1}$$

Where $\Psi(x,t)$ is the complex electron wave function, m is electron mass, and $\Phi(x,t)$ is the potential given by:

$$\Phi(x,t) = \begin{cases} 0, & x < 0 \\ V_0 - qF_0x - qF_1x\cos(wt), & x \geq 0 \end{cases} \quad \textbf{Equation 2.4.2}$$

Where V_0 is the sum of metal Fermi level and its work function.

It is shown that reflected and transmitted electron wave functions from the barrier consist of a series of ladder eigenstates with eigen-energies of $\varepsilon + n\hbar w$ corresponding to sub-bands available by n-photon absorption (n>0) or emission (n<0) where ε is the surface normal energy of incident electron. These eigen-energies include both the drift kinetic energy and the ponderomotive energy of electron quiver motion. Solution of the wave function outside the metal is the superposition of plane waves corresponding to each sub-band and weighed by its transmission amplitude.

Using the boundary conditions of continuity of both Ψ and $\frac{d\Psi}{dx}$ at the metal-vacuum interface it is possible to obtain the transmission and reflectance amplitude of each eigen-state, T_n and R_n, respectively and thus the solution of the time-dependent wave function inside and outside metal. The probability current density is then given using:

$$J(x,t) = \frac{i\hbar}{2m}(\Psi\nabla\Psi^* - \Psi^*\nabla\Psi) = \frac{i\hbar}{2m}\sum_{n=-\infty}^{\infty}\sum_{l=-\infty}^{\infty}(\Psi_n\nabla\Psi_l^* - \Psi_n^*\nabla\Psi_l) \quad \textbf{Equation 2.4.3}$$

The normalized emission current density defined as the ratio of the transmitted current density over the incident current density is then calculated using:

$$w(\varepsilon, x, t) \equiv \frac{J_t(\varepsilon,x,t)}{J_i(\varepsilon)}$$ **Equation 2.4.3**

In our model, we used optical field enhancement β and effective work function ϕ_{eff} as the control parameters to fit the measured data to analytical solution, assuming optical illumination at 785 nm and electrons being initially at the Fermi level [22,29,31,43,46]. The model does not include the reduction of barrier height due to image charge effects and solves the Schrödinger equation assuming a sharp triangular barrier; however, as shown by Zhang and Lau [46] it can be used for realistic potentials including the image charge effects by replacing the work function with reduced ϕ_{eff}.

2.4.3. Comparison Between Analytical Solution and Measurements

In order to fit both constant DC field and constant AC field curves to the analytical solution, the effective work function of gold had to be reduced to 3.3 eV. This reduction is slightly higher than the energy of a photon at 785 nm (1.58 eV), suggesting a combination of one and two photon absorption at the surface. The optical field at the surface had to be enhanced by 3 orders of magnitude in order to reach measured current levels. Figure 2.4.1 and 2.4.2 show that the analytical I-V characteristic of the device falls within the range of measured data for each optical intensity.

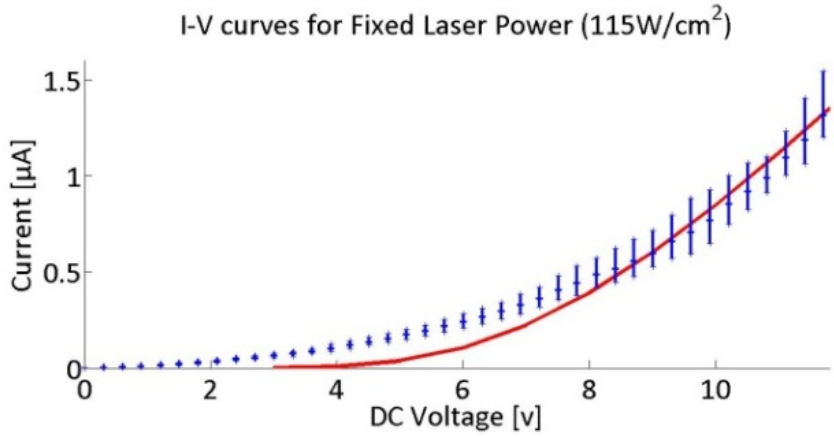

Figure 2.4.1. Comparison between analytical model and measurement results. I-V curves at radiation intensity= 115 $\frac{W}{cm^2}$, analytical solution (solid, red), measured data (blue).

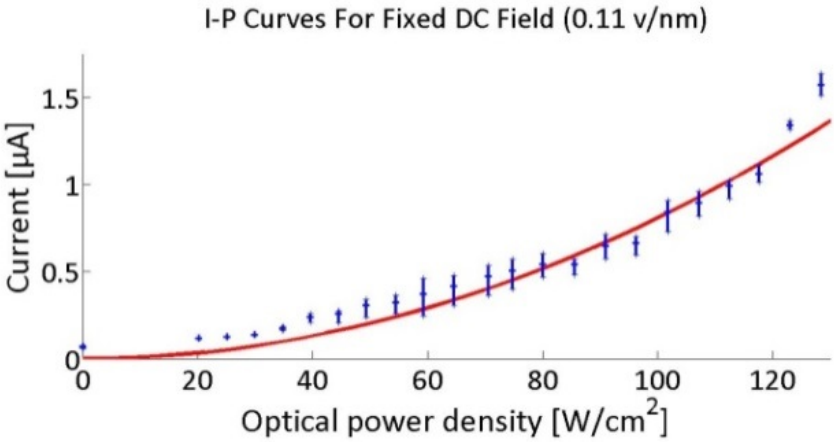

Figure 2.4.2. Comparison between analytical model and measurement results. I-P curves at DC field= 0.11 $\frac{V}{nm}$, analytical solution (solid, red), measured data (blue).

Figure 2.4.3 shows the effect of combination of DC and AC excitation in electron emission. The maximum laser intensity even after applying the enhancement factor in the model is below 0.04 $\frac{v}{nm}$ which is considerably smaller than the DC field to have a significant effect on the current; however, due to the nonlinear properties of the laser-matter interaction, the consequent photocurrent is increased substantially.

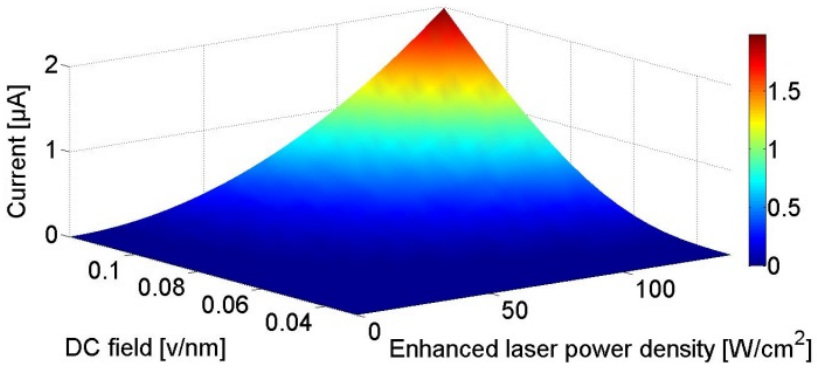

Figure 2.4.3. Total time averaged current as a function of DC field and enhanced laser power density based on analytical solution.

The analytical model does not include the induced field inside the metal and assumes a zero potential inside gold. The extracted surface field enhancement is also compatible with values obtained by Ward et al. [41] at 785 nm and optical peak intensity of 22.6 $\frac{\mathrm{kW}}{\mathrm{cm}^2}$. The surface enhancement mechanism has been previously utilized in ultrafast free electron generation [29,30,47]. It has also been discussed that photo-assisted field emission process can be favored over multi-photon over-the-barrier photoemission due to the increase in tunneling probability of electrons through an optically modified barrier [26]. Therefore, it appears from our experiments that the optical excitation at the resonance wavelength of the surface reduces the gold work function at least by one photon energy. Additionally, the enhanced optical field induces sufficient modulation of the barrier to make it narrow enough at parts of the optical cycle for the electrons to tunnel through after absorption of one or two photon energies. The obtained photocurrent based on the analytical model strongly agrees with the measured values in terms of both DC voltage and optical power levels as depicted in Figure 2.4.1 and 2.4.2, respectively.

2.5. Summary

In summary, we have designed, fabricated, and modeled a plasmon-induced photoemission based vacuum-channel device enabling efficient combination of DC and AC field induced emission of electrons. Meanwhile neither solely optical nor DC excitation per se provides sufficient energy for the electrons to overcome the barrier, their highly nonlinear interaction at the interface results in significant photocurrent which has been characterized in our measurements. The laser and DC power levels required for electron emission are substantially reduced ($\frac{\mathrm{W}}{\mathrm{cm}^2}$ optical intensity and less than 10 v DC bias) in a simple planar metallic surface due to the plasmon-induced sub-wavelength field concentration and manipulation. The effective work function of gold and the optical electric field enhancement factor at the surface have been quantified using the exact solution of the time-dependent Schrödinger equation in a field- modulated triangular barrier. It is shown that the experimental results fit well in the analytical model having an effective work function of 3.3 ev and a field enhancement of 1800. Utilization of the resonant field enhancement in this periodic structure addresses the challenges of efficient generation of carriers in vacuum-channel devices and can be taken advantage of in a variety of applications including nano-scale photonic circuits, photovoltaics, and photochemistry.

Chapter 2, in part, has been submitted for publication of the material as it may appear in: S. Piltan, D. Sievenpiper, “Field Enhancement in Plasmonic Nanostructures”. The dissertation author was the primary author of this material.

Chapter 3

Variations of the Resonant Surface and Their Properties

In chapter 2, we showed the idea behind design process of the periodic surface used as a tool for efficient combination of static fields and optical radiation taking advantage of the plasmonic field enhancement. Since the spectral and field intensity properties of the resonance depend highly on the geometry, a number of various layouts and applications can be proposed using similar background notion. In this chapter, we first discuss the design and fabrication of a variation of the resonant periodic surface. Then, we demonstrate scaling properties of the current with the area. Finally, we characterize the field enhancement using a direct application of Fowler-Nordheim equations.

3.1. Geometrical Control over Field Enhancement

The geometry of the metallic resonance array is very flexible and it can be modified into various configurations. These variations include asymmetric configurations for rectification purposes (discussed in Chapter 4) and scaled dimensions for addressing infrared frequencies (discussed in Chapter 5). It is also possible to add extra ports for modulation of current in one port using the voltage on the other one [40]. This transistor-like behavior was shown using suspended mushroom-like structures for electrical and optical manipulation of electric field intensity in hot spots.

In this chapter, we used this degree of freedom to introduce higher enhancement factors in a periodic surface. The measured results confirm operation in high-field region and clearly have Fowler-Nordheim behavior. The geometry here consists of an array of sharp triangular unit-cells as shown in Figure 3.1.1. The vacuum gap is formed between the tips of unit-cells on two adjacent rows. Every other row is connected to a different terminal on two sides of the array and the bias voltage is applied through these terminals. While under normal conditions the vacuum gap prevents conductance between the two sharp terminals until the DC bias voltage reaches levels up to 100s of volts, this surface supports localized surface plasmon resonances in near-infrared and enables combination of photonic and electric excitations. Due to the sharp tip geometry of unit-cells the sensitivity of the surface to optical excitation is enhanced and electron emission and acceleration occurs at lower power intensities.

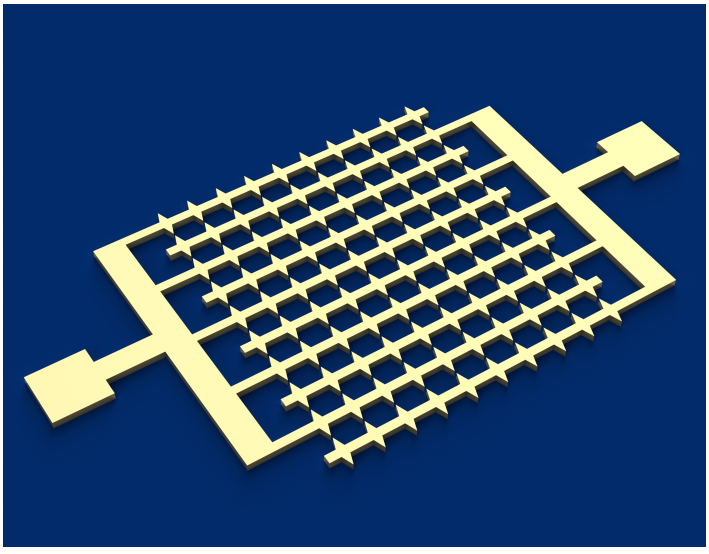

Figure 3.1.1. Modified flat structure for enhanced field intensity.

3.2. Design and Optimization

The geometrical parameters need to be optimized for hot-spots to occur at the surface of the triangular tips. Figure 3.2.1 shows a simulation unit-cell. The structure is simulated using HFSS electromagnetics tool based on the finite-element method and Johnson-Christy model for the complex dielectric constant properties of gold [39]. The unit-cell in Figure 3.2.1 is designed over a 280 nm silicon dioxide layer of isolation on top of silicon substrate. The exact thickness of the silicon dioxide layer is obtained experimentally using Filmetrics F20 general-purpose film thickness measurement instrument.

While the top and bottom boundaries are set as radiation boundary, the vertical boundaries were set as perfect electric and perfect magnetic conductors to enable simulation of an infinite array. Due to periodicity in both directions, it is possible to simulate only a quarter of unit-cell.

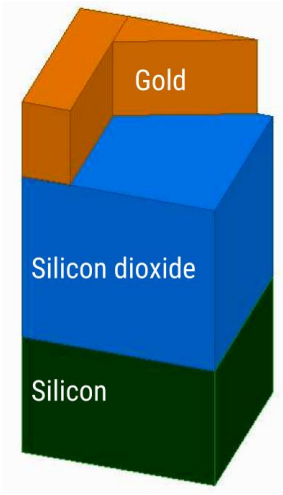

Figure 3.2.1. Simulation unit-cell. Symmetry of the design and periodicity of the boundary conditions allow simulation of only quarter of unit-cell.

The excitation in our simulations is set as a plane wave with magnitude of 1 v/m polarized in direction of axis of the sharp tip and vertically incident on it. The optimizations are done for maximizing the electric field at the tip of the triangular cell at 785 nm wavelength. The geometric parameters to be simulated are shown in Figure 3.2.2. The vacuum gap between the tips G, is set to be 50 nm wide which was close to the fabrication limit achievable in the nanofabrication facilities used. The wider this gap the less intense the electric field enhancement at the tip. The rest of the dimensions to be optimized include length of the triangular tip L, the sharpness angle θ, the separation distance between triangular elements on the same row T, the width of each row connecting unit-cells W, and the thickness of the gold layer H.

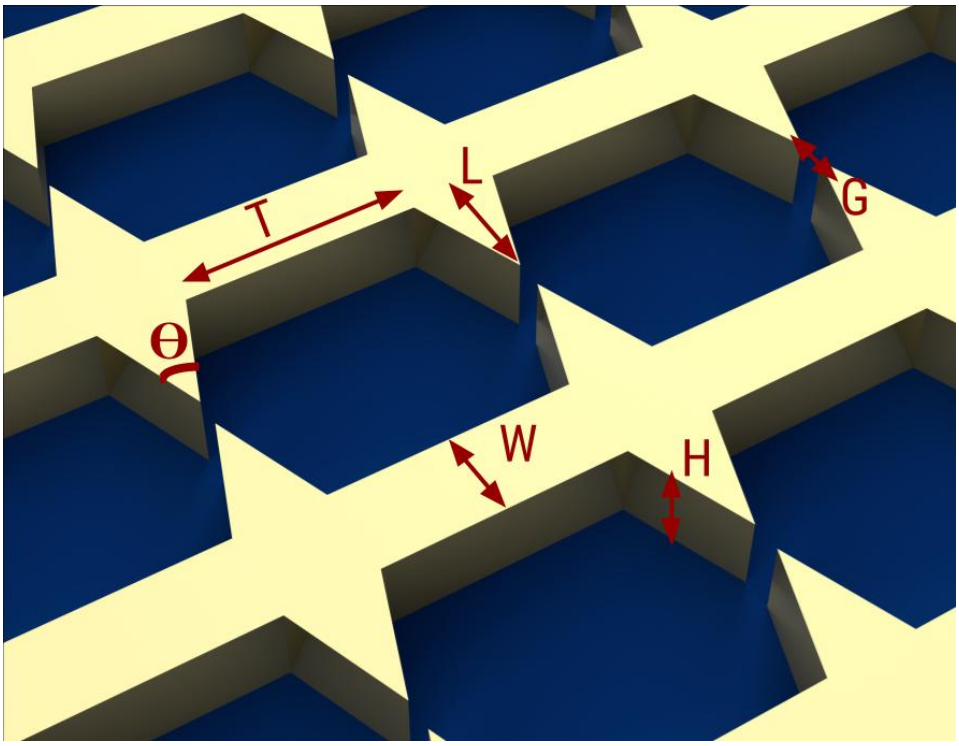

Figure 3.2.2. Multiple unit-cells of the triangular array and the simulated geometric parameters.

Field enhancement is defined as the ratio of the electric field at any point to the incident field and it is maximized for the point at the tip of the triangular element at a vertical distance from silicon dioxide substrate equal to half the total gold thickness. The optimized dimensions for excitation at 785 nm are T= 400 nm, L= 200 nm, W= 150 nm, θ= 40 degrees, and H= 130 nm. Figure 3.2.3 demonstrates the field enhancement value as a function of frequency for two points, on the substrate and 65 nm above silicon dioxide substrate, both on the tip edge.

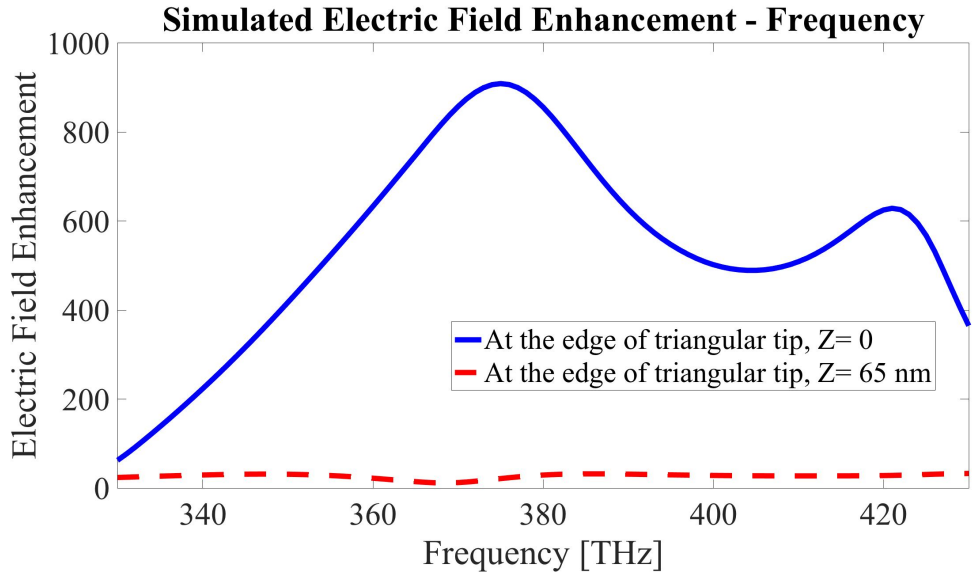

Figure 3.2.3. Simulated field enhancement as a function of frequency for final optimized dimensions, solid (blue) at the edge of the triangular tip on the substrate, dashed (red) at the edge of the triangular tip 65 nm above substrate.

The simulation results show relatively wide-band enhancement of electric fields and a maximum of approximately 810 at 382 THz. The field profile is such that the maximum enhancement factor falls closest to the metal-vacuum interface facilitating electron emission process. Figure 3.2.4 and 3.2.5 show the electric field profile at λ= 785 nm on the side and top interfaces of the half unit-cell, respectively.

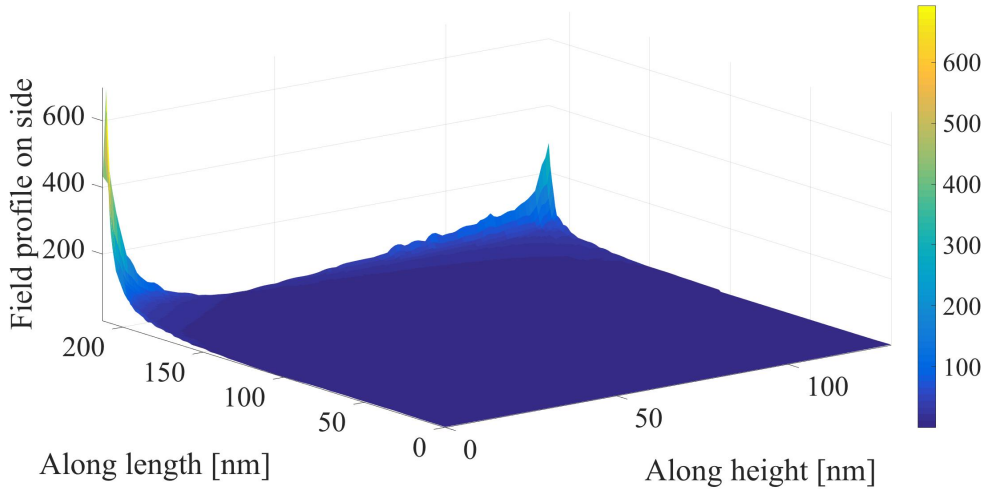

Figure 3.2.4. Simulated field enhancement profile on the side interface of triangular half unit-cell upon incident of plane wave at 785 nm polarized along the tip axis.

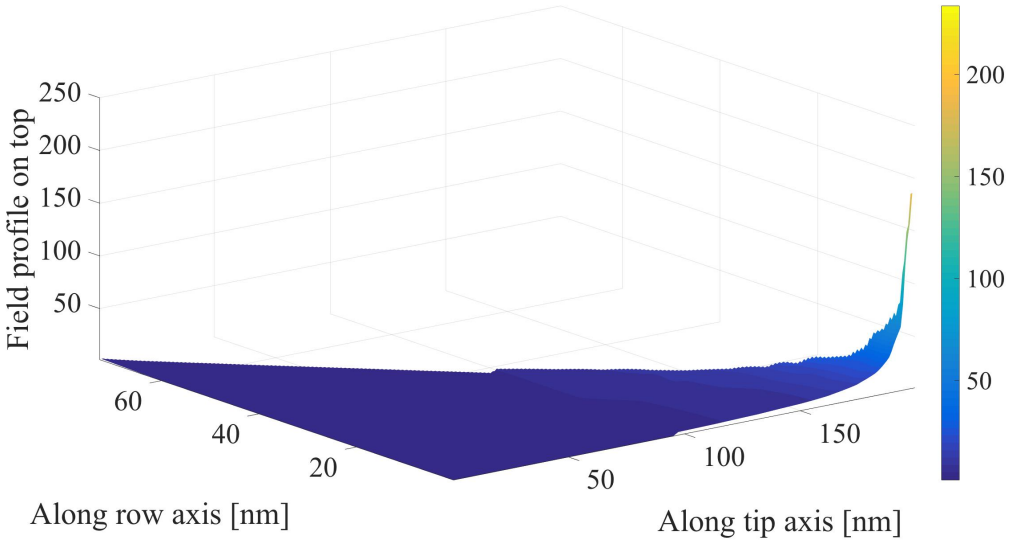

Figure 3.2.5. Simulated field enhancement profile on the top interface of triangular half unit-cell upon incident of plane wave at 785 nm polarized along the tip axis.

The simulated field profiles show enhancement factors as large as approximately 700 on parts of the emitting area at $\lambda = 785$ nm. In other words, although the field enhancement has a smaller average value over the entire interface

the photocurrent contribution of parts of the emitting area, specifically top and bottom edges of the tip, is significantly larger.

Figure 3.2.5 shows the electric field enhancement as a function of distance from the triangular tip for three different heights above the substrate, 130 nm or at the top of the edge, 65 nm or at the mid-point of the gold thickness, and on the substrate. The electric field value drops quickly with distance from surface and reaches a relatively similar value towards the middle point of the vacuum gap regardless of the vertical distance above substrate. This brings up the idea of utilizing this behavior for building geometrically asymmetric structures providing field enhancement in only one electrode. In that case, electrons can be liberated only from the metal edge at the high-field side and not from the other and it can provide rectification properties in optical frequencies. This idea is discussed in Chapter 4.

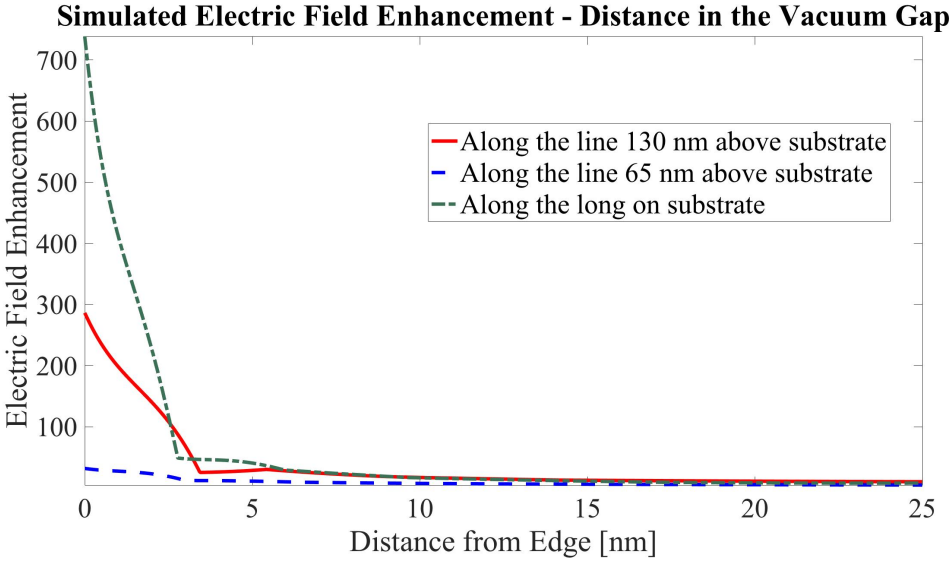

Figure 3.2.6. Simulated field enhancement in the vacuum gap as a function of distance from gap edge for three different vertical distances from substrate, 130 nm (top), 65 nm (middle), and on substrate, upon incident of plane wave at 785 nm polarized along the tip axis.

3.3. Fabrication

A 40x40 layout of the periodic unit-cells was fabricated on silicon wafers with a 280 nm thermally oxide SiO_2 layer to minimize leakage currents through substrate. The silicon wafers had a resistivity above 10000 Ω.cm and the thickness of SiO2 layer is sufficient for proper isolation [40]. The layout was exposed using electron beam lithography technique (Vistec EBPG5200 50/100 KV high performance nanolithography system) on a 300 nm thick layer of polymethyl methacrylate resists spin coated for 45 seconds with 2000 rpm and baked for 60 seconds on a 180 °C hot plate. After development and a 5 second O_2 plasma cleaning session, the layout was metallized using electron beam evaporation (Temescal's BJD 1800 e-beam evaporator) of a 5 nm chromium adhesion layer and subsequently a 125 nm gold layer. The lift-off process was overnight using Remover PG and subsequently in ultrasonic bath using acetone. The two-step lift-off process helps successful fabrication of the 50 nm gap in entire area of the array.

Figure 3.3.1 shows scanning electron microscope (FEI XL30-SFEG high-resolution scanning electron microscope) images of the fabricated arrays. The fabricated samples were finally diced and wire bonded in dual-standard packages.

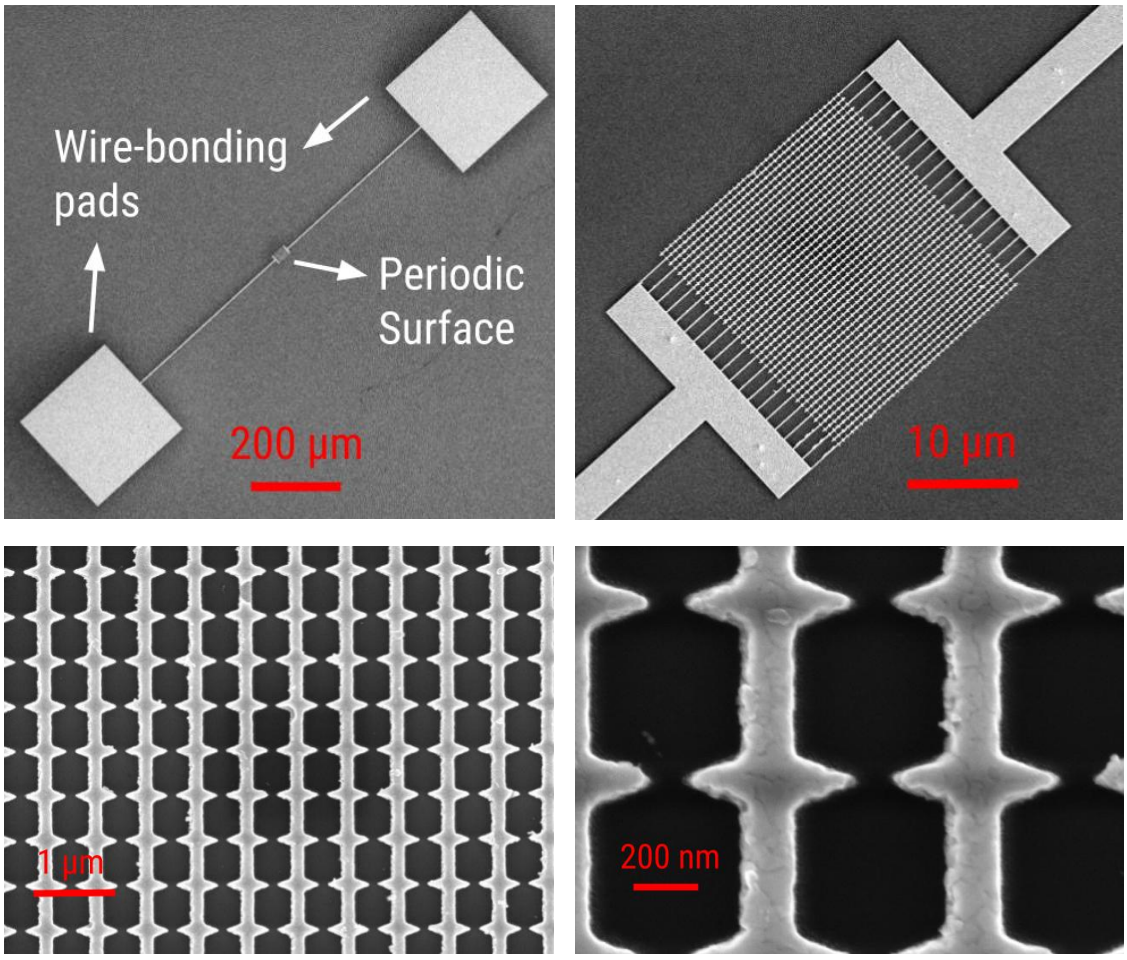

Figure 3.3.1. Scanning electron microscope images of periodic surface after fabrication.

3.4. Characterization and Measurement

The measurement setup is similar to what discussed in Chapter 2. The sample is located inside a vacuum chamber pumped down to 0.1 mTorr and the current-voltage characteristic is measured using Keithley 2410 source-meter. Optical excitation is provided by a tunable Ti:Sapphire continuous-wave laser pumped with a 10 watt green semiconductor laser with wavelength centered at 785 nm and beam radius of 0.475 mm. The measured current-voltage curves for various radiation power densities are shown in Figure 3.4.1.

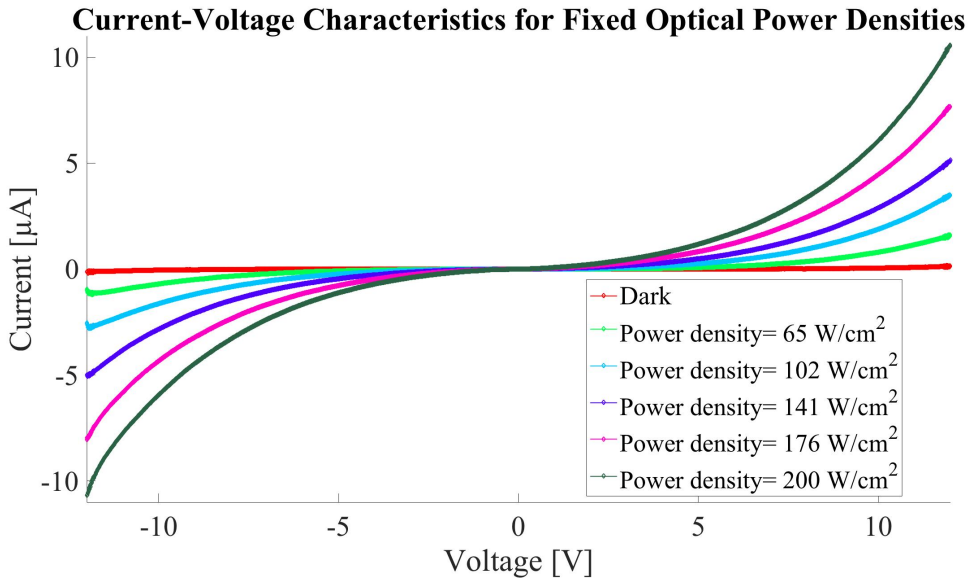

Figure 3.4.1. Measured current-voltage characteristics for the triangular sharp tip array for fixed radiation intensities centered at 785 nm (0, 65, 102, 141, 176, and 200 $\frac{W}{cm^2}$ shown).

It is observed that the photocurrent increases substantially by application of optical radiation at the resonant frequency. Also, the boosted effective electric field enhancement factor and the shorter gap size in the sharp tip structure compared to the flat emitting surface discussed in Chapter 2 are reflected in the amplified photocurrent for identical electrical and photonic powers.

Repeating the current-voltage characteristic measurements for a wide range of optical powers provides curves corresponding to photocurrent as a function of radiation power density for fixed electrical bias as shown in Figure 3.4.2.

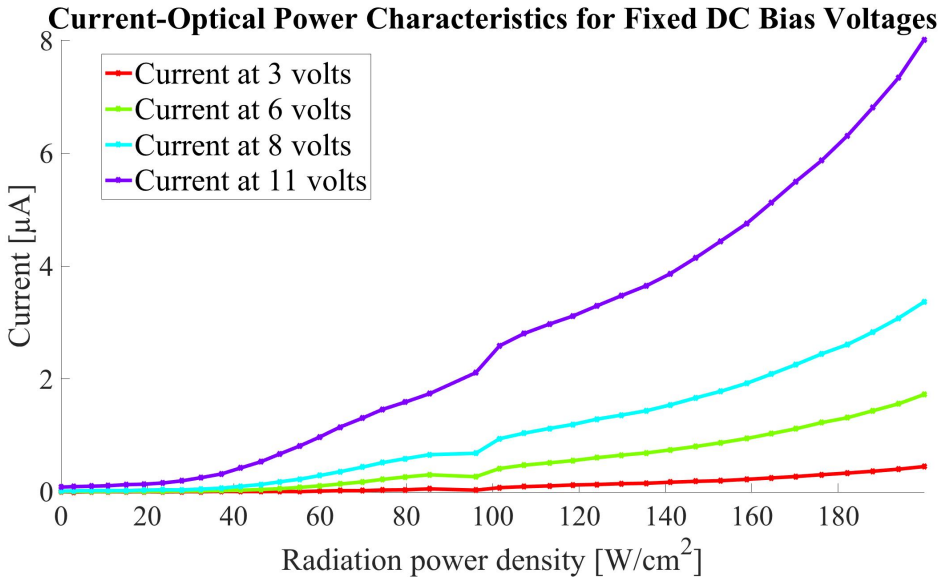

Figure 3.4.2. Measured current-optical power characteristics for the triangular sharp tip array for fixed DC bias voltages (3, 6, 8, and 11 volts shown).

3.5. Scaling Property of Photocurrent with Surface Area

Since every single cell contributes to the photocurrent, it is expected for the current to scale with the area of the array. Scaling is an important property because it can compensate for low effective quantum efficiency and it introduces new applications such as alternatives for solar harvesting cells. An scaled array will have a larger current handling capacity and it will increase the damage threshold of the device. In order to confirm this behavior, we fabricated an 80x80 periodic array of the same structure and compared the measured photocurrent for identical static fields and optical radiations in the scaled array with the original size. Figure 3.5.1 demonstrates scanning electron microscope images of the scaled array. The resulting photocurrent as a function of optical power density for multiple voltages is shown in Figure 3.5.2.

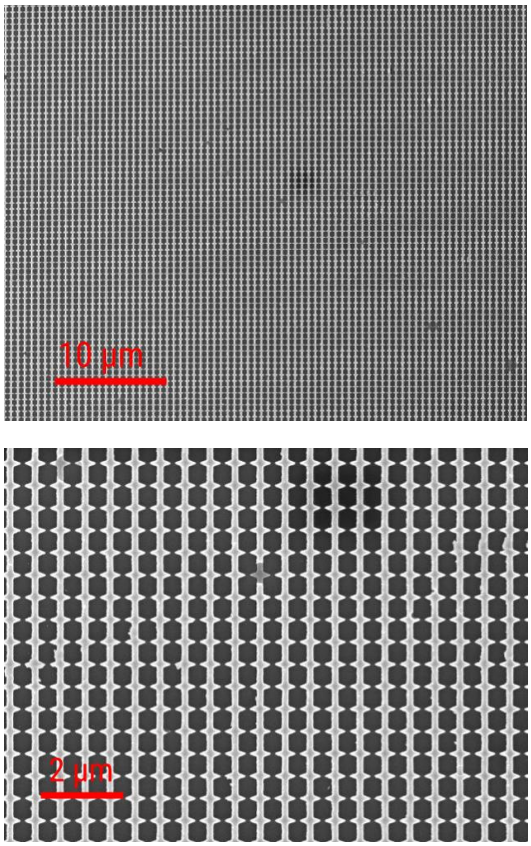

Figure 3.5.1. Scanning electron microscope images of the 80x80 element array.

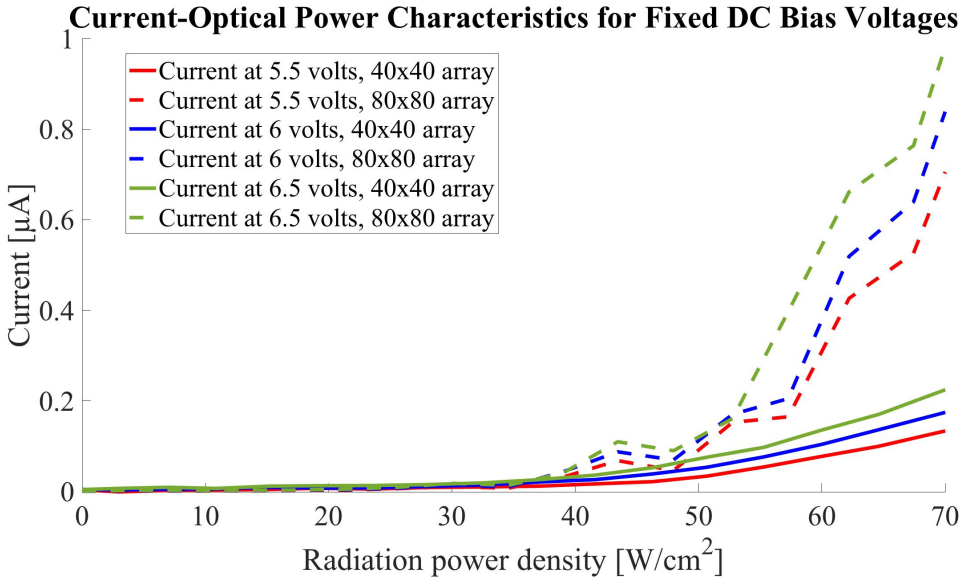

Figure 3.5.2. Measured current-optical power characteristics for fixed DC bias voltages (5.5, 6, and 6.5 volts shown) for 40x40 and 80x80 element surface.

Figure 3.5.2 clearly shows the scaling behavior of photocurrent with surface area for a variety of DC and optical powers. Since the array size in each dimension is doubled, the emitted current in the 80x80 element array is approximately 4 times bigger than the 40x40 surface.

3.6. Analytical Field Enhancement Factor Extraction

As discussed in chapter 1, plotting the current-voltage characteristic curves in Fowler-Nordheim coordinates ($\log\left(\frac{I}{V^2}\right) - \frac{1}{V}$) gives useful insight on the electron emission processes. Figure 3.6.1 demonstrates the measured current-voltage characteristics in these coordinates. Note that the horizontal coordinate spans from 0.5 volt to 12 volts.

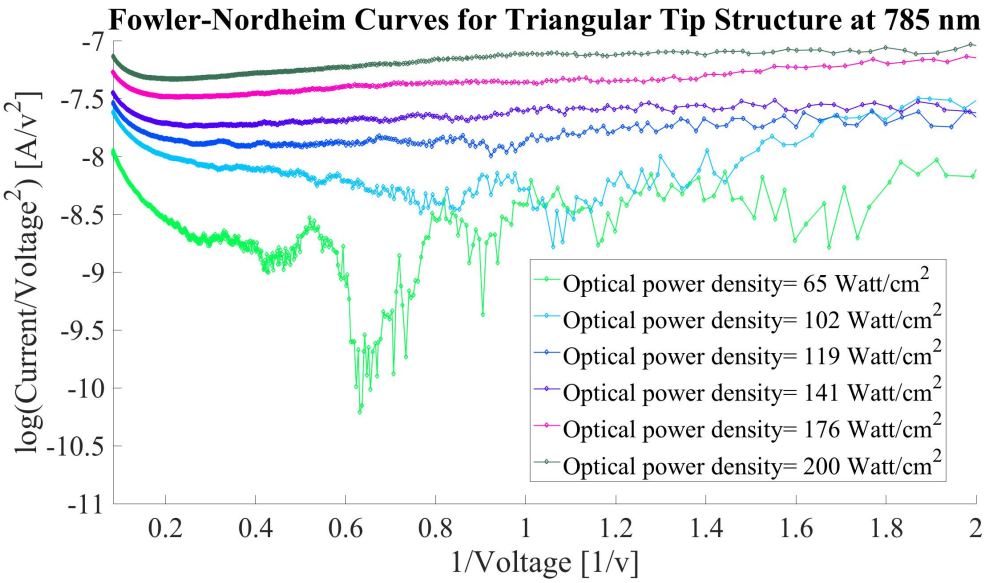

Figure 3.6.1. Measured $\log\left(\frac{I}{V^2}\right) - \frac{1}{V}$ characteristics for the triangular sharp tip array for fixed radiation intensities centered at 785 nm (0, 65, 102, 141, 176, and 200 $\frac{W}{cm^2}$ shown).

In the high-field regime, the relationship between current and voltage is approximately given by Equation 1.2.6 (Fowler-Nordheim equation) by substituting the total field as the sum of the static field and optical oscillating field. When the device operates in this regime, the $\log\left(\frac{I}{F^2}\right)$ curves as a function of $\frac{1}{F}$ change slope and become linear with a negative slope. The slope is given by $\frac{B\phi^{3/2}}{\beta}$ where β is field enhancement factor at the surface, ϕ is the effective work function, and B is the second Fowler-Nordheim constant equal to $\frac{8\pi\sqrt{2m}}{3hq} = 6.83\ [eV^{-3/2}\ V\ nm^{-1}]$.

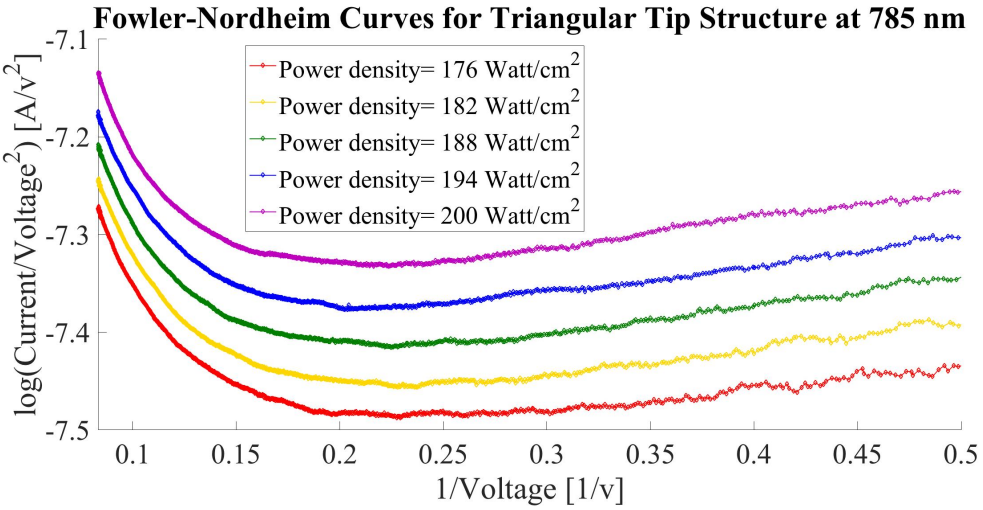

Figure 3.6.2. Measured $\log\left(\frac{I}{V^2}\right) - \frac{1}{V}$ characteristics for the triangular sharp tip array for fixed radiation intensities centered at 785 nm (176, 182, 188, 194, and 200 $\frac{W}{cm^2}$ shown).

This slope is used in the high-field approximation to extract the value of electric field enhancement at the surface for known values of work function and external field because direct measurement of the enhancement factor still remains a challenging task. Figure 3.6.2 shows the Fowler-Nordheim curves we utilized for this

analysis. The curves in Figure 3.6.2 are plotted for DC voltages above 2 volts and for optical intensities demonstrating the linear behavior most clearly. The linear behavior also confirms emission of electrons through the free space rather than leakage currents through substrate.

Next we extracted the slopes of the linear regression of the high-field part of the curves as shown in Figure 3.6.3. The horizontal axis spans from 10.5 volts to 12 volts in order to insure high-field linear behavior.

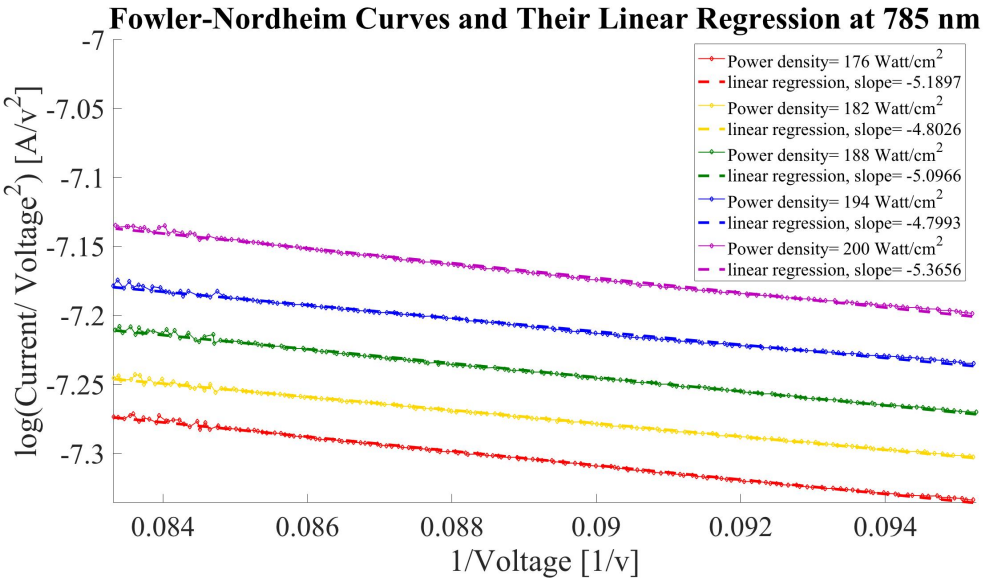

Figure 3.6.3. Measured $\log\left(\frac{I}{V^2}\right) - \frac{1}{V}$ characteristics for the triangular sharp tip array for fixed radiation intensities centered at 785 nm (176, 182, 188, 194, and 200 $\frac{W}{cm^2}$ shown), and their linear regression.

It is shown in Figure 3.6.3 that the slope of $\log\left(\frac{I}{V^2}\right) - \frac{1}{V}$ remains relatively constant for various optical intensities as long as the device is operating in the linear regime. Although the extracted value of enhancement factor is inversely proportional to $\phi^{3/2}$where ϕ is the effective work function of the metal, we assumed the work

function remains unchanged for this calculation due to optical excitation. We used a value of 5.1 eV for work function of gold. We also assumed the gap size is 50 nm. In other words, we extracted the maximum field at the tip of the triangular surface.

Based on these calculations Figure 3.6.4 shows the field enhancement factor as a function of optical intensity.

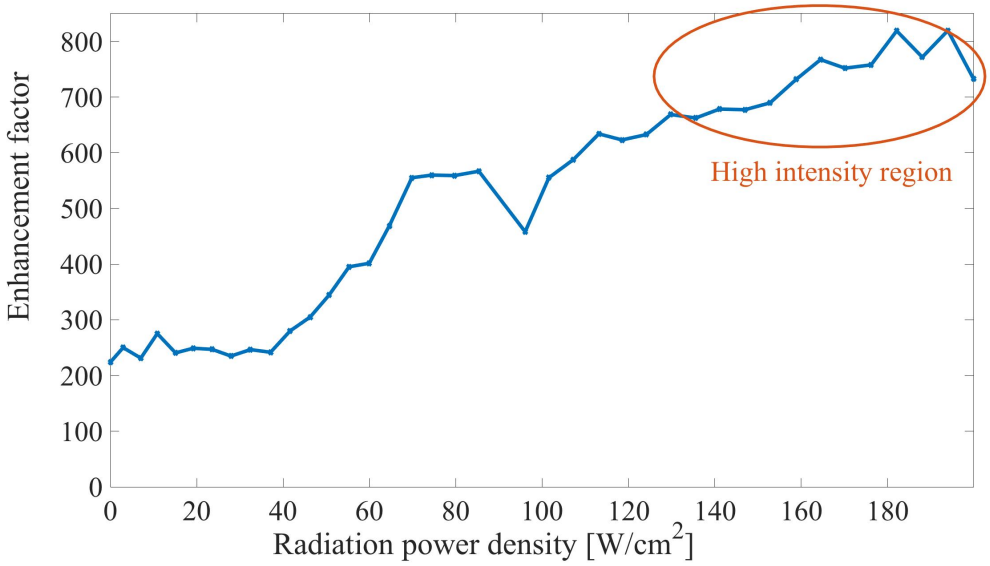

Figure 3.6.4. Field enhancement factor as a function of optical power density extracted using the slope of measured Fowler-Nordheim type cuves for 50 nm gap size and 5.1 eV gold work function.

The extracted field enhancement values at the edge of triangular tip first increase with radiation power density and then become relatively constant at a value between 700 and 850 for the high intensity region. Since current-voltage characteristics of device does show as clear linear behavior in the low intensity region as the high power region it is not possible to use the linear approximation for power densities below approximately 130 $\frac{W}{cm^2}$. The combination of multi-photon emission mechanisms for field intensities below this value plays an important role in

photocurrent. As the radiation intensifies the optical field emission contributes more to the emitted current and the linear approximation of Fowler-Nordheim curves results in a more accurate value for electric field enhancement at the tip. Based on this analysis for optical field intensities shown in Figure 3.6.3, the extracted field enhancement factor has an average value of 780.

3.7. Summary

In this chapter, we demonstrated a modification of the design discussed in Chapter 2. We took advantage of the geometric degree of freedom to achieve higher simulated electric field enhancement factors at the tip of a triangular gold unit-cell. We discussed fabrication of the device and showed the current-voltage characteristics measured. We used the high-field approximation of the Fowler-Nordheim relationship between current and voltage for a combination of static and oscillating electric fields. We demonstrated the fact that $\log\left(\frac{I}{V^2}\right) - \frac{1}{V}$ curves behave linearly for high static and optical field intensities. Using the slope of this curve we extracted the field enhancement factor at the tip edge to be on average 780 for a value of 5.1 eV for gold work function. This value shows the enhancement factor on the surface which otherwise is a challenging parameter to be directly measured.

Chapter 3, in part, is currently being prepared for submission for publication of the material as it may appear in: S. Piltan, D. Sievenpiper, “Plasmonic Nano-arrays for Enhanced Photoemission and Photodetection”. The dissertation author was the primary author of this material.

Chapter 4

Optical Rectification Using Geometrical Field Enhancement in Gold Nano-arrays

Conversion of photons to electrical energy has a wide variety of applications including imaging, solar energy harvesting, and IR detection. A rectenna device consists of an antenna in addition to a rectifying element to absorb the incident radiation within a certain frequency range. We designed, fabricated, and measured an optical rectifier taking advantage of asymmetrical field enhancement for forward and reverse currents due to geometrical constraints. The gold nano-structures as well as the geometrical parameters offer enhanced light-matter interaction at 382 THz. Using the Taylor expansion of the time-dependent current as a function of the external bias and oscillating optical excitation we obtained responsivities close to quantum limit of operation. This geometrical approach can offer an efficient, broadband, and scalable solution for energy conversion and detection in the future.

4.1. Introduction

There has been a growing demand for alternative broadband electromagnetic wave transducers in order to collect radiation from infrared through visible frequencies. A variety of such devices have been used in antenna-based photovoltaics and IR detectors [48,49,50]. Enhanced light-matter interaction in optical antennas facilitates conversion of photons into localized electrical energy. Other applications

include nanophotonics, near-field optics, medical imaging, chemical sensors, and optical detection [36,41,51,52]. Solar and waste heat energy harvesting applications are of particular interest; on the other hand, they present new challenges since they require efficient operation at zero external bias.

Solar harvesting is conventionally implemented using photovoltaic p-n junction cells; however, semiconductor cells fall short in absorption of low-energy photons and are limited by the band-gap for high-energy photons. As discussed by Shockley and Queisser in 1961, ultimate efficiency is fundamentally limited to 30% in single junction [53] and to 55% in multi-junction cells [54]. Also, implementation of p-n junction cells generally requires challenging materials.

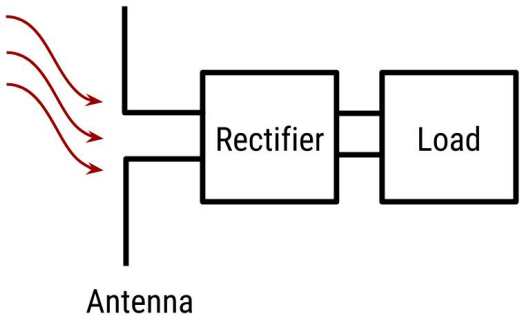

Figure 4.1.1. Block diagram of rectenna device attached to a load.

An alternative approach for energy transduction is utilization of rectennas. Rectennas consist of two main elements, an antenna and a tunnel junction for DC rectification as demonstrated in Figure 4.1.1. Incident electromagnetic waves are first collected through the antenna and converted to guided modes. The oscillation of charges on antenna induced by incident fields gives rise to alternating currents. The

resulting currents are then rectified through the diode element to be effectively used on the load.

Compared with the conventional semiconductor cells rectennas also enable photon to DC current conversion; however, they are speculated to have higher efficiency in THz [55]. Integrating the demodulating element of the transducer with the antenna enhances signal to noise ratio by minimizing signal pathway length in addition to providing another degree of freedom by control over geometry [52]. They operate based on the wave nature of light rather than the particle form; therefore, they are limited by cutoff frequency of the device instead of band-gap energy [55]. Furthermore, the small efficiency of rectennas can be compensated by scalable area and low cost. They are speculated to be an attractive addition to current energy harvesting technology [52].

4.2. Rectenna Challenges

There has been considerable effort in addressing the challenges of both the antenna and the rectifying element in the optical frequency spectrum. Antenna resonance at optical frequencies requires sub-wavelength dimensions as well as small inductance and capacitance. Solving this problem requires complicated fabrication processes and substantial computing power to design the nano-scale structures that are required. Various designs including dipole, bowtie [56,57], spiral, and thin wire antennas using carbon nanotube or nanowire arrays [58,59,60] have been theoretically and experimentally demonstrated.

In order to capture the AC radiation in form of a rectified DC current, there needs to be an asymmetrical charge flow mechanism for the forward and reverse bias. Material, thermal, and geometrical asymmetries have been used to provide the barrier difference at zero bias [48]. The response time of the rectifying device to optical radiation needs to be on the order of 10^{-15} to 10^{-13} seconds for the electrons to be able to cross the junction before field reversal. The most widely used diode categories for high-speed rectification are semiconductor p-n junction, Schottky, and MIM diodes. Rectification in p-n junctions is limited to gigahertz frequencies due to charge transit time [52,61]. Novel Schottky diodes have been used in terahertz frequencies but they are conventionally limited to below 5 THz [52,62,63]. MIM tunnel diodes are reproducible and mechanically strong; however, their speed is fundamentally restricted to below 150 THz due to RC time constant constraint [52,64,65].

There are three main factors limiting the speed of rectification. The first aspect is the tunneling time of electrons which is found to be in the femtosecond range [66,67] and is not in principle restraining optical rectification. Another limiting factor is the electron transit time in the junction. For a constant frequency of operation this imposes a maximum on the gap distance referred to as the characteristic distance. In other words, the maximum time electrons take to travel from one electrode to another needs to be smaller than one-half period of the incident optical radiation, otherwise they are back accelerated before they reach the electrode. The characteristic gap width was experimentally measured for the STM W/Si (111) junction by keeping the incident wavelength of a yttrium-aluminum-garnet laser fixed at 1.06 μm and

increasing the gap width [68]. The cutoff distance for the tungsten tip defined as the distance at which the rectified current is -3 dB from the value at the onset point at zero bias was found to be 2.5 nm in this case. Assuming simple kinematical equations between velocity and time for particle traversal, Sullivan et al. extracted the corresponding velocity of tunneling electrons to be approximately 10^8 cm/s on the order of Fermi velocity of electron at the tip [64]. This brings up the idea that electrons from states around the Fermi level act "classically" as they tunnel through the barrier from one electrode to another following kinematical motion equation; however, there is no a priori rationale for this in the classically inaccessible barrier [64]. The confined field enhancement induced by resonant plasmons facilitates electron liberation both by providing access to high-field regions and by enhancement of ponderomotive acceleration of electrons due to the substantial field gradient of this nanoscale confinement.

There are two limiting cases used for modeling the emission behavior. The first is when the period of radiation is significantly larger than the interaction time of electrons with the barrier at a given incident energy. In this case, particles observe an effectively static barrier and can traverse before field reversal. The second case is when the optical oscillation period is smaller than the interaction time of electrons [48]. The photocurrent of this behavior is determined by the additional energy states from where electron can tunnel through. Charge carriers in this way can travel from side-bands corresponding to either absorption or emission of a multitude of photon energy quanta in that frequency. This means electrons previously at energy level ε

may now be located at $\varepsilon+n\hbar\Omega$, where $\hbar$ is the reduced Planck constant, Ω is the frequency of the optical oscillation, and n is the number of absorbed or emitted photons [69]. The amplitude of probability of an electron being found at energy level $\varepsilon+n\hbar\Omega$ is given by solution of the wave function satisfying Hamiltonian in the presence of the oscillating field and is shown to be the Bessel function of order n [69,70]. Another parameter equivalently characterizing the transition between photon-driven and field-driven regimes is the Keldysh parameter defined as the ratio of the incident optical frequency to the characteristic tunneling frequency of metal as discussed in Chapter 1. For relatively weak fields where Keldysh parameter is above 1, the quiver amplitude of electrons in the applied field is smaller than the decay length of the near field; therefore, electrons are back accelerated before they are liberated and the dominant process is multi-photon induced emission. The local slope of the photocurrent as a function of laser intensity drops as the dominant mechanism changes from multi-photon induced emission to optical field emission. Here, we take advantage of the ponderomotive acceleration due to resonant field enhancement to overcome the transit time constraint for wider gap distances.

The third limiting factor of rectification speed is the electro-dynamical response time demonstrated in form of an RC time constant. For planar MIM junctions, in order to reach capacitances small enough for efficient rectification in the optical part of the frequency spectrum, the junction area needs to shrink down to as small as approximately 10x10 nm^2 [52]. However, the consequent junction resistance for such small areas is intolerably high [71,72]. A sufficiently low resistance is

desirable for matching between the antenna and diode impedances and it is crucial for efficient power transfer between them. As a result of this trade-off, parallel MIM devices are unable to provide the required RC time constant for an efficient operation in optical frequencies. Even though metal multi-insulator metal diodes provide a smaller resistance and superior matching for a given capacitance, they still suffer from this RC time constant constraint [52]. Point contact and sharp-tip diodes provide a faster response since the RC time constant is a function of contact area in this case. It has been demonstrated that the sharper the tip, the higher the rectification ratio and the faster the speed [48,73]. Other solutions to faster rectification include traveling-wave MIM and geometric diodes [74,75,76]. Traveling-wave diodes suffer from relatively higher resistive losses in metal but they have been shown to have better performance in wavelengths above 3 μm [75]. Geometric diodes on the other hand, do not take advantage of material or thermal asymmetries for their rectification mechanism. They rather provide a larger field enhancement on one electrode rather than the other resulting in an asymmetrical charge transport probability even at zero bias. This rectification mechanism has been verified both theoretically [67,77] and experimentally [41,78,79]. Zhu et al. have successfully used the funneling effect of sloped edges in a graphene geometrical diode to rectify radiation of a CO_2 laser at 28.3 THz [79]. The critical dimension of the funnel neck needs to be on the order of the mean free path length of electrons in material imposing challenges in fabrication. The choice of graphene is due to its relatively large mean free path length of electrons around 1 μm [80]. In another study [41], Ward et al. demonstrated optical rectification

of a 785 nm laser source using a geometrically asymmetrical sub-nm junction. They applied the Tien- Gordon approach [69] for theoretical analysis of their measured I-V characteristics in gold nanostructures and extracted field enhancement factors on the order of 10^3 at the surface. Here, we exploit a similar plasmonic field enhancement mechanism in a gold nano-array of geometrically asymmetric unit-cells to obtain rectification in gaps as wide as 50 nm. Other challenges to be addressed besides speed limitations include impedance matching for efficient power transfer, high zero-bias responsivity, maximum near field enhancement, complicated theoretical analysis, and fabrication.

4.3. Design and Optimization

Here, we take advantage of both the plasmonic resonant field enhancement at a sharp gold tip and the asymmetrical transmission probability of electrons in a geometrically optimized array of unit-cells to obtain DC rectification upon excitation with a laser beam at 785 nm. The antenna and rectifying elements of the rectenna are embedded in a single cell. This eliminates the challenging matching requirements between the antenna and diode impedances and reduces the signal path length, which in turn decreases the losses in material. It also helps to enhance signal to noise ratio by minimizing noise pick-up.

Each unit-cell consists of a triangular sharp tip facing a 50 nm wide flat electrode with 50 nm of gap in between as shown in Figure 4.3.1. We used a finite element numerical simulator (Ansys HFSS) in order to optimize dimensions for maximized field enhancement at the sharp tip when illuminated by a normally incident

plane wave at 785 nm wavelength polarized in the direction of the tip axis. We also applied the Johnson and Christy [39] model for complex dielectric properties of gold at optical frequencies. The gold unit-cell is simulated on an isolating SiO_2 layer of 280 nm thickness on a silicon wafer. Different geometric parameters including the period of unit-cells, triangular tip length, and sharpness angle were optimized to excite an electric field mode in optical frequencies with maximum enhancement at the sharp tip and minimum on the flat electrode. The goal is to have electrons tunnel through in one direction due to field-induced high transmission probability. Figure 4.3.1 demonstrates the consequent final dimensions. The overall array consists of one mutual flat electrode going around all sharp electrodes as shown in Figure 4.3.2. The other two terminals are each connected to a series of sharp cells on different sides.

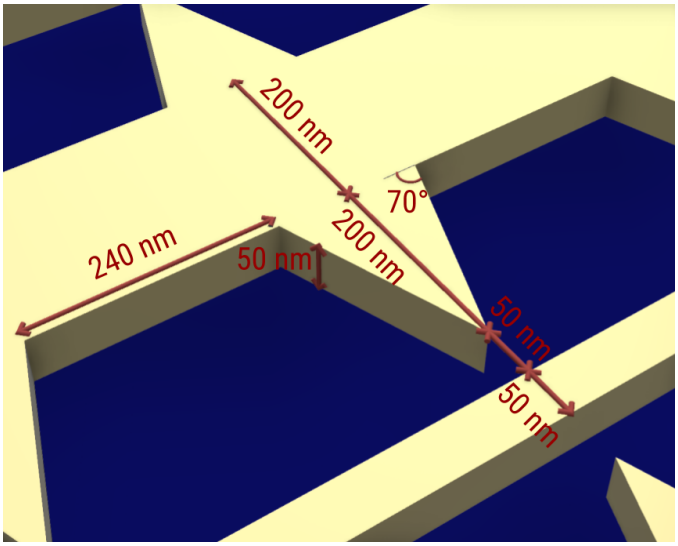

Figure 4.3.1. Schematic of designed resonant optical rectifier. Rectifying unit-cell of geometrically asymmetrical electrodes with 50 nm air gap in between, optimized for maximum field enhancement at the sharp tip.

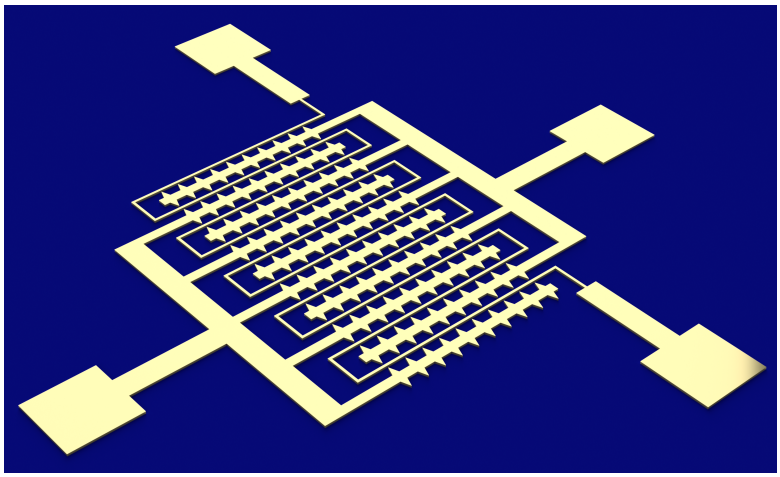

Figure 4.3.2. Schematic of designed resonant optical rectifier. Resonant array consisting of 3 terminals, the flat electrode terminal and two sharp tip terminals. One of the sharp tip terminals is grounded in our measurements.

The simulation results for the optimized geometry and the field profile is shown in Figure 4.3.3 and 4.3.4, respectively. The field enhancement is defined as the ratio of electric field at any point to the incident field. Figure 4.3.3 shows this ratio at four points, on the sharp electrode and on the flat one, at 25 nm and 50 nm above substrate height. Due to the geometrical constraints, the sharp tip provides a relatively large field enhancement over a broad frequency spectrum, with a with a maximum value of approximately 125 at 370 THz. Simulations demonstrate a field ratio of approximately 43 between the sharp electrode and flat electrode at 50 nm above substrate and at frequency equal to 370 THz, meaning for the same DC bias a much smaller optical power is required to liberate electrons from the sharp electrode than the flat one. The asymmetrical field profile is shown in Figure 4.3.4.

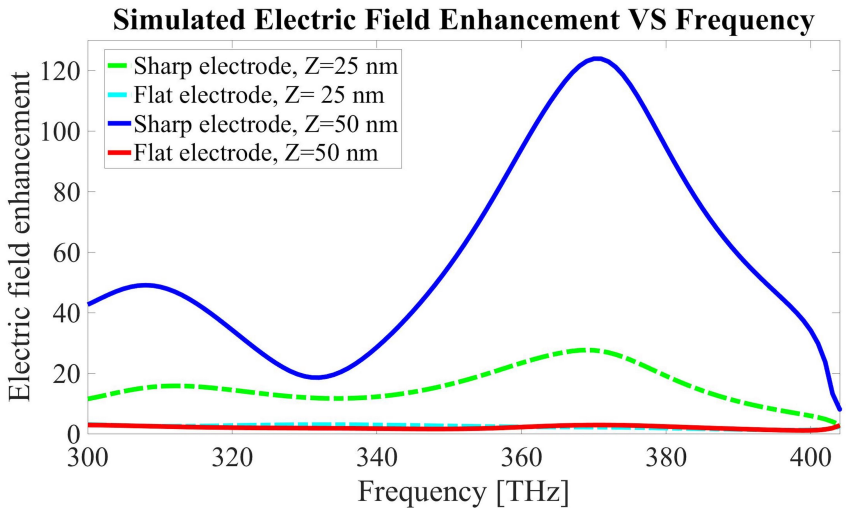

Figure 4.3.3. Simulation results. Electric field enhancement 25 nm above the substrate on the sharp electrode (green) and flat electrode (cyan), and 50 nm above the substrate on the sharp electrode (blue) and flat electrode (red), as a function of frequency.

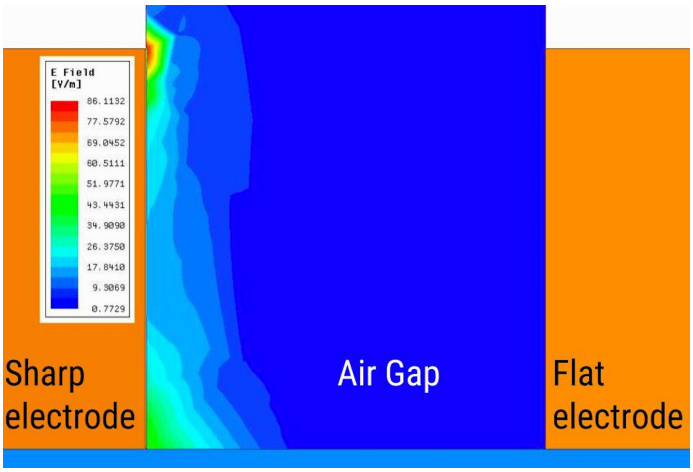

Figure 4.3.4. Simulation results at 382 THz. Side view of asymmetrical field profile in the air gap between the electrodes showing different field ratios on each side.

4.4. Fabrication

Fabrication of samples was done using a single step of e-beam lithography on silicon wafers with a 280 nm SiO_2 layer for isolation to minimize the leakage current through substrate.

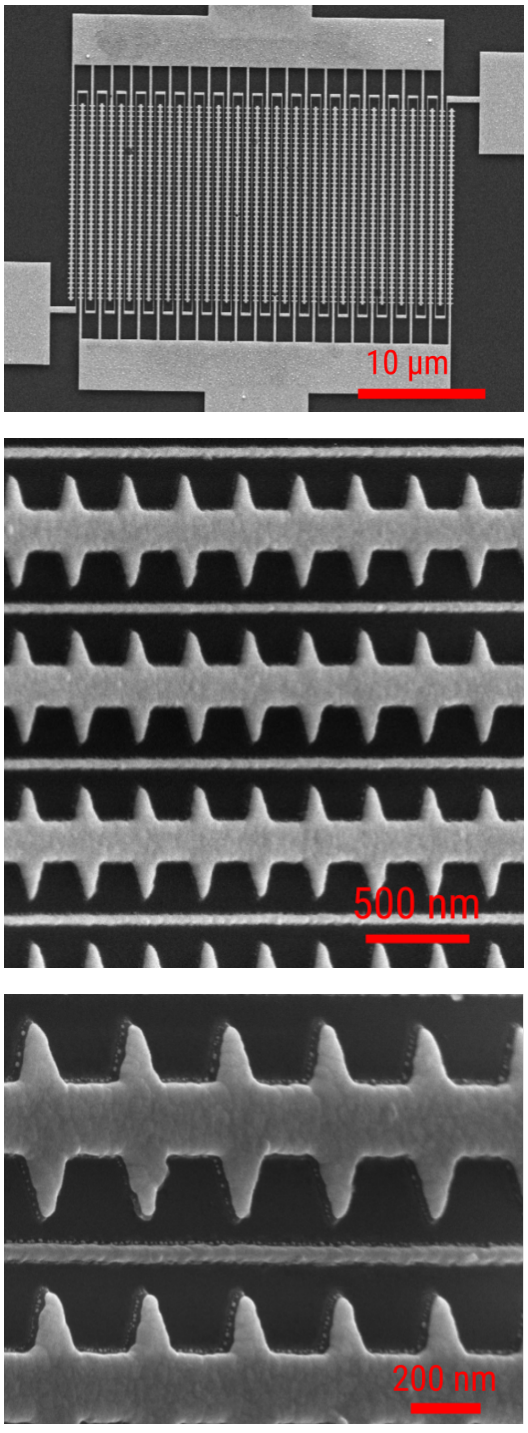

Figure 4.4.1. Scanning electron microscope images of fabricated samples.

The silicon wafers had a resistivity above 10000 Ω cm and the thickness of SiO_2 layer is enough for proper isolation [81]. A 5 nm chromium adhesion layer and a 50 nm gold layer were later electron beam evaporated on exposed samples. Lift-off was done using Remover PG over-night and subsequently using acetone in an ultrasonic bath. Each sample consists of a 40x40 array of unit-cells. The fabricated samples were then wire-bonded in standard dual in- line packages. Figure 4.4.1 shows scanning electron microscope images of fabricated samples. One end of the flat terminal was left open even though a wire-bonding pad was considered in the layout for that end as well. Alternating rows of the triangular unit-cells are connected together on each side of the array. One wire-bonding pad is connected to each side and one side is grounded. The other pad is used for I-V measurements.

4.5. Characterization and Measurement

The measurement setup consists of a tunable Ti:Sapphire continuous wave laser pumped with a 10 watt green semiconductor laser. The laser beam is first sampled for power and wavelength measurements to be done using a silicon photo-detector and spectrometer. The beam is then focused on the sample inside a vacuum chamber pumped down to 0.1 mTorr. Two source- meters simultaneously measure the currents through the flat terminal and the sharp terminal. Each of the source-meters can be set into an amp-meter, volt-meter, or to source voltage and measure currents for different setups. This way we can make sure the electrons emitted in one terminal are mainly collected through the other. Schematic of the measurement setup connections are shown in Figure 4.5.1.

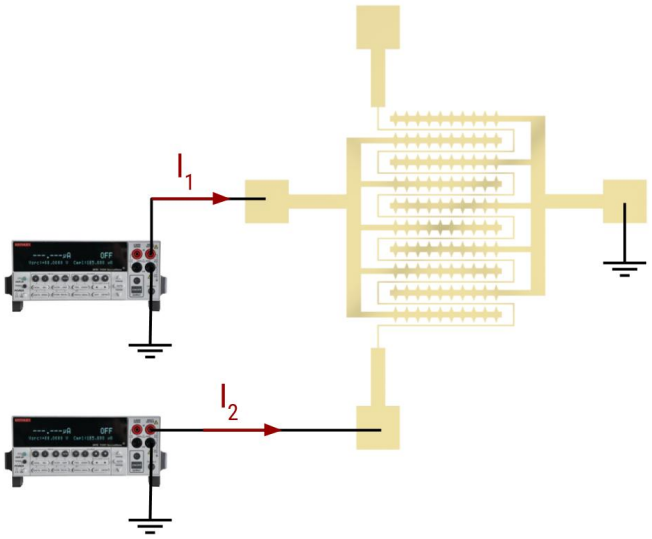

Figure 4.5.1. Measurement setup for rectifying structure. Two source- meters simultaneously measure the currents through the flat terminal and the sharp terminal.

A variety of combination of applied voltages and measured currents through different terminals is performed to characterize the device. First consider the case when the voltage is applied by source-meter 1 through the sharp tip terminal. Current through the sharp terminal I_1 and current through the flat terminal I_2 are measured simultaneously as shown in Figure 4.5.2. The measured current-voltage characteristic of the device measured through the sharp terminal is shown in Figure 4.5.2. Each measurement is repeated for various laser power densities ranging from 0 to 90 $\frac{W}{cm^2}$, keeping the wavelength at 785 nm. Figure 4.5.3 demonstrates the emitted current as a function of laser power density for various voltages. It is clear that photocurrent is not significantly affected by increasing laser intensity for reverse bias. The change in local slope of the curves associated with forward bias in Figure 4.5.3 indicates that the

dominant emission mechanism changes from multi-photon induced emission to optical field emission as optical radiation intensifies.

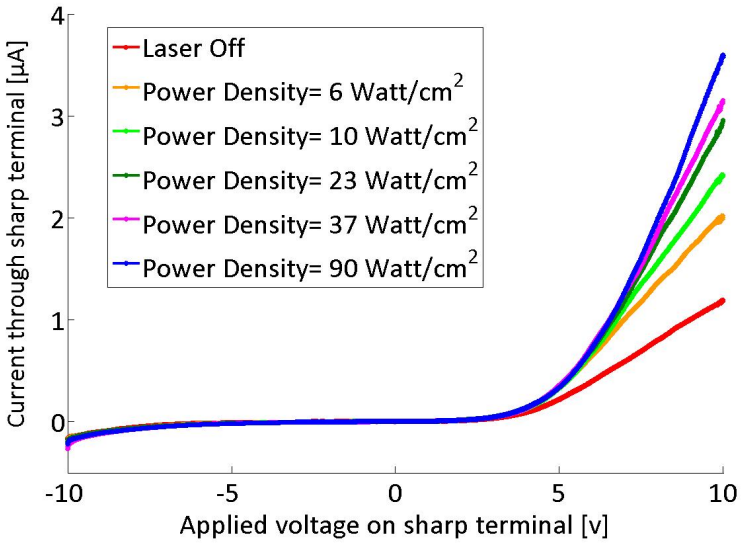

Figure 4.5.2. Measured I-V characteristics for various laser power densities, current on sharp terminal as a function of voltage over it.

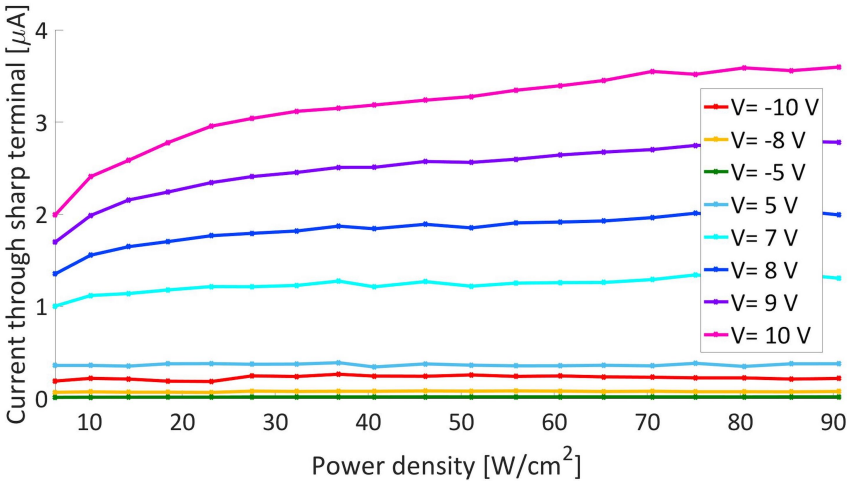

Figure 4.5.3. Measured I-P characteristics at various DC bias voltages on sharp terminal.

Meanwhile, current through the flat terminal is measured simultaneously and it is found to be approximately equal to the current measured on the sharp terminal with a difference in sign as shown in Figure 4.5.4.

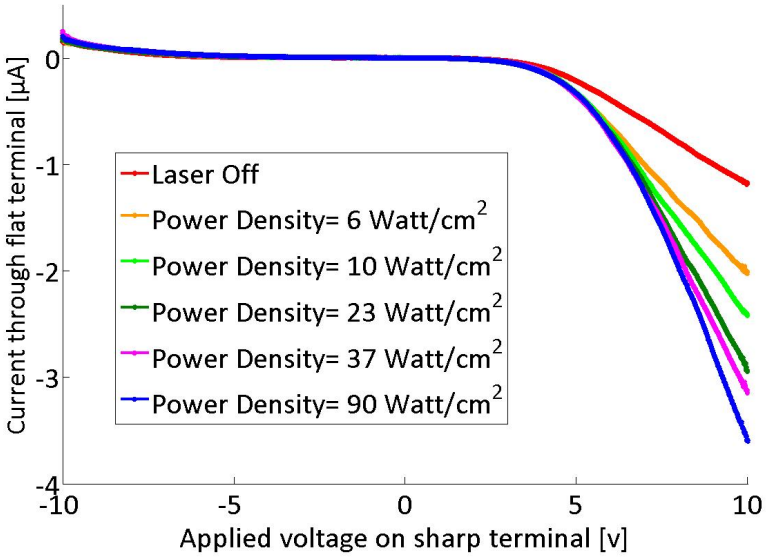

Figure 4.5.4. Measured I-V characteristics for various laser power densities, current on flat terminal as a function of voltage over sharp terminal.

Incident radiation induces oscillating charges at the geometrically asymmetric tunneling junction. Due to the finite effective mass of electrons, the phase lag between oscillating electrons and the electromagnetic field increases with frequency. The coulomb interaction with metal ions acts as the restoring force. The amplitude of the charge oscillation is maximized when the phase lag is increased to 90 degrees [36]. This frequency corresponds to the localized surface plasmon resonance frequency in metals and results in enhanced electric field near the surface. As discussed previously, we took advantage of geometrically induced asymmetric enhancement factor at the junction to obtain asymmetrical I-V curves as shown in Figure 4.5.2 and 4.5.4. Current-voltage characteristic curves using this method show obvious asymmetrical behavior. Figure 4.5.4 confirms the fact that approximately all electrons emitted from

the sharp terminal are collected by flat terminal since simultaneous measurements of current show equal values for both terminal with a difference in sign.

Emitted current increases as the optical illumination intensifies due to the highly nonlinear light-matter interaction at the surface. Similar geometrical rectification in optical frequencies has been studied both experimentally and theoretically. Bragas et al. [82] reported a field enhancement factor between 300 and 600 on gold tips used in scanning tunneling microscope illuminated at 670 nm. They demonstrated optical rectification based on both thermal and geometrical asymmetry. The asymmetrical behavior is once again confirmed when switching the voltage source location to the flat terminal. Figure 4.5.5 and 4.5.6 show the measured curves if the voltage is applied through source-meter 2 on the flat terminal and currents through the flat and sharp terminals are simultaneously measured.

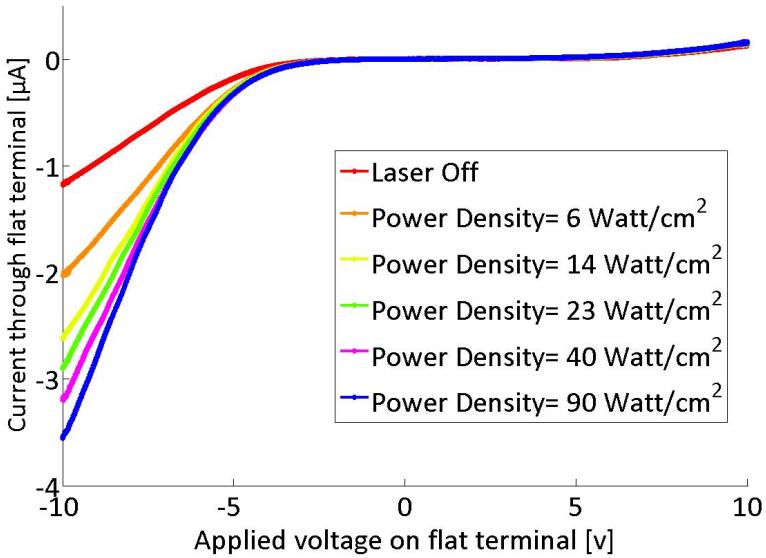

Figure 4.5.5. Measured I-V characteristics for various laser power densities, current on flat terminal as a function of voltage over it.

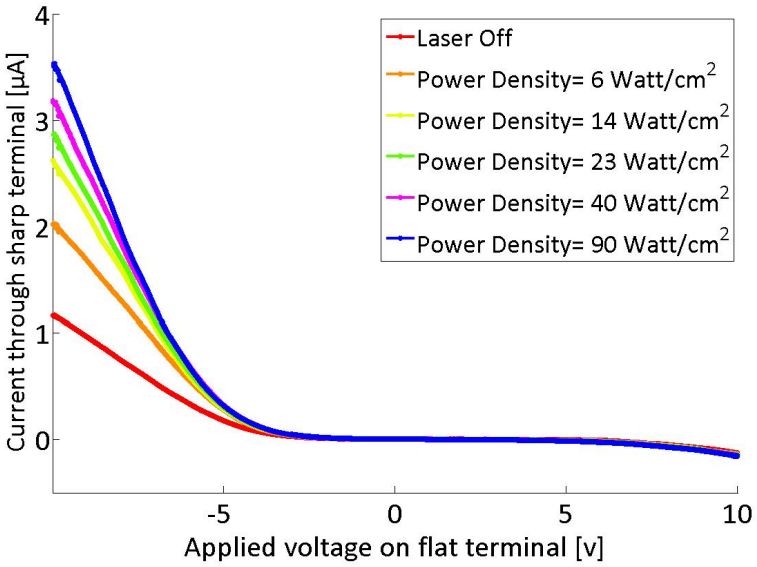

Figure 4.5.6. Measured I-V characteristics for various laser power densities, current on sharp terminal as a function of voltage over flat terminal.

It can be observed in Figure 4.5.5 and 4.5.6 that this time emission occurs in negative voltages, which effectively is equivalent to positive voltage in previous setup. Also, the currents have the same sign if emission occurs in both setups. This means only one electrode is capable of emission of electrons and current flows only in one direction. This confirms the rectification of incident radiation at 785 nm.

4.6. Modeling and Discussion

In order to model the measured characteristics, we use a method suggested by Mayer et al. in a series of papers [77,83,84,85,86] presenting a transfer-matrix analysis of a metal-vacuum-metal junction under oscillating potential and its dependence on physical and geometrical parameters. They first [83] demonstrated a quasi-static approximation and later [84] extended the solution taking the time-dependence of the potential into account by using a Floquet expansion of the wave function. They

generalized their previous work for various dielectric functions [85] and confirmed the role of plasmonic resonances in field enhancement and rectification in junctions using silver and tungsten tips. Their model suggests enhanced rectification ratio at resonant polarization frequencies of the tip and shows increased contribution of multi-photon processes at resonance. In their following work, they derived a classical responsivity [86] based on the Taylor-expansion of the static I-V characteristics for variable aspect ratio and work function, then [77] compared it with quantum responsivity defined from currents actually achieved in an oscillating barrier. Using a similar approach, we fit the measured I-V characteristics of the device into a higher order polynomial and use the following definitions for device responsivity, resistance, asymmetry, and nonlinearity [55]:

$$S(V) = \frac{d^2I}{dV^2}(V) \Big/ \frac{dI}{dV}(V)$$ Responsivity **Equation 4.6.1**

$$R(V) = 1 \Big/ \frac{dI}{dV}(V)$$ Resistance **Equation 4.6.2**

$$f_{asym}(V) = \left| \frac{I_{Forward}(V)}{I_{Reverse}(V)} \right|$$ Asymmetry **Equation 4.6.3**

$$f_{NL}(V) = \frac{dI}{dV}(V) \Big/ \frac{I(V)}{V}$$ Nonlinearity **Equation 4.6.4**

Here, classical responsivity is defined as the output DC current per unit power input. Although photon absorption increases the tunneling probability and currents in visible frequencies, we can use this approximation in the limit of small AC amplitudes [41]. Figure 4.6.1 shows responsivity as a function of applied voltage for various

optical powers at λ= 785 nm. Since quantum efficiency is limited to a maximum of one electron per incident photon, responsivity as defined above at this frequency is limited to 1.2663 A/W.

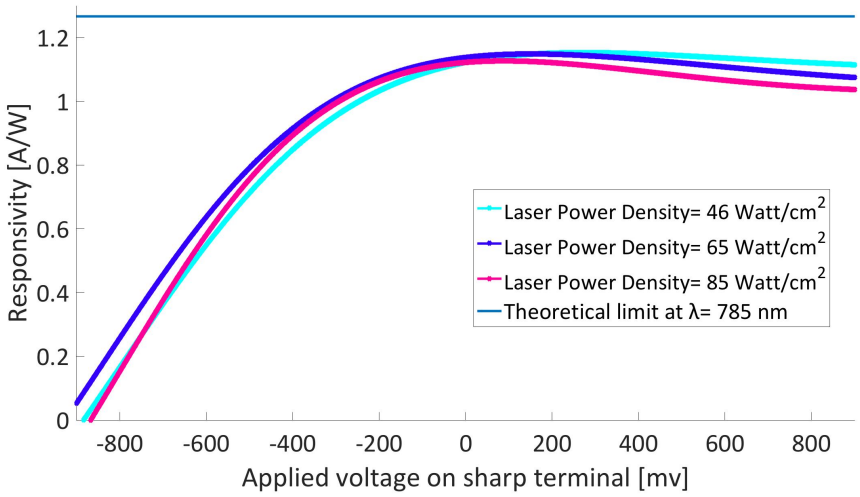

Figure 4.6.1. Diode figures of merit calculated from measured I-V characteristic using a model based on Taylor expansion of current in oscillating potential, Responsivity based on classical definition limited to 1.2663 at λ= 785 nm.

Zero-bias responsivity is specifically critical in energy harvesting applications. Zhu et al. [79] demonstrated a thin-film graphene geometric diode providing rectification of radiation from a 28 THz CO_2 laser coupled to an optical antenna. Their reported zero-bias responsivity defined as the half the ratio of second and first derivatives of the current-voltage characteristic at 28 THz is calculated to be 0.12 A/W, with a quantum limit of 8.5 A/W. Gadalla et al. [87] designed a rectenna based on a resonant bow-tie antenna and a rectifier realized between the antenna's arms. They took advantage of the highly enhanced localized fields at the tip and demonstrated a zero-bias responsivity of 4 A/W at 28.3 THz using the same definition as Equation 4.6.1. Our measurement results suggest an average zero-bias responsivity

equal to 1.0592 A/W at 382 THz. The quantum limit imposes a maximum responsivity of approximately 17 A/W at 28.3 THz and 1.27 A/W at 382 THz. Thus, our results here suggest operation closer to the quantum limit.

Resistance as defined in Equation 4.6.2 and demonstrared in Figure 4.6.2 is important in terms of power transfer and matching to the load. The value of resistance drops significantly by application of both radiation and bias voltage. Hence, it is possible to manipulate the value of resistance by applying the appropriate bias voltage.

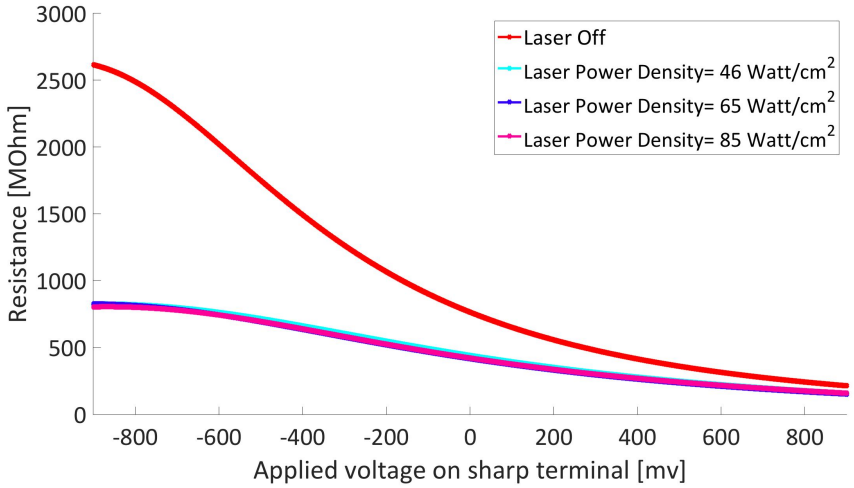

Figure 4.6.2. Diode figures of merit calculated from measured I-V characteristic using a model based on Taylor expansion of current in oscillating potential, resistance for various optical powers.

Asymmetry (Figure 4.6.3) defined as the absolute ratio of forward and reverse currents at a bias voltage indicates the rectification capability of the diode and nonlinearity (Figure 4.6.4) is a measure of deviation from a linear resistor [55]. The higher these figures of merit the more desirable the performance of diode. Donchev et al. [55] suggested asymmetry above unity and nonlinearity above 3 to be satisfactory in diode performance. The peak at approximately 0.5 v in the asymmetry curve is due

to the open circuit voltage occurring around -0.5 v in current-voltage characteristic plots.

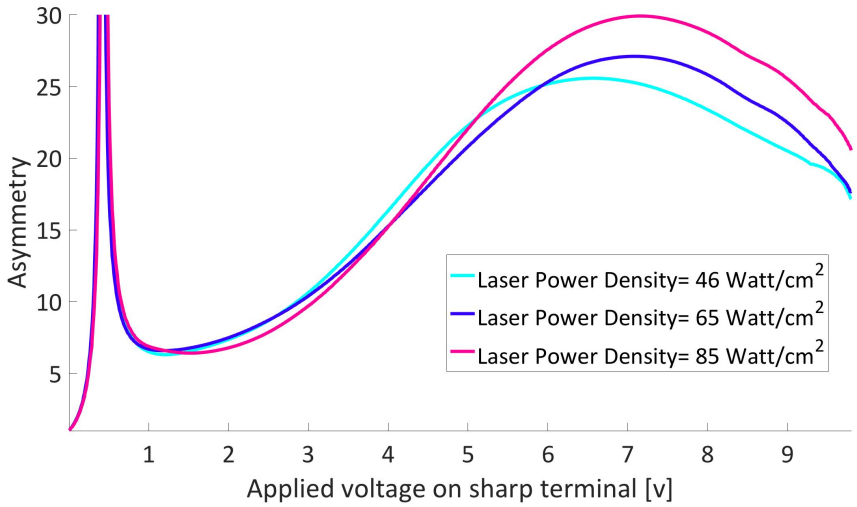

Figure 4.6.3. Diode figures of merit calculated from measured I-V characteristic using a model based on Taylor expansion of current in oscillating potential, asymmetry defined as the ratio of forward to reverse current as a function of applied voltage based on measured values.

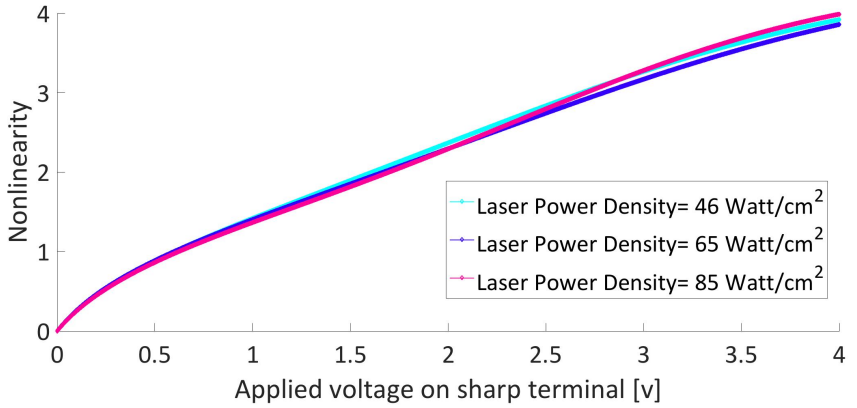

Figure 4.6.4. Diode figures of merit calculated from measured I-V characteristic using a model based on Taylor expansion of current in oscillating potential, nonlinearity, a measure of deviation from a linear resistor as a function of voltage.

Another important figure of merit of rectenna performance is power conversion efficiency defined as the ratio of output power over incident radiation power on antenna [55]. Efficiency takes four major loss mechanisms into account in conventional rectenna devices [52]. These factors are categorized as antenna efficiency, coupling efficiency between antenna and diode, rectification efficiency which is a function of responsivity, and coupling efficiency between the diode and the load. The overall power conversion efficiency is the product of these factors.

Here, we use the overall measured input and output powers rather than calculating efficiency of each step. Signal pathway length and matching challenges are minimized for each cell by integrating the antenna and diode units into one cell. Numerous theoretical studies speculated the limit of conversion efficiency of the optical rectenna device from less than 0.001 % to 2 % [55,88,89,90].

We defined the output power as half the product of the short-circuit current and the open-circuit voltage under various incident optical intensities. We derived these values from the current-voltage characteristic curves defined as the cross point of the curve with the vertical and horizontal axes, respectively. Measured power conversion efficiency is shown in Figure 4.6.5. The average zero-bias power conversion efficiency is 8.7×10^{-5}%. Although this number is small, it is expected for optical rectennas to have efficiencies in the order of 10^{-4}% to 10^{-7}% as shown by Briones et al [89]. It is also possible to increase the harvested power by scaling the area of the array.

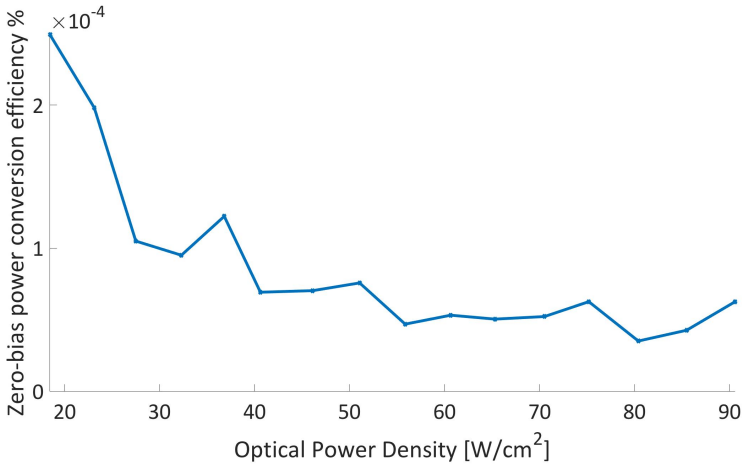

Figure 4.6.5. Power conversion efficiency in 382 THz based on measurement results.

4.7. Summary

In this chapter, we experimentally showed rectification in a geometrical metal-vacuum-metal rectenna integrating the diode and antenna together. The controllable geometric parameters of each element offer a different electric field enhancement factor for forward and reverse currents. Upon excitation with optical radiation at 382 THz, the collective oscillation of conduction band electrons of the metal provide maximized near field enhancement and facilitate electron liberation through one electrode more than the other; consequently providing rectification even at zero external bias. We discussed various figures of merit of our measured current-voltage characteristic based on Taylor expansion of the time-dependent current as a function of oscillating field. The average zero-bias responsivity at 382 THz is measured to be 1.0592 A/W based on this analysis. Due to the relatively simple fabrication process, easily accessible material, and scalability of the design, it can offer a reasonable addition for applications such as energy harvesting and optical detection. Work on

further enhancement of the power conversion efficiency and the theoretical analysis of electron emission process needs to be studied more extensively in the future.

Chapter 4, in part, has been submitted for publication of the material as it may appear in: S. Piltan, D. Sievenpiper, “Optical Rectification Using Geometrical Field Enhancement in Gold Nano-arrays”. The dissertation author was the primary author of this material.

Chapter 5

Plasmonic Nano-arrays for Infrared Photodetection

5.1. Introduction

Infrared optical spectrum plays important roles in many applications. The most common example is access to physical phenomena otherwise invisible to naked eye used in thermal imaging, environmental monitoring, medical imaging, and remote sensing [91,92,93]. The thermal infrared radiation emitted by many terrestrial objects is mainly centered in two atmospheric wavelength windows, the middle wavelength infrared (MWIR) region in 3-5 μm band, and the long wavelength infrared (LWIR) region in 8−14 μm band. This is because the maximum emissivity of gray objects at temperatures close to 300 °Kelvin is centered at wavelengths approximately around 10 μm. However, space applications rouse interest in longer wavelengths as well [94].

Infrared detectors can be classified in two main categories based on the detection mechanism [94]. The absorbed radiation can be detected in material either by interacting with electrons or by changing the temperature. Photon detectors are based on the former mechanism and thermal detectors operate due to the latter. The advantages of photon detectors compared to thermal detectors include higher signal to noise ratio and short response time; however, this requires cryogenic cooling which adds cost and weight and it is not convenient for all applications. Photon detectors based on different carrier generation methods including intrinsic and extrinsic band

gap detectors, photo-emissive detectors, and quantum well detectors have been explored and characterized.

Electrical output in thermal detectors is generated due to variations in material properties with temperature [95] and the main approaches in thermal detection are categorized based on these shifted properties. They usually consist of a temperature-dependent sensing element which is thermally isolated from surrounding structures. Thus, it is usually built in a suspended configuration. If the measured effect is due to the temperature rise induced in a material with highly temperature-dependent impedance the detector is called bolometric. Bolometers are most commonly divided into metal, thermistor, semiconductor, and super conducting types. Pyroelectric thermoelectric effects give rise to another category of thermal detectors in which the measurements are based on internal polarization variations caused by infrared radiation absorption. If the induced temperature change is measured by voltage generation against a thermal reference the thermal infrared sensor is developed based on the thermo-electric effect.

While photon detectors demonstrate wavelength-dependent response, thermal infrared detectors do not operate based on the photonic nature of incident excitation. Therefore, their response generally depends on the power level of incident radiation rather than its spectral properties. Thermal detectors are relatively cheap and convenient to use because they can operate at room temperature; however, their performance depends highly on the detector element's heat transfer characteristics and they offer lower sensitivity and their response time is longer than photon detectors.

Photon detectors based on both intrinsic and extrinsic band gap carrier generation provide superior performance as long as the temperature of device can be maintained low. Otherwise, thermally generated charge carriers undermine the signal to noise ratio. High-temperature operation of infrared detectors is therefore one of the main challenges limiting their applicability.

Among all types of photodetectors, the variable band gap HgCdTe sensors remain one of the most commonly used types [96]. HgCdTe provides high spectral tunability since changing the ratio of Hg and Cd in the composition provides energy band gaps ranging from minimum for HgTe to maximum for CdTe. As a result, this alloy is widely used in applications spanning in short, mid, long, and very long wavelength infrared bands. The most significant challenge associated with HgCdTe sensors relates to the difficulties in processing of this material. In order to achieve stable and uniform interfaces and sufficient yields strong Hg-Te bonds are required [96]. Maintaining performance of these detectors working under photoconductive, photovoltaic, and metal-insulator-semiconductor designs in high operational temperatures is another drawback to be addressed.

Nanostructures offer unique access to geometrical and optoelectronic properties not available otherwise [97]. Nano-devices such as quantum wells, carbon nanotubes, quantum dots, and graphene-based nanomaterials have been used for enhancing performance metrics of infrared photo-detectors. Plasmon-enhanced photodetectors [98] can compensate for the optical losses in metals by addressing overall challenges in flexibility, tunability, operation speed, and power consumption.

Here, we took a similar approach as previous chapters to take advantage of the size, geometry, and dielectric properties of the designed nano-array in order to target infrared photodetection applications. The main challenges being addressed by this design include spectral tunability, convenient fabrication and maintenance, and room temperature functionality.

5.2. Design and Optimization

The idea behind the design is very similar to what discussed in Chapter 3 for sharp tip periodic array of electron emitters combining the DC excitation and optical radiation at 785 nm. Engineering the geometry and configuration of metals enables manipulation of plasmon modes and their spectral properties [99,100]. Figure 5.2.1 shows the modified geometry combining electrical and optical excitations at 12 μm. As we discussed in Chapter 3, photocurrents are significantly enhanced at the surface of a gold-vacuum interface.

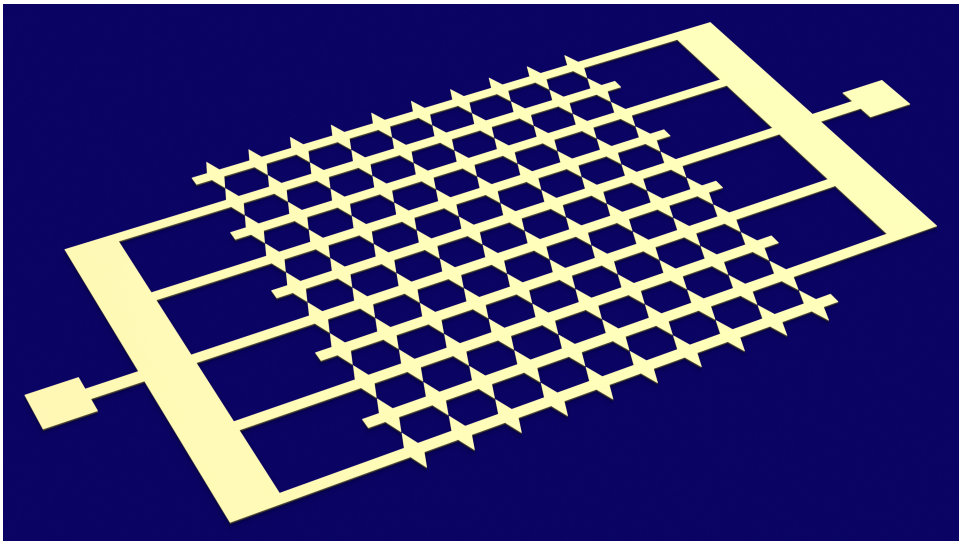

Figure 5.2.1. Resonant surface for maximized field enhancement at 25 THz.

Taking the same approach, we scaled the geometry to be resonant in wavelengths centered at 10-12 μm (long wavelength infrared) which is the band where many terrestrial objects radiate. In order to keep the fast response and maximized enhancement factor at the surface, we kept the vacuum gap width between the unit-cells on adjacent rows 50 nm. The rest of the geometrical parameters were optimized for maximizing the electric field at the tip of the triangular cell upon excitation with a plane wave at 25 THz incident vertically and polarized in direction of the tip axis. We used Johnson and Christy [39] complex permittivity model for gold and similar boundary conditions in simulations using Ansoft HFSS as described in Chapter 3. The substrate in simulations was a 280 nm thick layer of silicon dioxide on silicon. The final dimensions based on the simulations are shown in Figure 5.2.2.

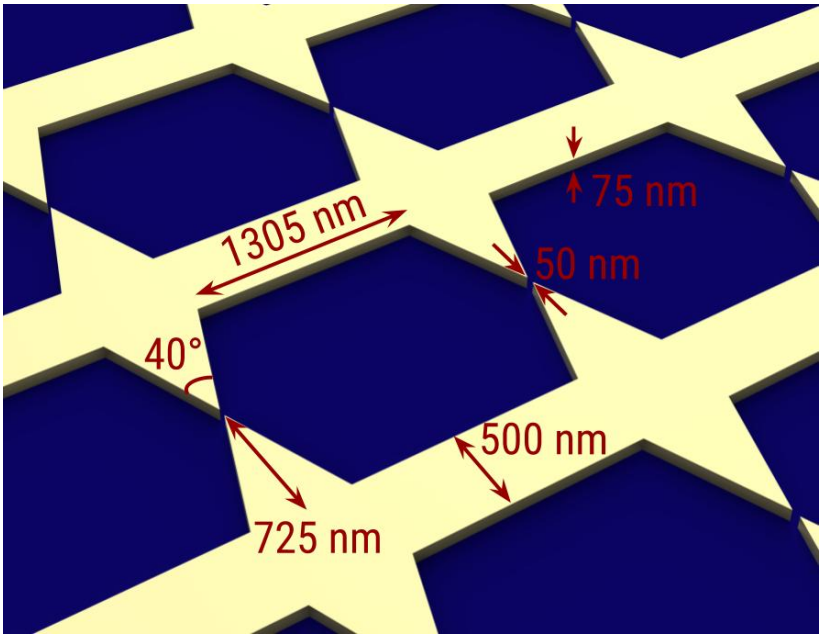

Figure 5.2.2. Simulated optimized dimensions for maximized field enhancement at 25 THz.

Figure 5.2.3 shows the field enhancement factor at two points for the optimized geometry, one point is on the surface of the triangular tip and the other is in the mid-point between the unit-cells in the vacuum gap. Both points are 37.5 nm above the silicon dioxide substrate. Field profile in the vacuum gap at 13 μm is demonstrated in Figure 5.2.4.

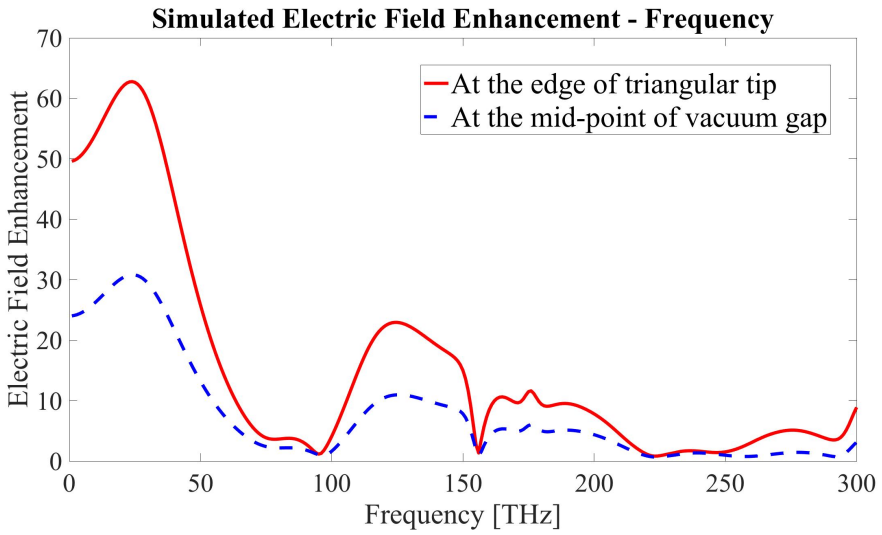

Figure 5.2.3. Simulated field enhancement as a function of frequency for final optimized dimensions, solid (red) at the edge of the triangular tip, dashed (blue) in the middle of the gap, both vertically 37.5 nm above substrate.

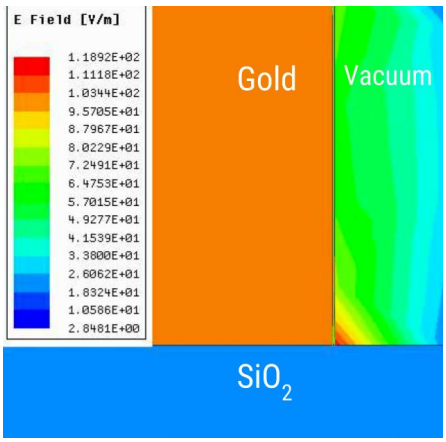

Figure 5.2.4. Side view of field profile in the air gap between the electrodes at 23 THz.

5.3. Fabrication

Fabrication was done following similar steps as Chapter 3 on silicon wafers with resistivity above 10000 Ω cm with a 280 nm thick layer of thermally oxide SiO_2. The 40x40 array layout was exposed using electron beam lithography. A 5 nm thick chromium adhesion layer and 70 nm thick layer of gold were electron beam evaporated following the exposure. After finishing the lift-off using Remover PG overnight and a subsequent session in acetone in an ultrasonic bath, the fabricated samples were imaged using scanning electron microscope. Figure 5.3.1 shows samples after fabrication.

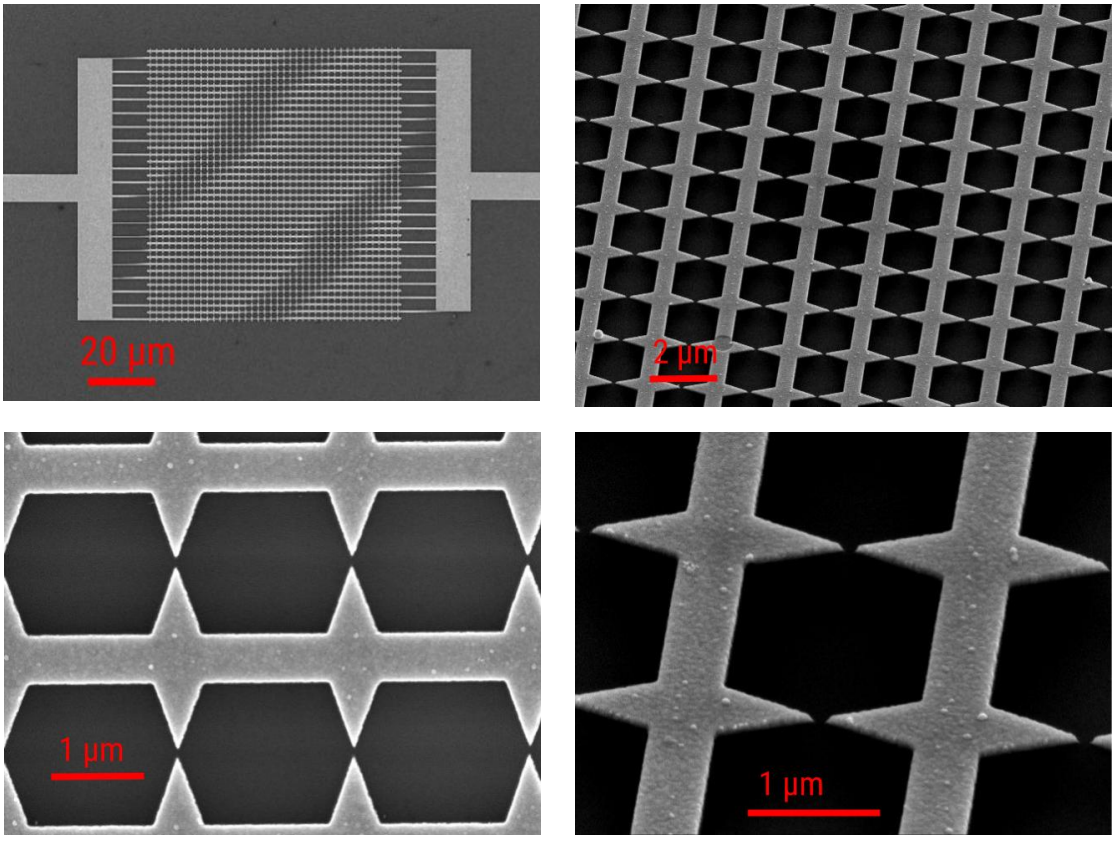

Figure 5.3.1. Scanning electron microscope images of fabricated resonant array.

5.4. Characterization and Measurement

Fabricated samples were wire bonded in dual in-line packages and connected to Keithley 2410 source-meter for current-voltage characterization. For infrared excitation, we used emission from a silicon nitride furnace igniter at 1300 °C. Radiation was focused on the sample using a ZnSe meniscus lens with focal length of 63.5 mm and diameter of 28 mm.

Figure 5.4.1 demonstrates the measured current-voltage curves for when the igniter is off and on. Infrared radiation from the igniter results in photocurrents 3-4 times higher than the dark current and the effect is amplified for larger bias voltages.

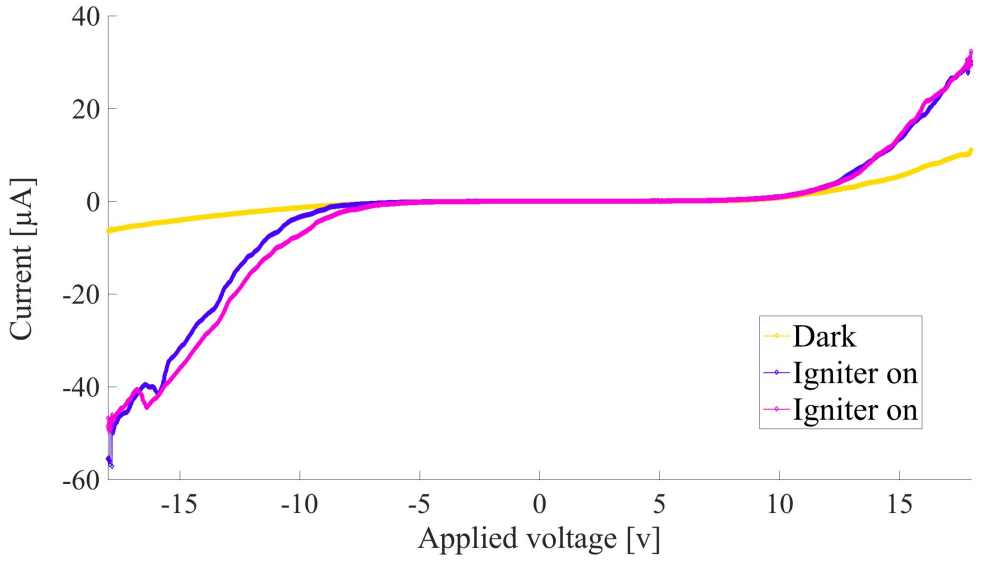

Figure 5.4.1. Measured current-voltage characteristic of array for infrared detection.

5.5. Modeling and Discussion

In order to interpret the measured results we should first understand the power density levels emitted by the thermal igniter. We assumed emissivity of unity for our thermal radiator in our calculations. This assumption was due to the fact that at a given temperature spectral radiance emitted by a non-unity emissivity source is lower than an ideal black body. Therefore, calculations done based on unity emissivity result in upper bound on emitted radiance and lower bound on figures of merit such as specific detectivity and sensitivity.

Spectral density of electromagnetic radiation emitted by a black body in thermal equilibrium at a given temperature is given by Planck's law. Spectral radiance of a body is defined as the energy emitted from it associated with different frequencies. In other words, it describes the power emitted per unit area of the body, per unit solid angle of measurement, per unit frequency.

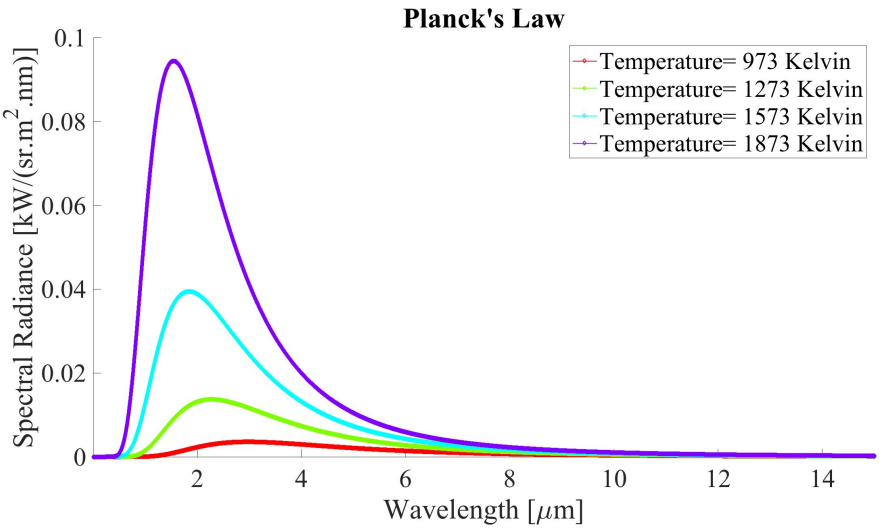

Figure 5.5.1. Spectral radiance as a function of wavelength for a variety of temperatures.

Planck's law describes the spectral radiance as:

$$\beta_\nu(\nu, T) = \frac{2h\nu^3}{c^2}\frac{1}{e^{h\nu/K_B T}-1}\ [W.sr^{-1}.m^{-2}.Hz^{-1}] \qquad \textbf{Equation 5.5.1}$$

Where ν is frequency, h is Planck's constant, c is the speed of light, K_B is the Boltzmann constant, and T is the temperature. Thermal radiation from a black body is equal to the full amount specified by Planck's law. Figure 5.5.1 shows spectral radiance as a function of wavelength for different temperatures.

Emittance of the body is defined as the total energy radiated per unit surface of the black body radiator across all wavelengths per unit time and it is given by the Stefan-Boltzmann law. In order to derive the total energy emitted per unit area we should integrate the power radiated by a surface area A through solid angle dΩ in the frequency range between ν and ν + dν given by:

$$\beta_\nu(\nu, T)A d\nu d\Omega = \frac{2h\nu^3}{c^2}\frac{1}{e^{h\nu/K_B T}-1}A d\nu d\Omega \qquad \textbf{Equation 5.5.2}$$

Therefore power density integrated over a half sphere of solid angle can be written as:

$$\frac{P}{A} = \int \beta_\nu(\nu, T)\, d\nu \int d\Omega$$

$$= \int \frac{2h\nu^3}{c^2}\frac{1}{e^{h\nu/K_B T}-1} d\nu \int d\varphi \int \sin\theta d\theta$$

$$= \frac{2\pi h}{c^2}\left(\frac{K_B T}{h}\right)^4 \int \frac{u^3}{e^u - 1} du$$

$$= \sigma T^4\ [\frac{W}{m^2}]$$

Equation 5.5.3

Where σ is the Stefan-Boltzmann constant given by:

$$\sigma = \frac{2\pi^5 K_B^4}{15c^2h^3} \qquad \textbf{Equation 5.5.4}$$

Radiance or the power per unit area of black body per unit solid angle of radiance is therefore given by:

$$L = \frac{\sigma}{\pi} T^4 \left[\frac{W}{m^2 sr}\right] \qquad \textbf{Equation 5.5.5}$$

Solid angle in our measurement is given by:

$$\Omega = \frac{\pi d^2}{4l^2} \ [sr] \qquad \textbf{Equation 5.5.6}$$

Where d is the lens diameter equal to 63.5 mm and l is the distance. Total power density incident on our sample in our measurements is equal to 1.687 $\frac{W}{cm^2}$.

The two most widely used characteristic factors for comparison of performance of detector technologies are responsivity and specific detectivity. Responsivity is a measure of the current the system can output upon excitation with a given optical power. It can be written as:

$$\beta = \frac{I_{generated}}{P_{optical}} \left[\frac{A}{W}\right] \qquad \textbf{Equation 5.5.7}$$

Specific detectivity is the main figure of merit for characterizing normalized signal to noise performance of detection. It is equal to the reciprocal of noise equivalent power normalized per square root of the sensor's area and frequency bandwidth. Specific detectivity is commonly expressed in units of $\frac{cm\sqrt{Hz}}{W}$ or Jones and it is defined as:

$$D^* = \frac{\sqrt{A\Delta f}}{NEP}\ [\frac{cm\sqrt{Hz}}{W}]$$ **Equation 5.5.8**

Where A is the detector area, Δf is the measurement bandwidth, and NEP is the noise equivalent power.

Noise equivalent power is defined as the power level of the input signal that would result in a signal to noise ratio of unity in a bandwidth of 1 hertz. In other words, it is the optical power needed to induce a current equivalent to the noise current. Noise equivalent power can be written as a function of noise current and responsivity in form of:

$$NEP = \frac{I_n}{\beta}\ [W]$$ **Equation 5.5.8**

We assumed calculations at room temperature. Noise current I_n in our device is the sum of shot noise from the photocurrent and the Johnson noise from detector resistance [52,101] and it can be expressed as:

$$I_n = \sqrt{(2qI_{ph} + \frac{4K_BT}{R})\Delta f}$$ **Equation 5.5.9**

Here, we assumed absorption efficiency of 100%. We used the calculations explained above to extract the responsivity, noise current, and specific detectivity of the detector based on measured current-voltage properties.

Figure 5.5.2 and 5.5.3 demonstrate the extracted values of responsivity and specific detectivity as a function of applied voltage, respectively.

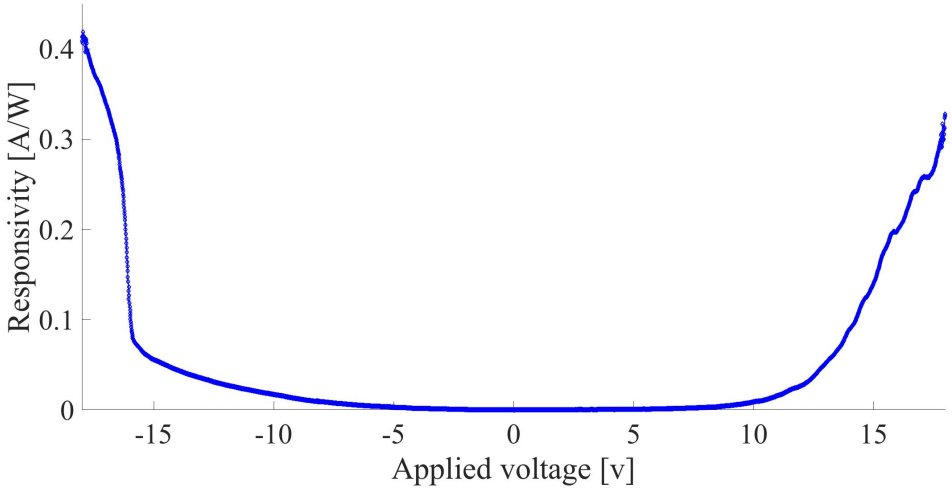

Figure 5.5.2. Responsivity as a function of applied voltage based on current-voltage characteristic curves.

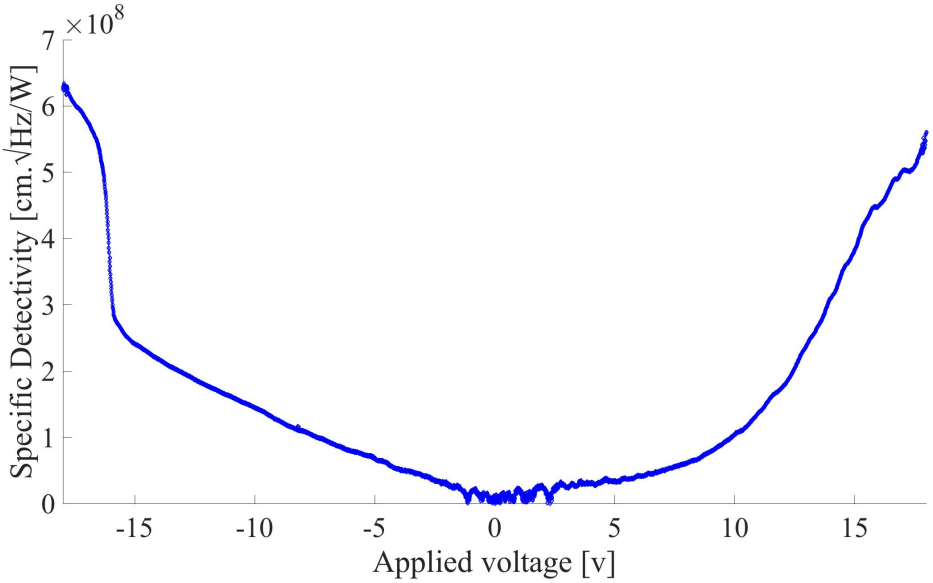

Figure 5.5.3. Specific detectivity as a function of applied voltage based on current-voltage characteristic curves.

Since emission mechanism is facilitated by applying higher DC voltages, photocurrent, responsivity, and specific detectivity also increase with voltage. The

efficiency defined as the ratio of the output power to the input optical power is shown in Figure 5.5.4.

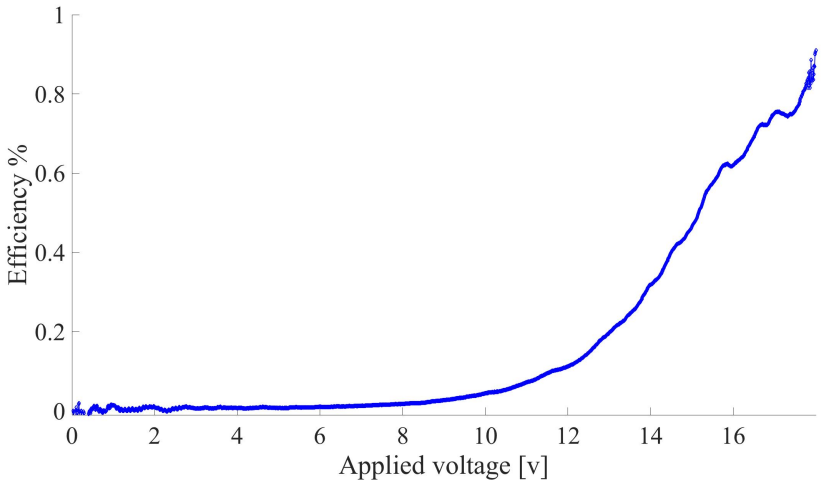

Figure 5.5.4. Efficiency as a function of applied voltage based on current-voltage characteristic curves.

Avoiding semiconductors as the medium of charge transport helps to reduce the noise due to generation and recombination processes and enhance sensitivity. Since spectral response of the design depends highly on the geometry, it is possible to tailor it for optimized detection at different parts of the infrared spectrum. This allows fabrication of dual and multi-color devices. The performance of the resonant surface is not strongly contingent on cryogenic cooling and low temperatures. Although lower temperatures still provide superior sensitivity, the contribution of noise caused by thermal effects is not the dominant mechanism in signal to noise ratio. Specific detectivity associated with various available detectors operated in different temperatures is reviewed by Rogalski [94,95,101] and room temperature performance of detectors including InSb, PbSe, and InAs sensors operating in photovoltaic, photoconductive, and photoelectromagnetic modes and bolometers is shown to be on

the order of 10^8-10^9 $\frac{\mathrm{cm}\sqrt{\mathrm{Hz}}}{\mathrm{W}}$. InGaAs and HgCdTe detectors can have larger detectivities but as discussed before the complications in processing these materials for high yield purposes can make the proposed nano-array an attractive alternative solution for infrared photodetection.

5.6. Summary

In this chapter, we proposed a solution for multi-band, flexible, and room temperature detection of infrared radiation based on an easy-to-fabricate gold nano-array. The plasmon-enhanced detection occurs due to the nonlinear interaction of incoming infrared radiation and gold surface at the resonance frequency of the array. The proposed structure takes advantage of metal as the active detection medium and therefore provides high detectivity (on the order of 10^8 $\frac{\mathrm{cm}\sqrt{\mathrm{Hz}}}{\mathrm{W}}$ which can be improved with DC bias voltage) and potentially faster response, removing requirements for cooling and difficult material processing.

Chapter 5, in part, is currently being prepared for submission for publication of the material as it may appear in: S. Piltan, D. Sievenpiper, “Plasmonic Nano-arrays for Enhanced Photoemission and Photodetection”. The dissertation author was the primary author of this material.

Chapter 6

Summary and Conclusion

It has been demonstrated that coupling of electromagnetic radiation to free electron oscillations at a metal interface has interesting properties that can be used in a variety of applications including photovoltaic devices, optical antennas, optical rectification, and infrared photodetection. The most important property of this light-matter interaction allowing for compensation of metal losses in optical frequencies is the enhanced electric field at the surface at the resonance frequency which is also tightly confined at the interface.

Chapter 1 first discussed the advantages of using vacuum as the medium for charge transport and explained the main challenges in liberating electrons from metals. Electron emission mechanisms are classified into four main categories and the transition between them due to a combination of electrical and photonic excitations is explained. Finally, the role of plasmonic field enhancement in both electron emission and acceleration processes is discussed.

Chapter 2 presents the idea behind the design of the periodic array as a means for combination of static electric fields applied through a bias voltage and optical fields incident upon a vacuum-channel surface. The design process of the geometry and the simulations in order to optimize the dimensions are discussed. Then fabrication and measurement steps are explained. Finally, the measured characteristics

are modeled using the time-dependent Schrödinger equation for a rounded triangular barrier. Using this model the electric field enhancement at the surface is extracted such that the measurement and analytical solution curves match for different DC and optical powers.

Chapter 3 introduces a variation of the periodic surface based on the same phenomena modified for maximized field enhancement at the tip of a triangular unit-cell. After explaining the design, fabrication, and measurement processes the scaling property of the photocurrent with the area of device is experimentally demonstrated. In this chapter slope of Fowler-Nordheim curves is used in order to extract the electric field enhancement at the tip of metal cell and the measured results on modeled on that basis.

Chapter 4 presents an optical rectifier operating based on geometrical asymmetry at the surface. The electric fields centered at wavelength equal to 785 nm are rectified using a surface allowing flow of electrons only in one direction due to asymmetrical field enhancement factors at the interface of two electrodes. The proposed device is compared with available diode technologies and the main limits on rectification speed are explained. Experimental asymmetric current-voltage characteristics of the device are followed. Finally, the surface is characterized for main diode figures of merit including responsivity, nonlinearity, asymmetry, and efficiency using the Taylor expansion of the time-dependent current as a function of oscillating field.

In chapter 5, the geometrical degree of freedom of the surface is exploited in order to enable photodetection in infrared frequencies without requirements for low temperatures and using simple fabrication techniques. Using a similar idea as previous chapters this time the device is optimized for maximum field enhancement in infrared part of frequency spectrum. The current-voltage characteristics based on measurements using a furnace igniter at 1300 °C are analyzed for responsivity and specific detectivity of the surface.

This work presented a variety of applications including optical rectification and photodetection allowing multi-band operation at room temperature. Similar ideas can be exploited for development of efficient optical gate transistors for high-speed and high-power applications. The proposed vacuum-channel device allows for operation above damage threshold of solid-state devices using easily accessible material and enables scalable designs. In the future, there is need for more in-depth theoretical analysis of the physical phenomena associated with this interesting nonlinear behavior. Depending on the specific application being targeted, the power conversion efficiency, the sensitivity, and the power handling of the device are among parameters that could be improved further.

Bibliography

[1] M. Fleischmann, P. J. Hendra, and A. J. McQuillan, "Raman spectra of pyridine adsorbed at a silver electrode," *Chemical Physics Letters*, vol. 26, no. 2, pp. 163-166, 1974.

[2] P. L. Stiles, J. A. Dieringer, N. C. Shah, and R. P. Van Duyne, "Surface-enhanced Raman spectroscopy," *Annual Review of Analytical Chemistry*, vol. 1, pp. 601-626, 2008.

[3] E. Laux, C. Genet, T. Skauli, and T. W. Ebbesen, "Plasmonic photon sorters for spectral and polarimetric imaging," *Nature Photonics*, vol. 2, no. 3, pp. 161-164, 2008.

[4] M. E. Stewart, N. H. Mack, V. Malyarchuk, J. A. Soares, T. W. Lee, S. K. Gray, R. G. Nuzzo, and J. A. Rogers, "Quantitative multispectral biosensing and 1D imaging using quasi-3D plasmonic crystals," *Proceedings of the National Academy of Sciences*, vol. 103, no. 46, pp. 17143-17148, 2006.

[5] T. Xu, Y. K. Wu, X. Luo, and L. J. Guo, "Plasmonic nanoresonators for high-resolution colour filtering and spectral imaging," *Nature communications*, vol. 1, no. 5, p. 59, 2010.

[6] H. A. Atwater and A. Polman, "Plasmonics for improved photovoltaic devices," *Nature materials*, vol. 9, no. 3, pp. 205-213, 2010.

[7] S. Mukherjee, F. Libisch, N. Large, O. Neumann, L. V. Brown, J. Cheng, J. B. Lassiter, E. A. Carter, P. Nordlander, and N. J. Halas, "Hot electrons do the impossible: plasmon-induced dissociation of H2 on Au," *Nano Letters*, vol. 13, no. 1, pp. 240-247, 2013.

[8] P. Christopher, H. Xin, and S. Linic, "Visible-light-enhanced catalytic oxidation reactions on plasmonic silver nanostructures," *Nature chemistry*, vol. 3, no. 6, pp. 467-472, 2011.

[9] I. Goykhman, B., Desiatov, J. Khurgin, J. Shappir, and U. Levy, "Waveguide based compact silicon Schottky photodetector with enhanced responsivity in the telecom spectral band," *Optics express*, vol. 20, no. 27, pp. 28594-28602, 2012.

[10] P. Mühlschlegel, H. J. Eisler, O. J. F. Martin, B. Hecht, and D. W. Pohl, "Resonant optical antennas," *science*, vol. 308, no. 5728, pp. 1607-1609, 2005.

[11] M. W. Knight, H. Sobhani, P. Nordlander, and N. J. Halas, "Photodetection with active optical antennas," *Science*, vol. 332, no. 6030, pp. 702-704, 2011.

[12] W. L. Barnes, A. Dereux, and T. W. Ebbesen, "Surface plasmon subwavelength optics," *Nature*, vol. 424, no. 6950, pp. 824-830, 2003.

[13] H. Ditlbacher, J. R. Krenn, G. Schider, A. Leitner, and F. R. Aussenegg, "Two-dimensional optics with surface plasmon polaritons," *Applied Physics Letters*, vol. 81, no. 10, pp. 1762-1764, 2002.

[14] R. A. Shelby, D. R. Smith, and S. Schultz, "Experimental verification of a negative index of refraction," *Science*, vol. 292, no. 5514, pp. 77-79, 2001.

[15] N. Fang, H. Lee, C. Sun, and X. Zhang, "Sub–diffraction-limited optical imaging with a silver superlens," *Science*, vol. 308, no. 5721, pp. 534-537, 2005.

[16] E. Braun and S. MacDonald, *Revolution in miniature: The history and impact of semiconductor electronics*.: Cambridge University Press., 1982.

[17] F Guthrie, *Magnetism and electricity*.: W. Collins, Sons, 1876.

[18] H. F. Dylla and S. T. Corneliussen, "John Ambrose Fleming and the beginning of electronics," *Journal of Vacuum Science & Technology A: Vacuum, Surfaces, and Films*, vol. 23, no. 4, pp. 1244-1251, 2005.

[19] W. F. Brinkman, D. E. Haggan, and W. W. Troutman, "A history of the invention of the transistor and where it will lead us," *IEEE Journal of Solid-State Circuits*, vol. 32, no. 12, pp. 1858-1865, 1997.

[20] J. W. Han, J. Sub Oh, and M. Meyyappan, "Vacuum nanoelectronics: Back to the future?—Gate insulated nanoscale vacuum channel transistor," *Applied physics letters*, vol. 100, no. 21, p. 213505, 2012.

[21] M. Reiser, *Theory and design of charged particle beams*.: John Wiley & Sons, 2008.

[22] R. H. Fowler and L. Nordheim, "Electron emission in intense electric fields," *Proceedings of the Royal Society of London A: Mathematical, Physical and*

Engineering Sciences, vol. 119, no. 781, pp. 173-181, 1928.

[23] P. Hommelhoff, Y. Sortais, A. Aghajani-Talesh, and M. A. Kasevich, "Field emission tip as a nanometer source of free electron femtosecond pulses," *Physical review letters*, vol. 96, no. 7, p. 077401, 2006.

[24] C. Kealhofer, S. M. Foreman, S. Gerlich, and M. A. Kasevich, "Ultrafast laser-triggered emission from hafnium carbide tips.," *Physical Review B*, vol. 86, no. 3, p. 035405, 2012.

[25] H. Yanagisawa, M. Hengsberger, D. Leuenberger, M. Klöckner, C. Hafner, T. Greber, and J. Osterwalder, "Energy distribution curves of ultrafast laser-induced field emission and their implications for electron dynamics," *Physical review letters*, vol. 107, no. 8, p. 087601, 2011.

[26] M. R. Bionta, B. Chalopin, J. P. Champeaux, S. Faure, A. Masseboeuf, P. Moretto-Capelle, and B. Chatel, "Laser-induced electron emission from a tungsten nanotip: identifying above threshold photoemission using energy-resolved laser power dependencies," *Journal of Modern Optics*, vol. 61, no. 10, pp. 833-838, 2014.

[27] C. Ropers, D. R. Solli, C. P. Schulz, C. Lienau, and T. Elsaesser, "Localized multiphoton emission of femtosecond electron pulses from metal nanotips," *Physical review letters*, vol. 98, no. 4, p. 043907, 2007.

[28] L. V. Keldysh, "Ionization in the field of a strong electromagnetic wave," *Sov. Phys. JETP*, vol. 20, no. 5, pp. 1307-1314, 1965.

[29] S. V. Yalunin, M. Gulde, and C. Ropers, "Strong-field photoemission from surfaces: Theoretical approaches," *Physical Review B*, vol. 84, no. 19, p. 195426, 2011.

[30] S. M. Teichmann, P. Rácz, M. F. Ciappina, J. A. Pérez-Hernández, A. Thai, J. Fekete, A. Y. Elezzabi, L. Veisz, J. Biegert, and P. Dombi, "Strong-field plasmonic photoemission in the mid-IR at< 1 GW/cm 2 intensity," *Scientific reports*, vol. 5, p. srep07584, 2015.

[31] M., Pant and L. K. Ang, "Ultrafast laser-induced electron emission from multiphoton to optical tunneling," *Physical Review B*, vol. 86, no. 4, p. 045423, 2012.

[32] F. Schertz, M. Schmelzeisen, M. Kreiter, H. J. Elmers, and G. Schönhense,

"Field emission of electrons generated by the near field of strongly coupled plasmons," *Physical review letters*, vol. 108, no. 23, p. 237602, 2012.

[33] P. Dombi, A. Hörl, P. Rácz, I. Márton, A. Trügler, J. R. Krenn, and U. Hohenester, "Ultrafast strong-field photoemission from plasmonic nanoparticles," *Nano letters*, vol. 13, no. 2, pp. 674-678, 2013.

[34] K. Iwami, A. Iizuka, and N. Umeda, "Laser stimulated electron field emission at the plasmon-resonant wavelength," in *Nano/Micro Engineered and Molecular Systems (NEMS), 2011 IEEE International Conference on*, February 2011, pp. 1085-1088.

[35] S. Kim, J. Jin, Y. J. Kim, I. Y. Park, Y. Kim, and S. W. Kim, "High-harmonic generation by resonant plasmon field enhancement," *Nature*, vol. 453, no. 7196, pp. 757-760, 2008.

[36] P. Biagioni, J. S. Huang, and B. Hecht, "Nanoantennas for visible and infrared radiation," *Reports on Progress in Physics*, vol. 75, no. 2, p. 024402, 2012.

[37] J. M. Pitarke, V. M. Silkin, E. V. Chulkov, and P. M. Echenique, "Theory of surface plasmons and surface-plasmon polaritons," *Reports on progress in physics*, vol. 70, no. 1, p. 1, 2006.

[38] K. A. Willets and R. P. Van Duyne, "Localized surface plasmon resonance spectroscopy and sensing," *Annual Review of Physical Chemistry*, vol. 58, pp. 267-297, 2007.

[39] P. B. Johnson and R. W. Christy, "Optical constants of the noble metals," *Physical review B*, vol. 6, no. 12, p. 4370, 1972.

[40] E. Forati, T. J. Dill, A. R. Tao, and D. Sievenpiper, "hotoemission-based microelectronic devices," *Nature communications*, vol. 7, p. 13399, 2016.

[41] D. R. Ward, F. Hüser, F. Pauly, J. C. Cuevas, and D. Natelson, "Optical rectification and field enhancement in a plasmonic nanogap," *Nature nanotechnology*, vol. 5, no. 10, pp. 732-736, 2010.

[42] M. J. Lee, "Field emission of hot electrons from tungsten," *Physical Review Letters*, vol. 30, no. 24, p. 1193, 1973.

[43] M. Schenk, M. Krüger, and P. Hommelhoff, "Strong-field above-threshold photoemission from sharp metal tips," *Physical review letters*, vol. 105, no. 25,

p. 257601, 2010.

[44] H. R. Reiss, "Effect of an intense electromagnetic field on a weakly bound system," *Physical Review A*, vol. 22, no. 5, p. 1786, 1980.

[45] N. I. Shvetsov-Shilovski, M. Lein, L. B. Madsen, E. Räsänen, C. Lemell, J. Burgdörfer, D. G. Arbó, and K. Tőkési, "Semiclassical two-step model for strong-field ionization," *Physical Review A*, vol. 94, no. 1, p. 013415, 2016.

[46] P. Zhang and Y. Y. Lau, "Ultrafast strong-field photoelectron emission from biased metal surfaces: exact solution to time-dependent Schrödinger Equation," *Scientific reports*, vol. 6, 2016.

[47] M. Aeschlimann, C. A. Schmuttenmaer, H. E. Elsayed‐Ali, R. J. D. Miller, J. Cao, Y. Gao, and D. A. Mantell, "Observation of surface enhanced multiphoton photoemission from metal surfaces in the short pulse limit," *The Journal of chemical physics*, vol. 102, no. 21, pp. 8606-8613, 1995.

[48] N. M. Miskovsky, P. H. Cutler, A. Mayer, B. L. Weiss, B. Willis, T. E. Sullivan, and P. B. Lerner, "Nanoscale devices for rectification of high frequency radiation from the infrared through the visible: a new approach," *Journal of Nanotechnology*, vol. 2012, pp. 1-19, 2012.

[49] P. Bharadwaj, B. Deutsch, and L. Novotny, "Optical antennas," *Advances in Optics and Photonics*, vol. 1, no. 3, pp. 438-483, 2009.

[50] L. Novotny and N. Van Hulst, "Antennas for light," *Nature photonics*, vol. 5, no. 2, pp. 83-90, 2011.

[51] J. Alda, J. M. Rico-García, J. M. López-Alonso, and G. Boreman, "Optical antennas for nano-photonic applications," *Nanotechnology*, vol. 16, no. 5, p. S230, 2005.

[52] G. Moddel and S. Grover, *Rectenna solar cells*. New York: Springer, 2013, vol. 4.

[53] W. Shockley and H. J. Queisser, "Detailed balance limit of efficiency of p-n junction solar cells," *Journal of applied physics*, vol. 32, no. 3, pp. 510-519, 1961.

[54] C. H. Henry, "Limiting efficiencies of ideal single and multiple energy gap

terrestrial solar cells," *Journal of applied physics*, vol. 51, no. 8, pp. 4494-4500, 1980.

[55] E. Donchev, J. S. Pang, P. M. Gammon, A. Centeno, F. Xie, P. K. Petrov, J. D. Breeze, M. P. Ryan, D. J. Riley, and N. M. Alford, "The rectenna device: From theory to practice (a review)," *MRS Energy & Sustainability-A Review Journal*, vol. 1, pp. 1-34, 2014.

[56] R. D. Grober, R. J. Schoelkopf, and D. E. Prober, "Optical antenna: Towards a unity efficiency near-field optical probe," *Applied Physics Letters*, vol. 70, no. 11, pp. 1354-1356, 1997.

[57] G. S. Kino, A. Sundaramurthy, P. J. Schuck, D. P. Fromm, and W. E. Moerner, *Surface Plasmon Nanophotonics*.: Springer, 2007.

[58] P. J. Burke, S. Li, and Z. Yu, "Quantitative theory of nanowire and nanotube antenna performance," *IEEE transactions on nanotechnology*, vol. 5, no. 4, pp. 314-334, 2006.

[59] L. Novotny, "Effective wavelength scaling for optical antennas," *Physical Review Letters*, vol. 98, no. 26, p. 266802, 2007.

[60] K. Kempa, J. Rybczynski, Z. Huang, K. Gregorczyk, A. Vidan, B. Kimball, J. Carlson, G. Benham, Y. Wang, A. Herczynski, and Z. F. Ren, "Carbon nanotubes as optical antennae," *Advanced Materials*, vol. 19, no. 3, pp. 421-426, 2007.

[61] A. S. Sedra and K. C. Smith, *Microelectronic circuits*. New York: Oxford University Press, 1998, vol. 1.

[62] H. Kazemi, K. Shinohara, G. Nagy, W. Ha, B. A. Lail, E. N. Grossman, G. Zummo, W. R. Folks, J. Alda, and G. D. Boreman, "First THz and IR characterization of nanometer-scaled antenna-coupled InGaAs/InP Schottky-diode detectors for room temperature infrared imaging," in *Proceedings of SPIE*, vol. 6542, 2007, pp. 65421J-2.

[63] E. R. Brown, "A system-level analysis of Schottky diodes for incoherent THz imaging arrays," *Solid-State Electronics*, vol. 48, no. 10, pp. 2051-2053, 2004.

[64] T. E. Sullivan, Y. Kuk, and P. H. Cutler, "Proposed planar scanning tunneling microscope diode: application as an infrared and optical detector," *IEEE Transactions on Electron Devices*, vol. 36, no. 11, pp. 2659-2664, 1989.

[65] B. Berland, "Photovoltaic Technologies Beyond the Horizon: Optical Rectenna Solar Cell," *National Renewable Energy Laboratory*, vol. NREL/SR-520-33263, 2003.

[66] M. Tonouchi, "Cutting-edge terahertz technology," *Nature photonics*, vol. 1, no. 2, pp. 97-105, 2007.

[67] H. Q. Nguyen, P. H. Cutler, T. E. Feuchtwang, Z-H. Huang, Y. Kuk, P. J. Silverman, A. A. Lucas, and T. E. Sullivan, "Mechanisms of current rectification in an STM tunnel junction and the measurement of an operational tunneling time," *IEEE Transactions on Electron devices*, vol. 36, no. 11, pp. 2671-2678, 1989.

[68] P. H. Cutler, T. E. Feuchtwang, Z. Huang, T. T. Tsong, H. Nguyen, A. A. Lucas, and T. E. Sullivan, "EXPERIMENTAL AND THEORETICAL RESULTS OF RECTIFICATION MEASUREMENTS IN AN STM," *Le Journal de Physique Colloques*, vol. 48, no. C6, pp. C6-97, 1987.

[69] P. K. Tien and J. P. Gordon, "Multiphoton process observed in the interaction of microwave fields with the tunneling between superconductor films," *Physical Review*, vol. 129, no. 2, p. 647, 1963.

[70] J. R. Tucker and M. J. Feldman, "Quantum detection at millimeter wavelengths," *Reviews of Modern Physics*, vol. 57, no. 4, p. 1055, 1985.

[71] A. Sanchez, C. F. Davis Jr, K. C. Liu, and A. Javan, "The MOM tunneling diode: Theoretical estimate of its performance at microwave and infrared frequencies," *Journal of Applied Physics*, vol. 49, no. 10, pp. 5270-5277, 1978.

[72] S. Grover and G. Moddel, "Applicability of metal/insulator/metal (MIM) diodes to solar rectennas," *IEEE Journal of Photovoltaics*, vol. 1, no. 1, pp. 78-83, 2011.

[73] N. M. Miskovsky, S. J. Shepherd, P. H. Cutler, T. E. Sullivan, and A. A. Lucas, "The importance of geometry, field, and temperature in tunneling and rectification behavior of point contact junctions of identical metals," *Applied Physics Letters*, vol. 35, no. 7, pp. 560-562, 1979.

[74] P. C. Hobbs, R. B. Laibowitz, F. R. Libsch, N. C. LaBianca, and P. P. Chiniwalla, "Efficient waveguide-integrated tunnel junction detectors at 1.6 μm," *Optics express*, vol. 15, no. 25, pp. 16376-16389, 2007.

[75] S. Grover, O. Dmitriyeva, M. J. Estes, and G. Moddel, "Traveling-wave metal/insulator/metal diodes for improved infrared bandwidth and efficiency of antenna-coupled rectifiers," *IEEE Transactions on Nanotechnology*, vol. 9, no. 6, pp. 716-722, 2010.

[76] G. Moddel, "Geometric diode, applications and method," U.S. Patent No. 8,803,340, Aug. 12, 2014.

[77] A. Mayer, M. S. Chung, P. B. Lerner, B. L. Weiss, N. M. Miskovsky, and P. H. Cutler, "Classical and quantum responsivities of geometrically asymmetric metal-vacuum-metal junctions used for the rectification of infrared and optical radiations," *Journal of Vacuum Science & Technology B, Nanotechnology and Microelectronics: Materials, Processing, Measurement, and Phenomena*, vol. 29, no. 4, p. 041802, 2011.

[78] M. Dagenais, K. Choi, F. Yesilkoy, A. N. Chryssis, and M. C. Peckerar, "Solar spectrum rectification using nano-antennas and tunneling diodes," in *Proceedings of SPIE*, vol. 7605, 2010, pp. 76050E-1.

[79] Z. Zhu, S. Joshi, S. Grover, and G. Moddel, "Graphene geometric diodes for terahertz rectennas," *Journal of Physics D: Applied Physics*, vol. 46, no. 18, p. 185101, 2013.

[80] A. C. Neto, F. Guinea, N. M. Peres, K. S. Novoselov, and A. K. Geim, "The electronic properties of graphene," *Reviews of modern physics*, vol. 81, no. 1, p. 109, 2009.

[81] M. M. Gauthier, *Engineered materials handbook*.: ASM International, 1995.

[82] A. V. Bragas, S. M. Landi, and O. E. Martınez, "Laser field enhancement at the scanning tunneling microscope junction measured by optical rectification," *Applied physics letters*, vol. 72, no. 17, pp. 2075-2077, 1998.

[83] A. Mayer, M. S. Chung, B. L. Weiss, N. M. Miskovsky, and P. H. Cutler, "Three-dimensional analysis of the geometrical rectifying properties of asymmetric metal-vacuum-metal junctions and extension for energy conversion," *Physical Review B*, vol. 77, no. 8, p. 085411, 2008.

[84] A. Mayer, M. S. Chung, B. L. Weiss, N. M. Miskovsky, and P. H. Cutler, "Three-dimensional analysis of the rectifying properties of geometrically asymmetric metal-vacuum-metal junctions treated as an oscillating barrier," *Physical Review B*, vol. 78, no. 20, p. 205404, 2008.

[85] A. Mayer and P. H. Cutler, "Rectification properties of geometrically asymmetric metal–vacuum–metal junctions: a comparison of tungsten and silver tips to determine the effects of polarization resonances," *Journal of Physics: Condensed Matter*, vol. 21, no. 39, p. 395304, 2009.

[86] A. Mayer, M. S. Chung, B. L. Weiss, N. M. Miskovsky, and P. H. Cutler, "Simulations of infrared and optical rectification by geometrically asymmetric metal–vacuum–metal junctions for applications in energy conversion devices," *Nanotechnology*, vol. 21, no. 14, p. 145204, 2010.

[87] M. N. Gadalla, M. Abdel-Rahman, and A. Shamim, "Design, optimization and fabrication of a 28.3 THz nano-rectenna for infrared detection and rectification," *Scientific reports*, vol. 4, p. 4270, 2014.

[88] H. Mashaal and J. M. Gordon, "Efficiency limits for the rectification of solar radiation," *Journal of Applied Physics*, vol. 113, no. 19, p. 193509, 2013.

[89] E. Briones, J. Alda, and F. J. González, "Conversion efficiency of broad-band rectennas for solar energy harvesting applications," *Optics express*, vol. 21, no. 103, pp. A412-A418, 2013.

[90] M. W. Knight, H. Sobhani, P. Nordlander, and N. J. Halas, "Photodetection with active optical antennas," *Science*, vol. 332, no. 6030, pp. 702-704, 2011.

[91] G. C. Holst, *Common sense approach to thermal imaging*. Washington, DC, USA: SPIE Optical Engineering Press, 2000.

[92] J. S. Tyo, D. L. Goldstein, D. B. Chenault, and J. A. Shaw, "Review of passive imaging polarimetry for remote sensing applications," *Applied optics*, vol. 45, no. 22, pp. 5453-5469, 2006.

[93] M. A. Brun, F. Formanek, A. Yasuda, M. Sekine, N. Ando, and Y. Eishii, "Terahertz imaging applied to cancer diagnosis," *Physics in medicine and biology*, vol. 55, no. 16, p. 4615, 2010.

[94] A. Rogalski, *Infrared Detectors*. Amsterdam: Gordon and Breach Science Publishers, 2000.

[95] A. Rogalski, "History of infrared detectors," *Opto-Electronics Review*, vol. 20, no. 3, pp. 279-308, 2012.

[96] P. Martyniuk, J. Antoszewski, M. Martyniuk, L. Faraone, and A. Rogalski,

"New concepts in infrared photodetector designs," *Applied Physics Reviews*, vol. 1, no. 4, p. 041102, 2014.

[97] X. He, F. Léonard, and J. Kono, "Uncooled carbon nanotube photodetectors," *Advanced Optical Materials*, vol. 3, no. 8, pp. 989-1011, 2015.

[98] M. L. Brongersma, "Plasmonic Photodetectors, Photovoltaics, and Hot-Electron Devices," in *Proceedings of the IEEE*, vol. 104, 2016, pp. 2349-2361.

[99] K. L. Kelly, E. Coronado, L. L. Zhao, and G. C. Schatz, "The optical properties of metal nanoparticles: the influence of size, shape, and dielectric environment," *The journal of physical chemistry B*, vol. 107, no. 3, pp. 668-677, 2003.

[100] W. A. Murray and W. L. Barnes, "Plasmonic materials," *Advanced materials*, vol. 19, no. 22, pp. 3771-3782, 2007.

[101] A. Rogalski, "Infrared detectors: status and trends," *Progress in quantum electronics*, vol. 27, no. 2, pp. 59-210, 2003.